

UNIVERSITÀ DEGLI STUDI
DI MODENA E REGGIO EMILIA

Dottorato di ricerca in Medicina Molecolare e Regenerativa

Ciclo XXXII

Selective ion transport in graphene-based membranes for sensing and biomedical applications

Candidata: Vanesa Quintano

Relatore (Tutor): Prof. Fabio Biscarini

Co-Relatore: Prof. Vincenzo Palermo

Coordinatore del Corso di Dottorato: Prof. Michele De Luca

Università degli Studi di Modena e Reggio
Emilia

PHD PROGRAM IN MOLECULAR AND REGENERATIVE
MEDICINE XXXII CYCLE

*SELECTIVE ION TRANSPORT IN
GRAPHENE-BASED MEMBRANES FOR
SENSING AND BIOMEDICAL
APPLICATIONS*

VANESA QUINTANO

COORDINATOR:

PROF. MICHELE
DE LUCA

SUPERVISOR:

PROF. FABIO
BISCARINI
PROF. VINCENZO
PALERMO

RELATORE: PROF. FABIO BISCARINI
Life Science Department
University of Modena and Reggio Emilia
Via Campi, 103 I-41125 Modena
Italy
Tel: +39 059 205 8587
Fax: +39 059 205 5410
e-mail: fabio.biscarini@unimore.it

CO-RELATORE: PROF. VINCENZO PALERMO
CNR – National Research Council of Italy
Institute for Organic Synthesis and Photoreactivity
Via Gobetti 101, 40129, Bologna
Italy
Tel: +39 051 6399932
e-mail: vincenzo.palermo@isof.cnr.it

*To those who inspired it
and will not read it*

*“NOTHING IN LIFE IS TO BE FEARED, IT IS ONLY TO BE UNDERSTOOD.
NOW IS THE TIME TO UNDERSTAND MORE, SO THAT WE MAY FEAR LESS”*

MARIE SKŁODOWSKA-CURIE

TABLE OF CONTENTS

TABLE OF CONTENTS	11
ABSTRACT.....	15
SINTESI.....	17
1 INTRODUCTION	25
<i>1.1 Ion Transport</i>	<i>27</i>
<i>1.2 Biomimetic Materials.....</i>	<i>30</i>
<i>1.3 Wearable Electronics</i>	<i>31</i>
2 GRAPHENE-BASED MATERIALS.....	35
<i>2.1 Graphene</i>	<i>37</i>
<i>2.2 Graphene Oxide (GO).....</i>	<i>40</i>
<i>2.2.1 GO in Sensors</i>	<i>42</i>
<i>2.3 GO Membranes (GOM).....</i>	<i>43</i>
<i>2.3.1 GOM Applications</i>	<i>46</i>
3 CHARACTERIZATION & FABRICATION METHODS.....	51
<i>3.1 X-Ray Diffraction (XRD).....</i>	<i>53</i>
<i>3.2 HPLC-MS.....</i>	<i>53</i>
<i>3.3 NMR</i>	<i>53</i>
<i>3.4 Scanning Probe Microscopy (SPM).....</i>	<i>53</i>
<i>3.4.1 Atomic Force Microscopy (AFM)</i>	<i>54</i>
<i>3.4.2 Kelvin Probe Force Microscopy (KPFM).....</i>	<i>56</i>
<i>3.5 Electronic Microscopy (SEM/EDX).....</i>	<i>58</i>
<i>3.6 X-ray Photoelectron Spectroscopy (XPS).....</i>	<i>58</i>

<i>3.7 UV-VIS Spectroscopy</i>	60
<i>3.8 Ultrafast UV-VIS Spectroscopy</i>	61
<i>3.9 Computational Calculations (DFT)</i>	62
<i>3.10 Electrochemical Characterization</i>	62
<i>3.11 Fabrication Methods</i>	64
3.11.1 3D Printer.....	64
3.11.2 Spin Coating.....	65
3.11.3 Drop-Casting.....	67
4 GOM: EXPERIMENTAL ACTIVITIES	69
<i>4.1 GO Preparation & Chemical Characterization with XPS</i>	71
<i>4.2 Membrane Preparation</i>	73
<i>4.3 Chemical Analysis of GOM</i>	76
<i>4.4 Set-up for Electrochemical Measurements</i>	77
4.4.1 Set-up Out of Plane.....	84
4.4.2 Set-up in Plane.....	85
<i>4.5 Results and Conclusions</i>	86
4.5.1 Ion Transport, a Brief Introduction.....	87
4.5.2 Out of Plane.....	91
4.5.3 In Plane.....	91
5 PAH: AZOBENZENE	105
<i>5.1 Azomolecules for Supramolecular Functionalization</i>	111
5.1.1 Synthesis Triazole Azobenzene.....	112
5.1.2 Switching Study in Solution.....	117
5.2 AZOMOLECULES FOR COVALENT FUNCTIONALIZATION:	118
5.1.2 Photoswitching Study in Different Environments (AZO1, AZO2).....	118
5.2.2 Covalent Functionalization (XPS-XRD).....	138

6	AZO MEMBRANE	141
6.1	<i>Fabrication of GO-PAH Membrane.....</i>	<i>142</i>
6.2	<i>Switching of GO-PAH Membrane.....</i>	<i>142</i>
7	GOM FOR SENSOR APPLICATIONS.....	147
7.1	<i>Prototypes Biosensors</i>	<i>149</i>
8	CONCLUSIONS	167
	ACRONYMS.....	171
	REFERENCES.....	173
	LIST OF FIGURES	183
	LIST OF TABLES	191
	LIST OF ACTIVITIES DURING PHD.....	193
	ACKNOWLEDGEMENTS	197

ABSTRACT

Biological ion channels intelligently controlling ions across cell membranes serve as a big source of bio-inspiration for the scientists to build bio-inspired smart solid-state nanopores and nanochannels with practical applications. Graphene Oxide (GO) based membranes that differentiate ions are being actively developed to meet the needs in separation, sensing, biomedical, and water treatment technologies. Biomimetic approaches that combine bioinspired functional molecules with solid state supports offer great potential for imitating the functions and principles of biological ion channels.

GO is an atomic-thick sheet of carbon atoms with oxygen (content $\approx 30\%$ in weight). The presence of different functional groups, such as epoxides, alcohols, and carboxylic acids, allows to obtain stable dispersion in all of the most common solvents and water, in particular (stability > 2 years). The high processability of GO in water allows to use it as building block to realise 2D/3D structures with tuned order. The simplest structure is the lamellar membrane where all the GO sheets are stacked with a distance lower than 2 nm. Moreover, the distance can be easily tuned with humidity. These membranes have shown potential in a variety of applications, including water desalination and purification, gas and ion separation, biosensors, proton conductors, lithium-based batteries and super-capacitors.

The combination of 2D materials with small organic molecules (PAH) allows to create new composite materials that merge together the 2-dimensional structure of graphene-based materials with the tunable (photo) chemical properties of dyes.

This thesis is the first step to develop GO-PAH composites. For this reason,

the two materials are separately investigated and after mixed.

Regarding PAH, we study the behaviour of a well-known class of photoswitching molecules (azobenzenes) from cis to trans isomer using light stimuli as an ideal probe to study conformational freedom in different constrained environments and, furthermore, confined in lamellar GO membranes.

Regarding the GO membranes, a comprehensive understanding of all the mechanisms involved in the ion selectivity has not been developed. This work aims to clarify some aspects and as well as the design and fabrication of biomimetic and free-standing Graphene Oxide (GO) based membranes covered with polymer that can be integrated into a biosensing 3D printed device.

GO functionalization with PAH allows to tune the capabilities for selective recognition and transport of the composite membranes. The resulting GO-based membranes show remarkable ion selectivity toward the specific ion of interest, for the transport across the membranes as in the biological ion channels. By combining the selective graphene based membranes with commercial electrodes (Metrohm DropSens) we develop a wearable and selective biosensor for K^+/Na^+ in sweat that can be used to monitor disease such as hypokalemia or cystic fibrosis in children.

SINTESI

Le proprietà di selettività ionica e direzionalità dei canali ionici biologici sono studiate da decenni e continuano a essere fonti di ispirazione per la realizzazione di materiali e strutture per applicazioni nella sensoristica e nel campo biomedicale. Nell'ultimo decennio, grande attenzione è stata rivolta allo studio delle membrane a base grafene ossido (GO) che permettono di realizzare materiali e sistemi che mimano alcune proprietà dei canali ionici per applicazioni tecnologiche. In genere, l'integrazione di materiali che mimano alcuni processi biologici con sistemi a stato solido offre un enorme interesse per riprodurre le funzioni e i principi dei canali ionici biologici.

Il GO è un materiale bidimensionale composto da un singolo foglio monoatomico di grafene fortemente ossidato (concentrazione di ossigeno $\approx 30\%$ in peso). La presenza di numerosi gruppi funzionali, quali idrossili, ossidrili, carbossili, permette di ottenere sospensioni stabili di GO in tutti i comuni solventi. In particolare, il GO forma sospensioni acquose stabili per un paio di anni. Tale caratteristica permette una elevata processabilità del GO che può essere riassembleto formando strutture 2D/3D in maniera controllata. La struttura assemblata più semplice è la membrana lamellare, dove tutti i singoli fogli sono paralleli con una distanza inferiore a 2 nanometri e che può essere finemente controllata in funzione dell'umidità residua dell'aria. Tali membrane mostrano un potenziale applicativo in numerosi settori quali: la desalinizzazione e purificazione dell'acqua, la separazione di ioni e gas, biosensoristica, conduttori protonici, sistemi per batterie e super-capacitori.

La combinazione di tali membrane con piccole molecole organiche (PAH) permette di creare una nuova classe di materiali lamellari con proprietà fotochimiche controllabili. L'obiettivo di questa tesi di dottorato è la

realizzazione di sistemi compositi lamellari GO-PAH.

Questa tesi rappresenta il primo passo per lo sviluppo di tali compositi. Per questo motivo i materiali vengono studiati separatamente per poi essere miscelati.

I PAH utilizzati appartengono a una nota classe di molecole fotocromiche quali le azobenzeni, la cui isomerizzazione cis- e trans- può essere pilotata tramite stimoli luminosi e il loro comportamento in diversi ambienti (liquido, superficie, incapsulato in matrici polimeriche), nonché confinati in membrane lamellari di GO.

Per quanto riguarda le membrane lamellari di GO, un quadro complessivo dei meccanismi responsabili della selettività ionica non è ancora stato sviluppato, perciò il lavoro di questa tesi si prefigge di chiarire alcuni meccanismi, nonché di realizzare dispositivi sensoristici. Per questo motivo sono state progettate e fabbricate membrane autoportanti di GO incapsulate in matrici polimeriche per lo studio del trasporto ionico e successivamente integrate in dispositivi stampati per biosensori.

La funzionalizzazione con PAH permette di modificare e controllare la capacità di riconoscimento e trasporto selettivi del sistema composito. Le membrane a base di GO così ottenute mostrano una notevole selettività ionica analoga a quella dei canali di ioni biologici. La combinazione delle membrane a base GO con elettrodi commerciali (ChemSens) hanno permesso lo sviluppo di un biosensore indossabile che misuri la concentrazione di K^+/Na^+ nel sudore e che può essere utilizzato per monitorare malattie quali la ipopotassiemia e la fibrosi cistica nei bambini.

Keywords

Graphene

Biosensor

Ion-transport

Self-assembling

Photoswitching

All the activities have been performed in collaboration with European partners involved within the EU Marie Skłodowska-Curie project “ISwitch” (G.A. 642196) and GrapheneCore2 (G.A. 785219) – Graphene Flagship.

1 INTRODUCTION

Current chapter introduces the field of ion transport starting from the state-of-the-art and how it is used for the fabrication of wearable devices for biomedical applications.

1.1 Ion Transport

Biological ion channels intelligently controlling ions across cell membranes (Figure 1) serve as a big source of inspiration for the scientists to build smart solid-state nanopores and nanochannels with practical applications. With the advance of chemistry, materials science, and nanotechnology, significant progress has been achieved in the design and application of synthetic nanofluidic devices and materials, mimicking the gating, rectifying, and adaptive functions of these biological ion channels. Fundamental physics and chemistry behind these novel **transport phenomena** on the nanoscale have been explored. However, toward real-world applications, one major challenge is to extrapolate these devices into macroscopic materials. Recently, inspired by nature, the material design and large-scale integration of artificial nanofluidic devices have stepped into a completely new stage, termed 2D nanofluidics. Unique advantages of the 2D layered materials have been found, such as facile and scalable fabrication, high flux, efficient chemical modification, tunable channel size, etc. These features enable wide applications in, for example, **biomimetic ion transport manipulation**, molecular sieving, water treatment, and nanofluidic energy conversion and storage. This work study the field of “2D nanofluidics”, with emphasis on the thought of bio-inspiration (Figure 2).¹

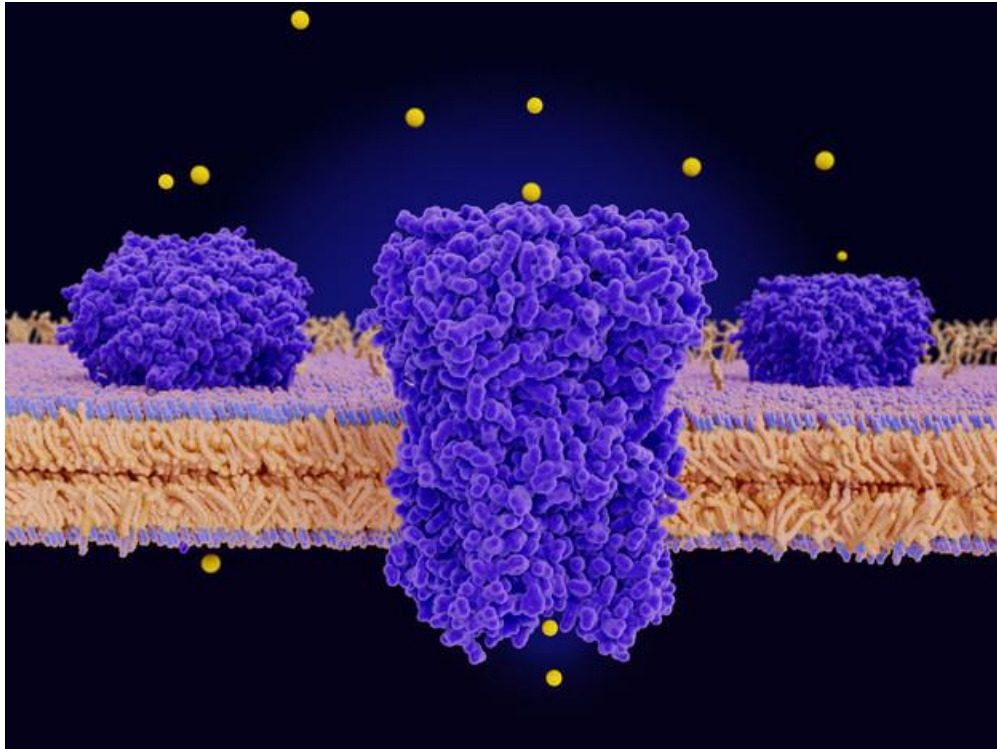


Figure 1. Chloride channels conducting chloride anions across a cell membrane.

The research field of nanofluidics studies the mass and charge transport within a characteristic length scale down to 1–100 nm in at least one dimension.^{2,3} Different from that in the bulk phase, nanofluidic transport is largely governed by the surface properties of channel walls that lead to various unique transport phenomena. For example, in charged nanochannels, the ionic conductivity is governed by the surface charge, particularly in low concentration electrolyte solutions.⁴ In sufficiently narrow nanochannels, the transporting molecules can be sieved by size exclusion or molecular recognition effects.⁵ Therefore, tremendous attention has been paid in engineering the geometry and surface chemistry of nanofluidic channels to manipulate the molecular transport behaviors.⁶

In the past decade, two asymmetric ion transport phenomena have been identified in synthetic nanofluidic structures, the rectified ionic current and the net diffusion current.³ The rectified ionic current is observed as a diode-like

current-voltage response when switching the voltage bias and indicates a preferential transport direction in the nanofluidic channel.⁷ The net diffusion current is generated from the asymmetric ion diffusion through charged nanochannels, a direct product of charge selectivity.

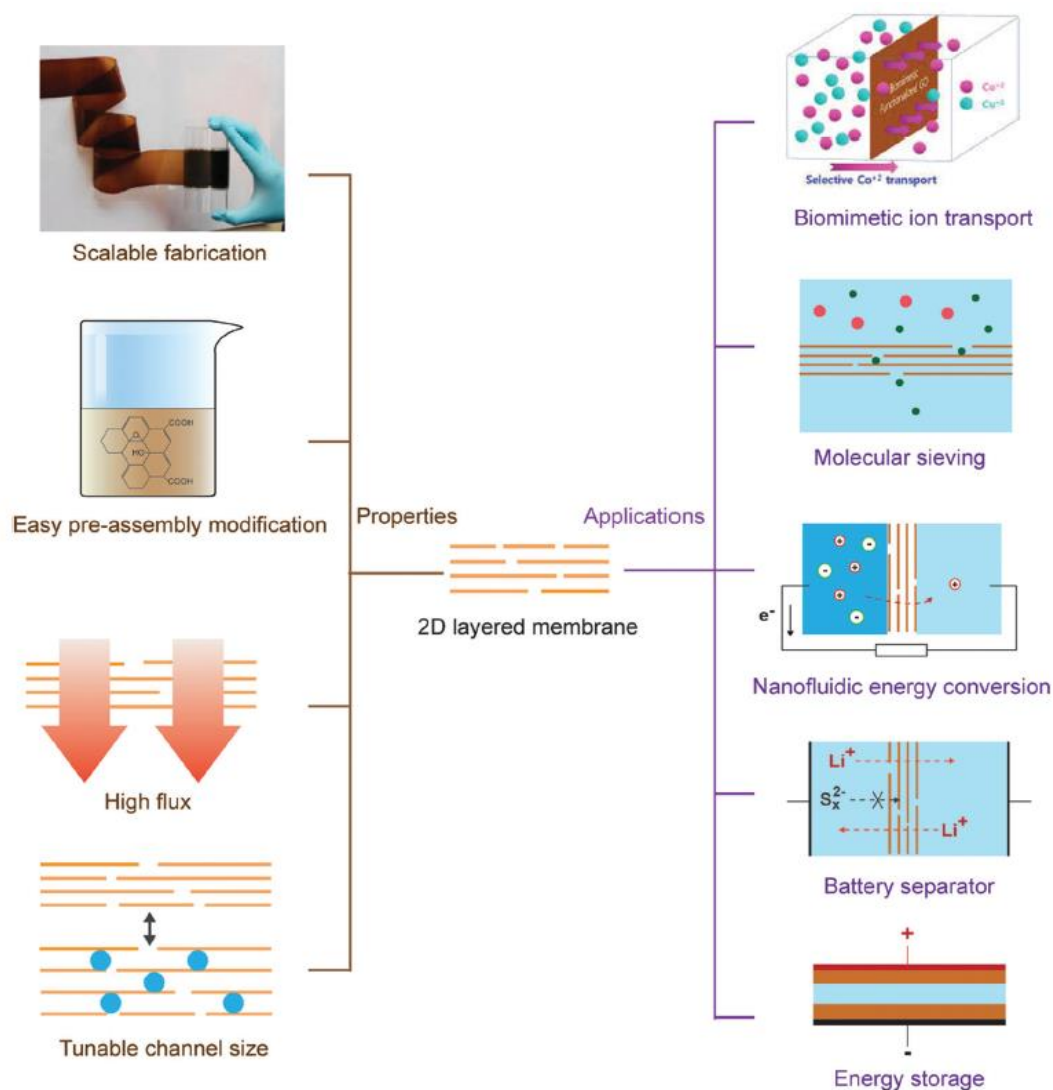


Figure 2. Fundamental properties and applications of 2D layered materials. The exfoliation–reconstruction strategy enables highly scalable fabrication and highly efficient chemical modification of the 2D nanofluidic systems with ultra-high ion or water flux and tunable channel size. Meanwhile, wide applications are found in, for example, biomimetic ion transport manipulation, molecular sieving, nanofluidic energy conversion, battery separators, and energy storage.¹

1.2 Biomimetic Materials

Biomimetic materials are designed to replicate one or more attributes of a material produced by a living organism.⁸ Honeycomb structure of the beehive, the fibre structure of wood, spider silks, nacre, bone, hedgehog quills are a short list of examples of natural systems which have inspired materials commonly used in the everyday life.

Bioinspired materials at nanoscale and microscale have been well studied for the purposes of building smart materials for various applications in biosensors, micro/nanofluidic devices, and clinical medicine settings.^{9,10,11}

Scientists and engineers are interested in the design and fabrication of synthetic nanofluidic architectures that mimic the gating functions of biological ion channels and lipidic membranes: such as the asymmetric structure, the precise ion selectivity, the stimuli-responsive gating behaviours, etc.⁶

The use of supramolecular chemistry is one of the main approaches to reproduce functions of biological systems at nanoscale. In general, the tuning of weaker reversible non-covalent interactions between molecules, (e.g. hydrogen bonding, metal coordination, hydrophobic forces, van der Waals forces, π - π^* interactions, electrostatic effects, etc.) has been successfully used to design and to fabricate a class of biomimetic systems for synthetic photosynthesis,¹² molecular motors,¹³ and switches.¹⁴

The increasing interest in scientific and technological application of such systems has been recognized with a Nobel Prize in Chemistry in 2016 to Stoddart¹⁵, Sauvage¹³ and Feringa.¹⁶ It is noteworthy to underline also the contribution of prof. Balzani¹⁷ at the Bologna University.

1.3 Wearable Electronics

Driven by the increasing demand for continuous health monitoring, fitness tracking, and virtual reality, there has been a fast-growing market for wearable devices. The total value of wearable devices was estimated to be around \$22 billion in 2016 and the worldwide revenue is expected to reach \$97.8 billion by 2023, growing at a compound annual growth rate of around 24% from 2017 to 2023.¹⁸

Wearable devices are becoming widespread in a wide range of applications, from healthcare to biomedical monitoring systems, which enable continuous measurement of critical biomarkers for medical diagnostics, physiological health monitoring and evaluation. Since the global elderly population growing, various chronic and acute diseases become increasingly important, and the medical industry is changing dramatically due to the need for point-of-care (POC) diagnosis and real-time monitoring of long-term health conditions. Wearable devices have evolved gradually in the form of accessories, integrated clothing, body attachments and body inserts. Over the past few decades, the tremendous development of electronics, biocompatible materials and nanomaterials has resulted in the development of implantable devices that enable the diagnosis and prognosis through small sensors and biomedical devices, and greatly improve the quality and efficacy of medical services.

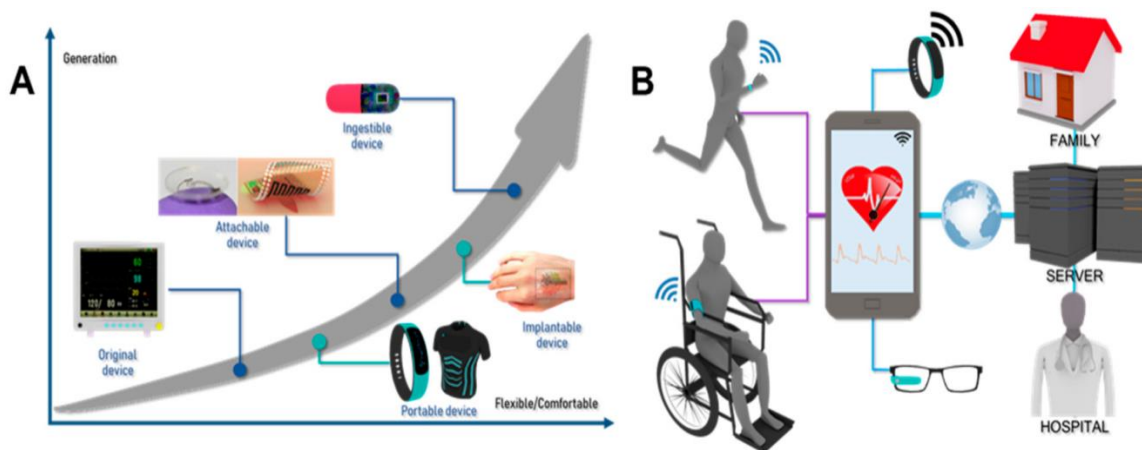


Figure 3. Industrial wearable technologies. (A) Evolution of wearable medical devices (B) Application of wearable devices in the healthcare and biomedical monitoring systems.¹⁹

Moreover, by incorporating engineering technology into skin adhesives, traditional medical skin adhesive patches can be transformed into advanced biomedical devices with integrated functionalities. Currently, with recent advances in nanofabrication, nanomaterials and flexible electronics, the skin patch has evolved into a smart multifunctional device by incorporating core functions of bulk medical instruments within a thin flexible patch (Figure 4).

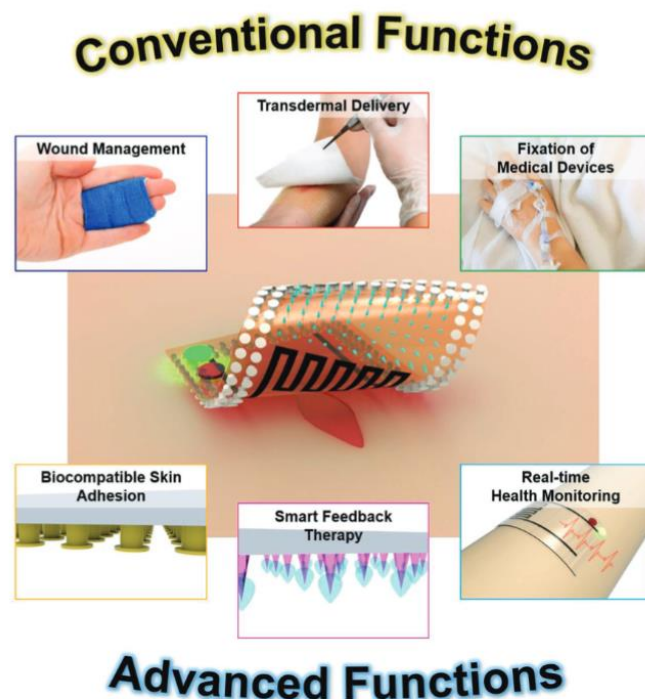


Figure 4. Conceptual illustration of the medical skin adhesive patch with various fundamental and advanced functions.²⁰

Real-time health monitoring systems that can precisely measure vital signs of the human body with high patient compliance are of great importance for advanced health care, specially for prevention and customisation.

To address this demand, skin patches with on-board monitoring and sensing functions of human vital signals have been extensively developed thanks to advances in nanomaterials and flexible electronics. These systems are typically in the form of thin flexible patches in which conducting or semiconducting nanomembranes or nanomaterials (carbon nanotubes (CNTs), nanowires, and graphene) are integrated with soft polymeric membranes (PDMS).^{21, 22, 23}

Consequently, the overall system has low effective elastic modulus, which enables intimate coupling to the skin, and therefore significantly enhances sensing quality and stability. Also, the integrated systems in the form of a single attachable patch can greatly favor patient compliance, facilitating real-time, long-term monitoring even during daily activities.²⁰

Several activities in this field have been performed at the University UniMoRe. For the sake of simplicity a couple of examples are here reported.

Recently, prof. Biscarini at the University UniMoRe demonstrated the feasibility of comfortable and transparent transistor devices fabricated on a fully resorbable bioscaffold. The device fabrication relies on a simple process which allows patterning of active areas of the conductive polymer PEDOT:PSS contacted by gold electrodes on the bioscaffold. The resulting structure combines biocompatibility and biodegradability with excellent electronic properties for fast and sensible potentiometric sensing in aqueous conditions. The fast ion-to-electron exchange which is crucial for bioelectric interfaces results from the intrinsic materials properties of the PEDOT:PSS layer. By optimizing the layer thickness and the channel geometry we achieve the sensing of signals down to a few tens of micro-volts at timescales of a few milliseconds. As a medically relevant bioelectric recording device, we applied the transistor in

electrocardiography and show a signal-to-noise ratio that is comparable to the one of standard Faradaic electrodes.²⁴

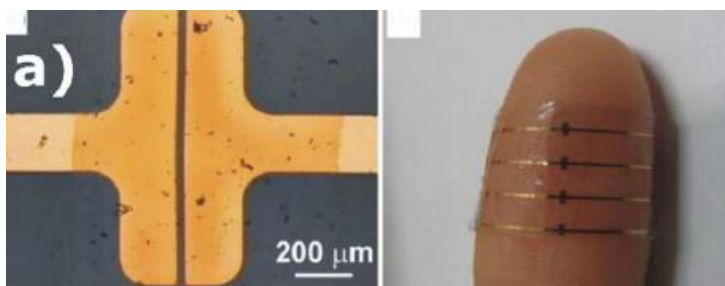


Figure 5. PEDOT:PSS polymer based device showing properties such as flexibility and transparency and used for Electrocardiogram (ECG) recording when attached to human skin.²⁴

Moreover, the group of prof. Zanardi fabricated a flexible electrode system entirely constituted by single-walled carbon nanotubes (SWCNTs). It has been proposed as the sensor platform for β -nicotinamide adenine dinucleotide (NADH) detection.

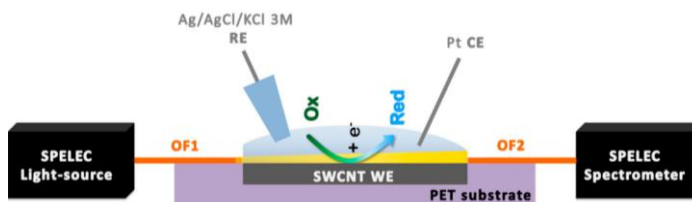


Figure 6. Schematic view of the UV/Vis absorption spectroelectrochemical set-up in parallel configuration.²⁵

The performance of the device, in terms of potential at which the electrochemical process takes place, significantly improves by electrochemical functionalization of the carbon-based material with a molecule possessing an o-hydroquinone residue, namely caffeic acid.²⁵

2 GRAPHENE-BASED MATERIALS

The purpose of this chapter is to give an overview of graphene-based materials, in particular Graphene Oxide (GO), its use to fabricate membranes and possible applications for biosensing.

INTRODUCTION II

2.1 Graphene

Graphene is one of the carbon allotrope²⁶ given by sp^2 -hybridized carbon atoms arranged into a two-dimensional hexagonal lattice in which each atom is bond to three adjacent atoms, forming angles of 120° within the plane, with interatomic distances of 1.42 \AA and center to center distances of 2.46 \AA .²⁷ The C-C bonds are covalent (σ and delocalized π orbitals), leading to a particularly strong and rigid structure.

First studies on graphene were attributed to Andre K. Geim and Konstantin S. Novoselov at the University of Manchester, UK. They used a simple, but effective, mechanical exfoliation of graphite by scotch tape to transfer single graphene sheet on silicon.^{28,27} The deposited graphene possesses size of several microns and irregular shape. For their studies, they were awarded with Nobel Prize in Physics in 2010.

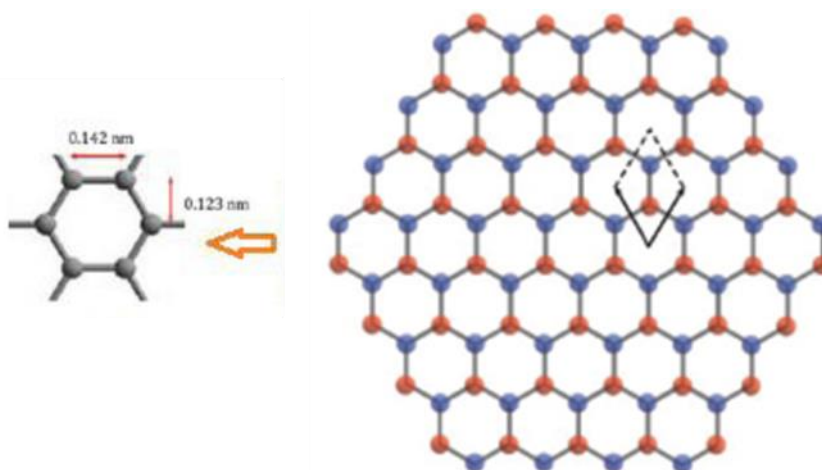


Figure 7. Unit cell of graphene evidencing the two sub-lattice structures (red and blue).²⁷

Graphene also constitutes the basic structural element of other allotropes, including graphite, fullerenes, and carbon nanotubes (Figure 8). In particular, graphite consists of multiple layers of particularly wide graphene units

interacting with each other through weak Van der Waals forces. Fullerenes are rolled graphene sheets possessing linked hexagonal, pentagonal and, sometimes, heptagonal rings. Fullerenes possessing a cylindrical shape are also called carbon nanotubes; in this case they exclusively contain hexagonal carbon rings.

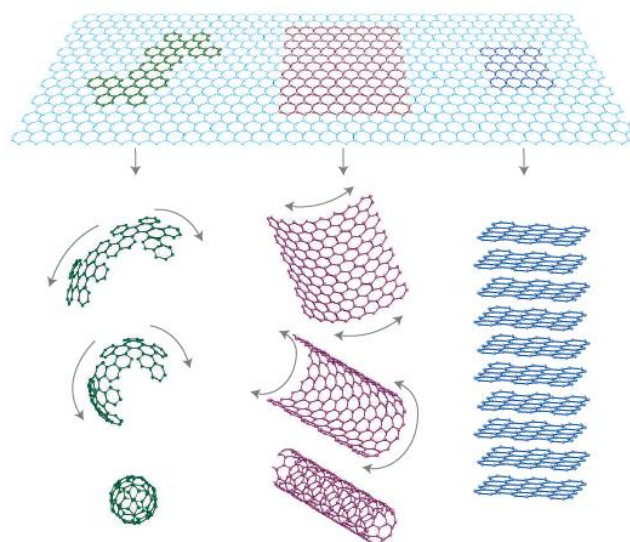


Figure 8. Scheme showing that graphene is a 2D building material for carbon materials of all other dimensionalities: it can be wrapped up into 0D fullerenes, rolled into 1D nanotubes or stacked into 3D graphite.²⁸

Together with the planar structure, the sp^2 hybridization provides high mechanical stability of all these materials.

Graphene-based allotropes can be classified depending on their spatial arrangement (Figure 9). In particular, fullerene can be considered as zero-dimensional (0D), carbon nanotubes as one-dimensional (1D), graphene as two-dimensional (2D) and graphite as three-dimensional (3D) structures.

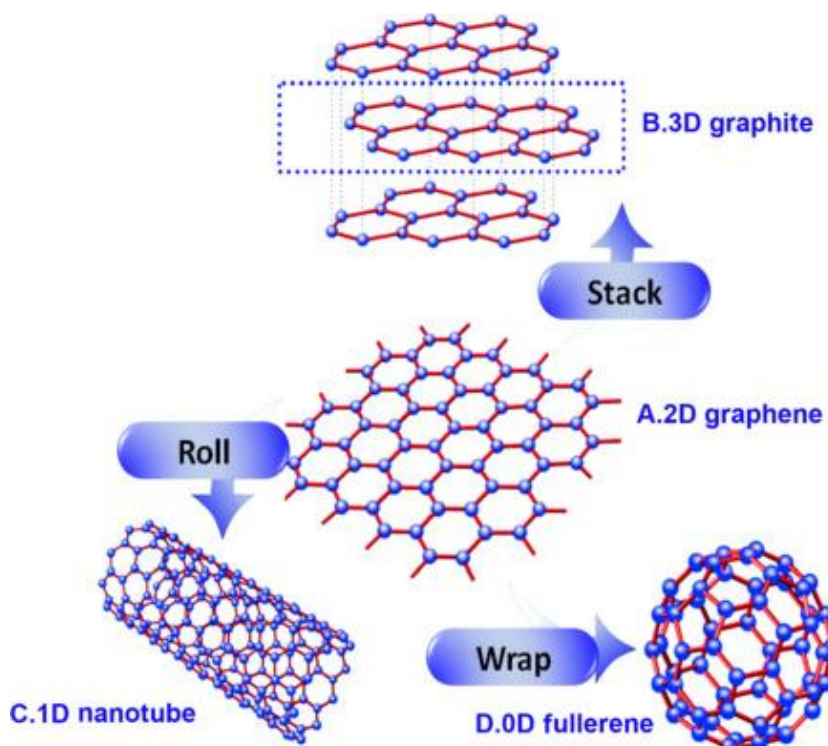


Figure 9. Graphene (A) is a two-dimensional material for constructing other nanoscale carbons such as (B) 3D graphite, (C) 1D carbon nanotubes, and (D) 0D fullerene C_{60} .²⁹

Graphene is the most exciting and extensively explored carbon allotrope in the fields of basic sciences, technology, and engineering due to its distinctive characteristics such as a large specific surface area, good conducting properties, high intrinsic mobility, thermal conductance, and an optical transmittance.³⁰ Since the high optical transparency and high electrical conducting properties, thin films of graphene nanosheets are promising materials for several (opto)electronic applications, such as i) transparent conducting sensors for liquid crystal displays, ii) touchscreens of mobile devices, iii) organic photovoltaic cells, and iv) organic light-emitting diodes. Moreover, the huge electroactive surface area (up to ca 2,000 m^2/g for a single sheet) makes graphene an outstanding electrode material for the design of numerous electrochemical sensors and biosensors.³¹

Despite the high quality of the produced graphene single sheets with very low density of defects, the scotch-tape approach developed at the Manchester University cannot be upscaled. For this reason many synthetic procedures have

been developed during this last decade. They can be generically distinguished in top-down and bottom-up approaches. A schematic representation is reported in Figure 10.

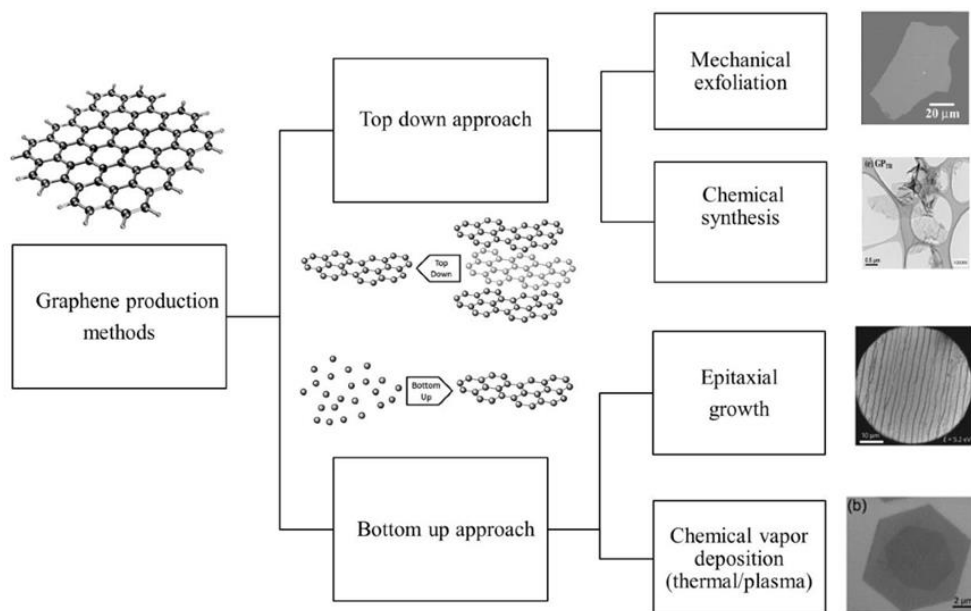


Figure 10. A flow chart on graphene production methods with some exemplificative examples of the procedures mostly used: mechanical exfoliation, epitaxial growth, CVD, thermally reduced graphene.

2.2 Graphene Oxide (GO)

Although the unique electronic and mechanical properties of graphene suggest numerous intriguing applications, the requisite large-scale direct synthesis and solution-based handling have proven difficult.³² Graphene Oxide (GO) is one of the most common graphene-based material providing a solution-friendly route to facile, high-throughput graphene manipulation.

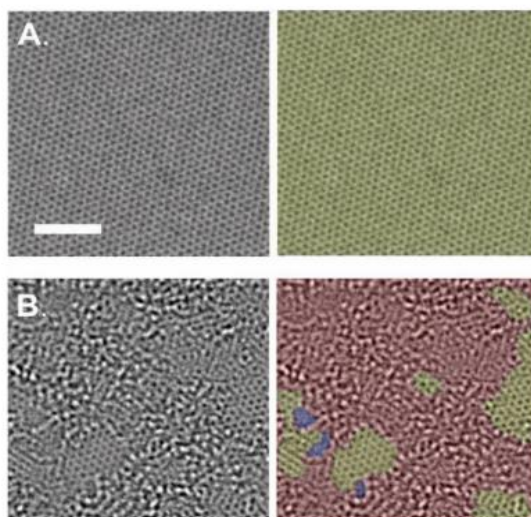


Figure 11. Aberration corrected TEM images of the following materials. Scale bar, denoting 2 nanometers, is valid for all images. (A) Single suspended sheet of graphene. On the right, graphitic area indicated in yellow. (B) Single suspended sheet of GO. On the right, holes are indicated in blue, graphitic areas in yellow, and high contrast, disordered regions, indicating oxygen functionalities, in red.³²

GO is a single sheet with a complex structure given by a patchwork of aromatic clusters surrounded by oxidized regions and various oxygen functional groups (-CO-, -OH-, -COOH), typically the C:O ratio ranges between 2 and 3. The presence of oxidized groups is due to the process of graphite exfoliation, generally occurring by addition of strong oxidizing agents, and makes the material highly hydrophilic, i.e. well soluble in water; on the other hand, they reduce the conductivity of the material: Exactly one layer of a polycyclic hydrocarbon network, with all carbon atoms hexagonally arranged in a planar condensed ring system.

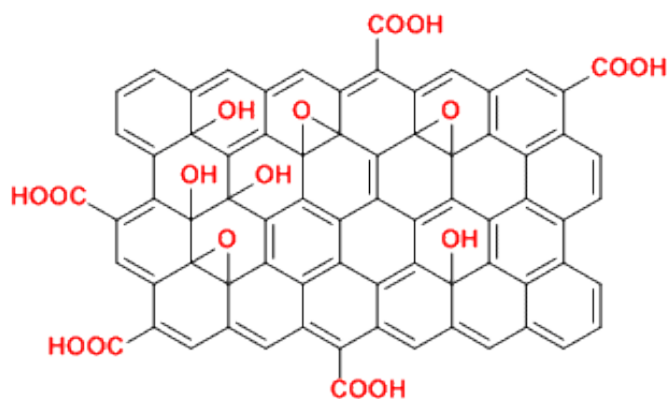


Figure 12. Representative structure of GO.

Moreover, the presence of functional moieties on GO edges and basal planes allows easy functionalization in both water and organic solvents.^{33, 34}

The functional groups give the possibility to add binding sites for further bio-functionalization with biological molecules, and change the properties of the surface.

One issue to take into account is the disintegration of GO in water. The GO sheets become negatively charged on hydration and the membrane should disintegrate owing to electrostatic repulsion. To prevent it, GO should be covered with a layer of polymer.

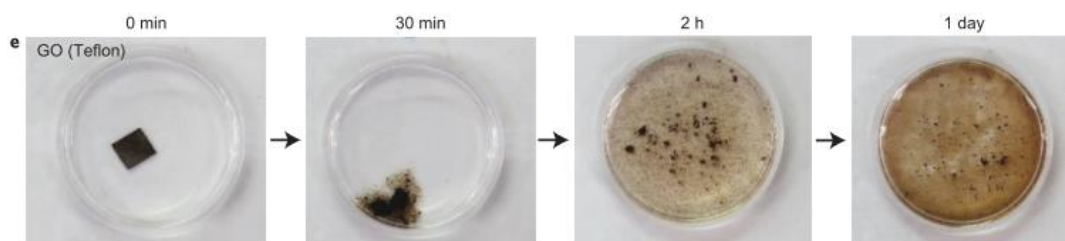


Figure 13. GO membranes obtained from Teflon filters.³⁵

2.2.1 GO in Sensors

GO is widely used for biomedical applications, as active material (such RGO electrodes) and acting as a filter in membranes. The large specific area of graphene promotes the loading of biomolecules in high concentrations on the sensing base to generate good detection sensitivity.³⁶

The following chapter gives an insight into the current state of the art of applying

graphene materials in chemical sensors and biosensors. A large amount of published work (over 230 references) on this topic is discussed to reveal the individual benefits (and flaws) of the members of the graphene-family.

Nanocomposite sensors: Electro-chemical sensors

Assemblies of different materials that form an entity in the nanometer range are often referred to as nanocomposites. They are characterized by a very high surface to volume ratio which explains their superior properties relative to bulk composites. The combination of two or more materials also enables the tailoring of properties such as sensitivity and selectivity.

2.3 GO Membranes (GOM)

A membrane is considered as a barrier with an ability to allow the passage of certain species while blocks other depending on characteristics of the membrane and species to be filtered.³⁷

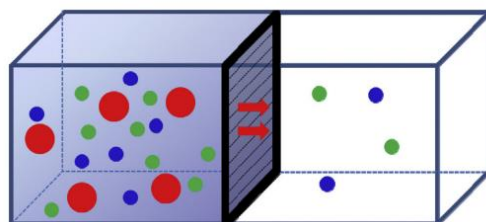


Figure 14. Schematic representing a membrane system.³⁷

Graphene Oxide Membranes (GOM) have been considered to be robust and continue to attract research interest due to their great potential in scientific and practical industrial domains such as water treatment,^{38,33,39,40} desalination,⁴¹ and ion separation.^{42,43}

Thus, GO has emerged as excellent membrane material. In the year 2012 Nair et al., demonstrated that GO membrane allows un-impeded permeation of water

whereas it blocks everything else in the vapor form.⁴⁴ GO is continuously demonstrating its excellent membrane characteristics and offer huge potential for real applications.

It is widely studied the transport of ions out of plane, while 2D materials offer much more straightforward ways to tune porosity by simple stacking the sheets. In Nanoporous graphene membrane the transport depends on the size exclusion and electrostatic interactions. Differently, in stacked GOM, the transport will depend also on the ion adsorption, meaning electrostatic binding, Π -cation interactions and metal coordination (figure 15).

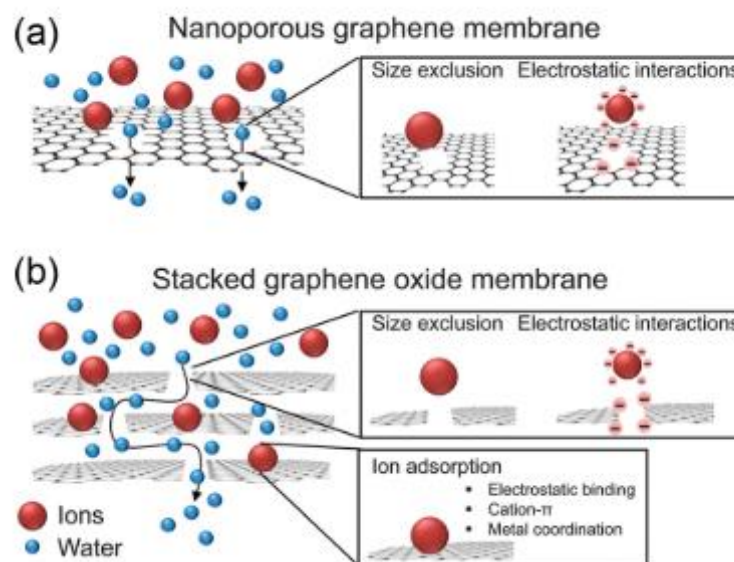


Figure 15. Schematic diagram of the two types of graphene-based membranes. (a) Nanoporous graphene membrane consists of a single layer of graphene with nanopores of defined sizes. Selectivity is achieved by size exclusion or electrostatic repulsion between charged species and the pores. (b) GOM composed of stacked GO sheets. In a GOM, the transport passages are the interlayer spaces between the sheets.⁴⁵

The rejection efficiency of GOM can be controlled by interlayer spacing, which can be readily linked in terms of chemical interactions between functional groups and cations. The effective interlayer space depends on the oxidation (figure 16) rate and the rate of humidity.

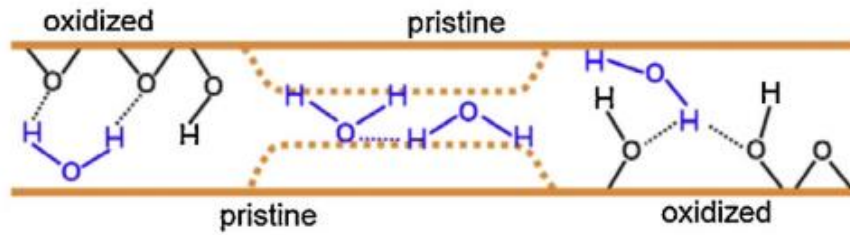


Figure 16. Schematic model of the nanocapillaries in GO films. Monolayer water can move through the capillaries when they are wide opened, however with low humidity the capillaries becomes narrower (shown by dashed line) and as a result there is no sufficient space between the capillaries to accommodate the water molecule. Figure reproduced with permission from.⁴⁴

In conventional 1D nanofluidic systems, the inlet and outlet of the ionic flow are all present along the channel axis, allowing only the horizontal transport mode. While in 2D layered materials enable two independent ways for ion transport, either horizontally or vertically (figure 17), meaning in plane or out of plane.

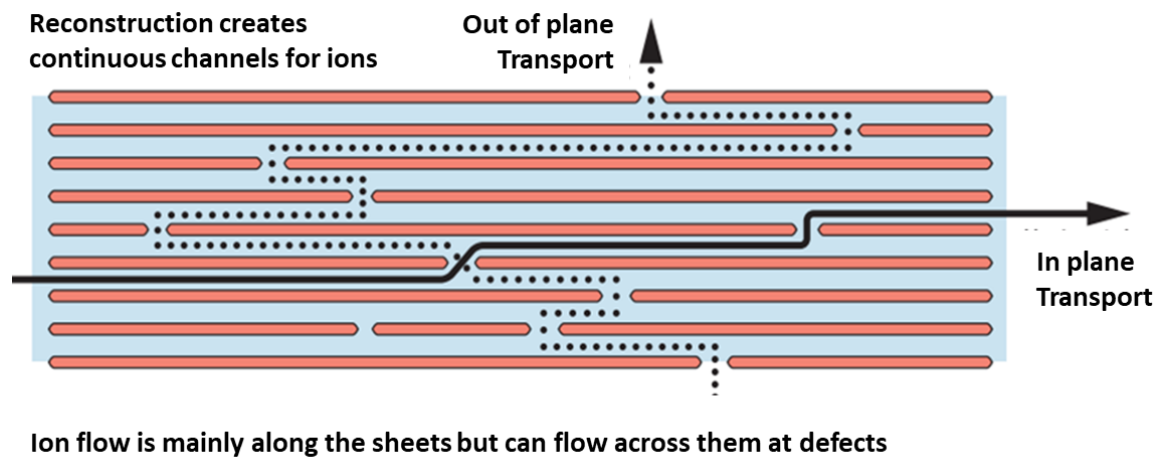


Figure 17. Lamellar film with massive arrays of 2D nanofluidic channels can be made by the exfoliation-reconstruction approach, as illustrated with models of GO sheets terminated with negatively charged carboxyl groups.⁴⁶

For either direction, the ion transport behaviours are governed by the surface properties of the reassembled 2D nanosheets. For example, in GOM, the interlayer distance can be as narrow as 1 nm-wide, and the lamellar fluidic channels are fully covered with an electrical double layer (EDL) associated with the surface charge, leading to unipolar ion transport. In this case, the co-ions are perfectly expelled from the 2D nanochannels, and the counter-ions become the only charge carriers.

Another parameter to take into account is the swelling, when the water penetrates into the nanochannels of the GOM, the interspacing increases, and it is possible to observe this effect by XRD measurements (Figure 18).

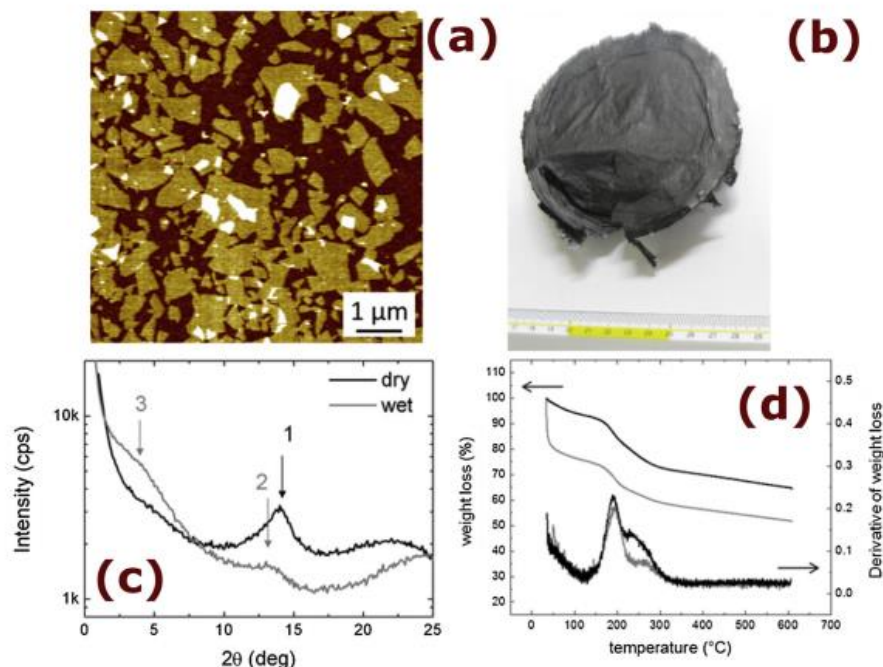


Figure 18. (a) AFM image of the as-prepared GOM, Z-range $\frac{1}{4}$ 3 nm; (b) As-prepared GOM before hydration; (c) XRD surveys and (d) TGA analysis of the dry (black) and hydrated (grey) membranes.⁴⁷

Moreover, it is possible to perform an efficient chemical modification in GOM: Besides inorganic materials,⁴⁸ organic molecules are also highly suitable for chemical modification of nanofluidic devices.^{49,50,51} They offer profuse functional groups on the surface of the channels; therefore, electrostatic interaction, steric hindrance, and hydrophobic interaction can be introduced into the nanofluidic system.³ The strategy for this purpose will be discussed in chapter 5.

2.3.1 GOM Applications

GOMs have been considered to be robust and continue to attract research interest due to their great potential in scientific and practical industrial domains such as water treatment,^{38, 33,39,40} desalination,⁴¹ and ion separation.^{42,43}

The flexibility of GO paper made it feasible to create a flexible nanofluidics device.

As reported by Raidongia Group,⁵² nanofluidic ion transport through GO paper has been already demonstrated. By assembling GO sheets into a multilayer, paper-like structure, numerous nanofluidic channels were formed with height of ~ 1 nm. Characteristic surface charge-governed ion transport was observed for salt concentration up to ~ 50 mM. The ease of fabricating unprecedentedly massive arrays of nanochannels led to ionic currents in the microampere range with centimeter-long devices. The work here demonstrates the feasibility of creating large-scale, flexible nanofluidic devices through reconstructed layer materials. It should be possible to make GO electrically conductive through partially reduction to create gated nanofluidic devices.

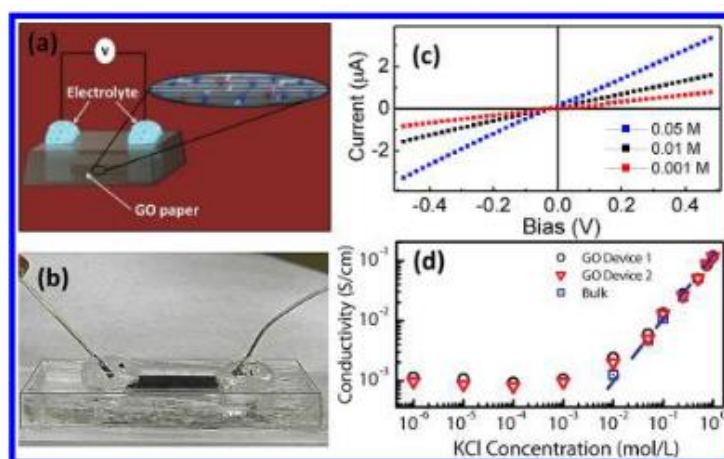


Figure 19. (a) Schematic illustration and (b) photograph showing GO paper-based nanofluidics device. (c) Representative I–V curves recorded at different KCl concentrations. (d) Ionic conductivity as a function of salt concentration measured through GO nanochannels. Results of two devices are presented here, showing good consistency.⁵²

GO membranes show exceptional molecular permeation properties, with promise for many applications. However, their use in ion sieving is limited by a permeation cutoff of ~ 9 Å, which is larger than the diameters of hydrated ions of common salts. The cutoff is determined by the interlayer spacing (d) of ~ 13.5 Å, typical for GO laminates that swell in water. Achieving smaller d for the

laminates immersed in water has proved to be a challenge. Nair's group⁵³ describe how to control d by physical confinement and achieve accurate and tunable ion sieving. Membranes with d from ~ 9.8 Å to 6.4 Å are demonstrated, providing a sieve size smaller than the diameters of hydrated ions. In this regime, ion permeation is found to be thermally activated with energy barriers of ~ 10 – 100 kJmol^{-1} depending on d . Importantly, permeation rates decrease exponentially with decreasing sieve size but water transport is weakly affected (by a factor of <2). The latter is attributed to a low barrier for the entry of water molecules and large slip lengths inside graphene capillaries. They show ion permeation rates through tunable interspace channels applying an external force such as pressure.

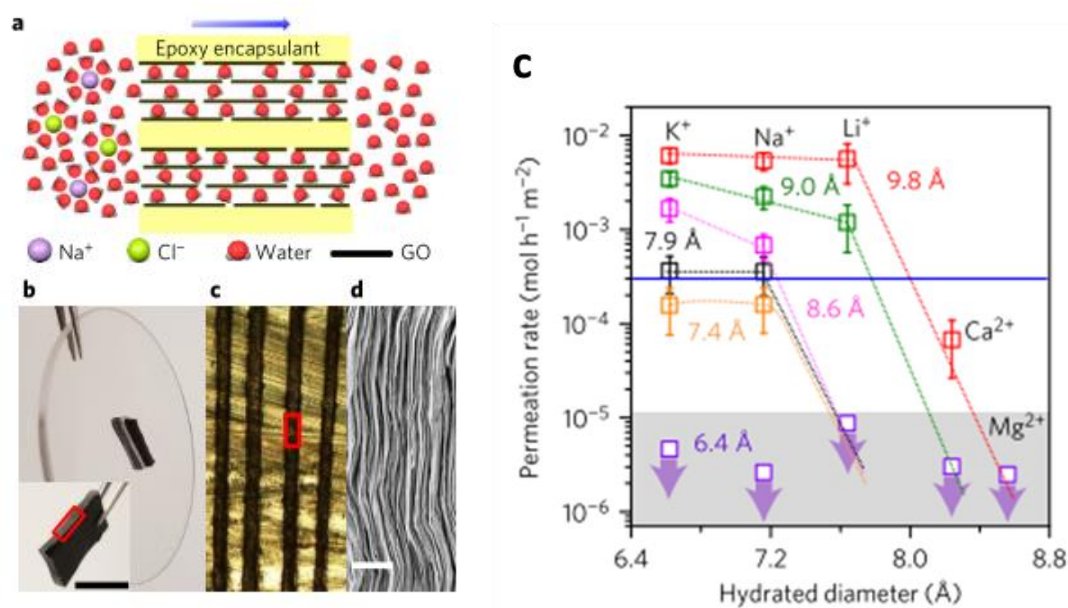


Figure 20. Physically confined GO membranes with tunable interlayer spacing. *a*, Schematic illustrating the direction of ion/water permeation along graphene planes. *b*, Photograph of a PCGO membrane glued into a rectangular slot within a plastic disk of 5 cm in diameter. Inset: photo of the PCGO stack before it was placed inside the slot. Scale bar, 5 mm. *c*, Permeation rates through PCGO membranes with different interlayer distances (colour coded). The salts used were KCl, NaCl, LiCl, CaCl₂ and MgCl₂. Dashed lines are guides to the eye indicating a rapid cutoff in salt permeation, which is dependent on the interlayer spacing.⁵³

Membranes that differentiate ions are being actively developed for biomedical sensing. Biomimetic approaches that combine bioinspired functional molecules with solid-state supports offer great potential for imitating the functions and

principles of biological ion channels. In a recent work was reported the design and fabrication of biomimetic GO based membranes functionalized with a peptide motif that has the capabilities for selective recognition and transport. The peptide, which has ion binding affinity to Co^{2+} ions, was adopted to enable the ion selective filtration capability and was then anchored on a GO surface. The resulting GO-based membranes show remarkable ion selectivity toward the specific ion of interest, for the transport across the membranes as in the biological ion channels. Ion recognition capability of this peptide motif successfully translates into ion specificity for selective transport.⁵⁴

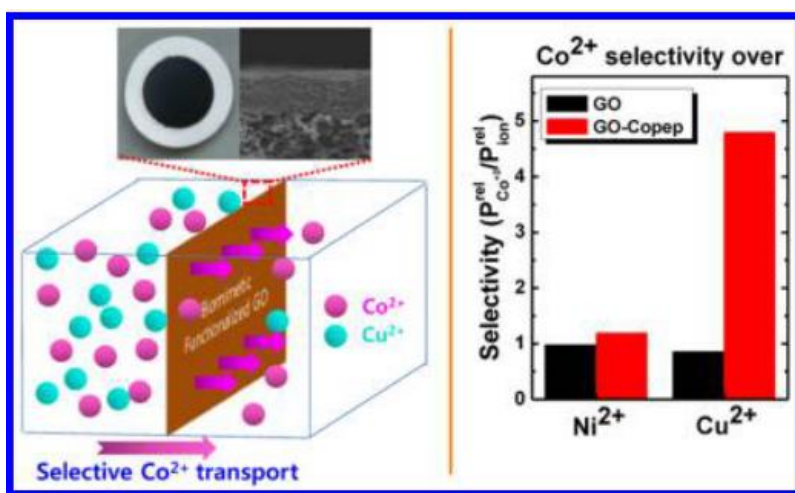


Figure 21. Left: Schem and picture of the biomimetic functionalized GO membrane. Right: Permeation test of Co^{2+} , Ni^{2+} , and Cu^{2+} ions through GO- based membranes.

Challenge & Aim:

In general, synthetic chemistry is performed in solution where molecules can interact with ions while freely floating in a 3D environment. Though, a working solid-state device is a (quasi) 2D system with lateral dimension up to the macroscopic scale. For this reason, we use layered GOM being able to tune and control ion transport on different scales exploiting the supramolecular interactions.

The aim of this thesis is the in-depth understanding of the ion transport mechanisms and the charge selectivity in designed nanochannels. This phenomenon will be study in stacked GOM in plane, through GOM:

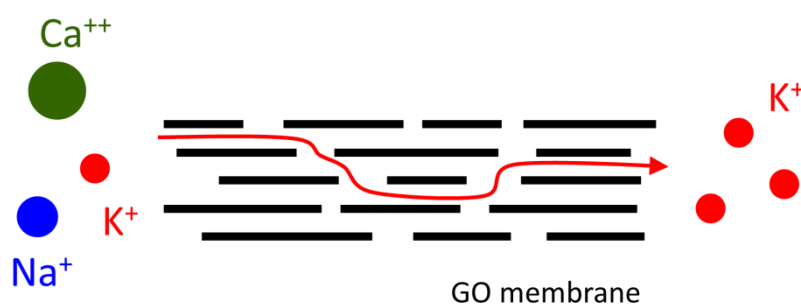


Figure 22. Scheme of transport through GO membranes.

In this thesis, we prepare reproducible GO membranes to study the transport of ions such Na^+ , K^+ , Ca^{2+} , through the membranes in plane applying a negative voltage, and use the technology in biosensors for biomedical applications:

- We produce free-standing GO membranes covered with polymer.
- We investigate the ionic selectivity of the GO membranes by measuring the ionic current of the ion channels under different ion solutions.

3 CHARACTERIZATION & FABRICATION METHODS

The current chapter introduces the characterization techniques that were used during this dissertation (i.e.) principles of work and applications of characterization methods such as Atomic Force Microscopy (AFM), Kelvin Probe Force Microscopy (KPFM) and X-ray Photoelectron Spectroscopy (XPS)

CHARACTERIZATION & FABRICATION METHODS

Brief introduction of techniques [giving structural (1-3), microscopical (4-5) and spectroscopical (6-8) information], simulation (9) and fabrication methods (11).

3.1 X-Ray Diffraction (XRD)

X-Ray Diffraction (XRD) were performed in specular geometry using a SmartLab-Rigaku diffractometer equipped with a rotating anode (Cu $\lambda_{\alpha} = 1.5405$ Å), followed by a parabolic mirror to collimate the incident beam, and a series of variable slits (placed before and after the sample position) to reach an acceptance of 0.09°. (IMM-CNR Bologna. Italy)

3.2 HLPC-MS

The synthesized compounds were characterized by using a HPLC Thermo Fisher Scientific Accela, reverse phase C18 Hypersil Gold column 50x2.1 mm, 1.9 μm , LCQ Fleet ESI/ion-trap mass spectrometer. (ISIS Strasbourg. France)

3.3 NMR

^1H NMR spectra were recorded on NMR Bruker Avance 3, 400 MHz. (ISIS Strasbourg. France)

3.4 Scanning Probe Microscopy (SPM)

Scanning probe microscope (SPM) is a branch of microscopy that forms images of surfaces using a physical tip that scans the sample. Since the probe is given by the interaction between tip and sample, it is possible to map – also simultaneously – different chemical/physical properties of the specimen. SPM family includes tens of different techniques (a.k.a. modes). The first SPM technique is the scanning tunnelling microscope (STM) invented by Binnig and Rohrer in 1982.⁵⁵ (ISOF-CNR Bologna. Italy)

3.4.1 Atomic Force Microscopy (AFM)

After STM, in 1986 Binnig also invented Atomic Force Microscopy (AFM), in collaboration with Quate and Gerber,⁵⁶ which became in few years the most popular SPM mode for creating surface topographical imaging exploiting the Van der Waals forces between a tip with a nanometric apex and the specimen. Due to the short range of the interaction, AFM is successfully used in a wide range of materials (with conductive, semiconductive or non-conductive properties) on nanoscale range. Moreover, AFM can operate in most of environments, such as air, ultra-high vacuum or liquid environments, becoming a useful tool in various disciplines, ranging from physics and chemistry to material science and biology. In order to characterize the surface of desired material, AFM uses an elastic cantilever/tip (general tip length of 100 μm) and measures the interaction force between the tip and the sample² that can be described according to Hooke's law:

$$F = -k \cdot \Delta z \quad (3.4.1.a)$$

In which F is defined as the interaction force, k is the spring constant of the cantilever and Δz is the deflection of the cantilever.

The tip performs a scanning motion on the sample's surface which is thoroughly monitored by a laser beam that is being reflected onto a high-precision position sensitive photo-detector (PSPD). This sensor picks up the changes in the laser reflection, which are referent of vertical and lateral motions of the cantilever (Figure 23). The tip is mounted on a piezoelectric actuator connected to a feedback loop (FL). The latter circuit is responsible for controlling the tip-to-surface distance by maintaining constant the feedback parameter which is responsible of moving the cantilever tip up and down. This parameter is different for each desired topography acquisition mode.

AFM topographies can be acquired in three different modes:⁵⁷ contact, non-contact and tapping modes. As the name suggests, in the **contact mode** the cantilever is kept in continuous contact with the sample while scanning its surface. Two configurations are possible, resulting in z distance parameter controlled by the feedback loop circuit: i) *constant force* in which the cantilever deflection parameter is set by the user, specifying how hard the tip will push against the surface; or ii) *constant height mode*, in which the tip is fixed at a user-specified distance above the sample's surface, and the resulting topography image describes the spatial distribution of the interaction forces. The probe is highly sensitive to the surface alterations in the contact operation mode, and it is usually applied in samples with low surface roughness.

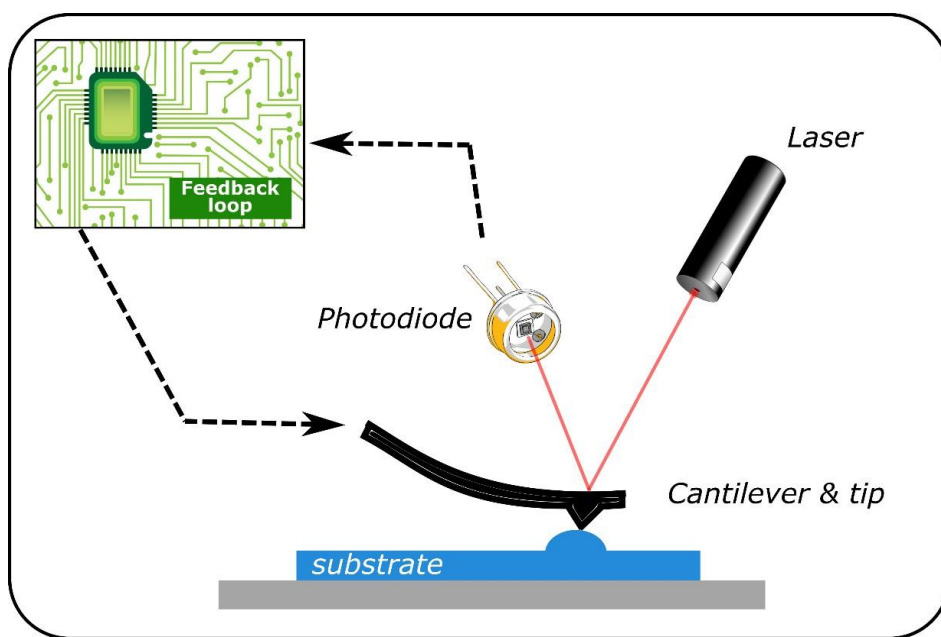


Figure 23. Working principle of AFM; key components are cantilever with tip, laser source, photodiode and feedback loop.

In non-contact mode the cantilever is always oscillating at a fixed frequency above the sample's surface. The feedback loop circuit senses the variations of the oscillating frequency and amplitude which are changed by the interactions of the tip with the surface, thus this method is generally used for sensing the attractive van der Waals interactions and it's suited to the soft materials, since the probability of damaging the sample and/or the tip is quite low.

The mode that was used to obtain the AFM topography images presented in this dissertation is called semi-contact or tapping mode. Here, the cantilever oscillates nearby its resonance frequency and it is fixed above the surface of the sample. Since the movement of the tip is much bigger than in non-contact mode, it is brought in contact with the surface for a short period of time. When compared with the contact mode, this is rather a gentle interaction with the surface, minimizing in this way the torsional forces between the tip and the sample. The user-specified oscillation amplitude of the tip is kept constant by the feedback loop circuit, giving the possibility to tune the interactions between the tip and the sample between the attractive and repulsive regimes. Finally, the voltage variations are recorded throughout the scan and are represented as the topographic AFM image of the sample; as well as the variations in the oscillation phase of the tip that represent the phase contrast imaging.

All the AFM images were acquired using two instruments: i) SMENA solver platform (NT-MDT, Moscow, Russia)⁵⁸ and Multimode 8 (Bruker) processed by Gwyddion⁵⁹ free software version 2.51 and SPIP.

3.4.2 Kelvin Probe Force Microscopy (KPFM)

Developed in 1991 by Nonnenmacher,⁶⁰ KPFM is based on the experiment of Lord William Thomson, as known as Lord Kelvin, who measured the build in contact potential difference (CPD) in metals: i.e. the work function difference between tip and sample.

CPD is measured by recording the electrostatic forces resulting from the interaction between tip and sample. Electrostatic forces, being a long-ranged interaction, do not require a physical contact between the two bodies. KPFM is in fact a non-contact AFM technique based on Zeeman vibrating capacitor set-up where the two electrodes of the capacitor are the sample and an oscillating conductive AFM tip (with defined frequency ω).

In addition to the conventional feedback circuit used to map the topography of the surface with an AFM, a second feedback is exploited to record the local variations in CPD during scanning. Figure 24 shows the operating principle of KPFM.

During the KPFM scan, both an AC- and DC-bias are simultaneously applied to the tip and the first harmonic of the resulting tip-sample capacitive force is

$$F_{\omega} = -\frac{\partial C}{\partial z} [(CPD - V_{dc})V_{ac} \sin(\omega t)] \quad (3.4.2.a)$$

Where V_{dc} and V_{ac} are the static and alternative bias between tip and sample, respectively, and C is the total capacitance of the system.

The feedback circuit is used to nullify the first harmonic term by tuning $V_{DC} = CPD$.

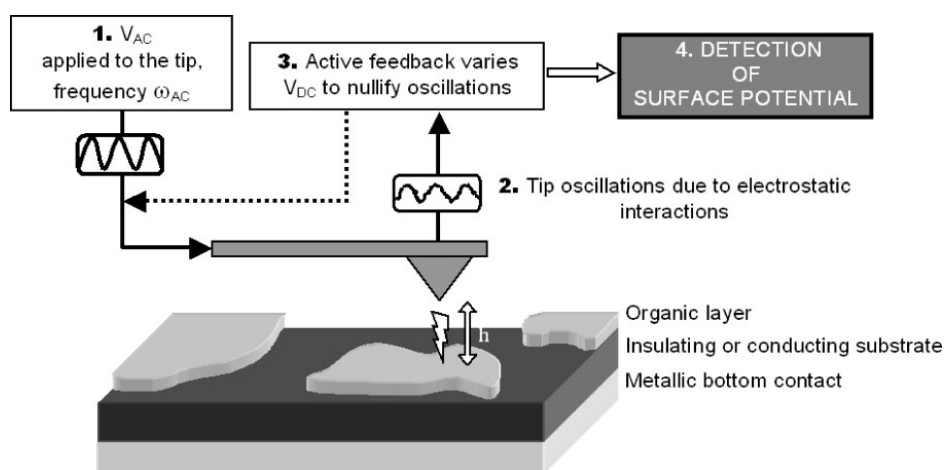


Figure 24. Schematic representation of KPFM.

In this thesis, we used KPFM using the so-called second-modes, where in the first scan is recorded the topography (AFM scan), then in a second one, the tip is lifted up of a fixed distance (lift height) in order to minimize the contribution in the signal of the short range forces. Then when the tip is far enough to the surface a second scan is performed recording the electrostatic forces.

All KPFM measurements were performed in air with a Multimode 8 (Bruker) using Pt/Ir-coated cantilever silicon tips ($k = 2.8$ N/m, Bruker) with oscillating frequencies in the range between 60 and 90 kHz. KPFM images were acquired in

the same measurement; a topographic line scan was first obtained by AFM operating in tapping mode, and then that same line was rescanned in lift mode with the tip raised to a lift height of 20 nm using the amplitude modulation (AM) mode. KPFM allowed mapping the topography and electric surface potential of the sample with a voltage resolution of about 5 mV, whereas the lateral resolution was few tens of nanometers. KPFM can measure the transport and generation of charges in nanometric structures as described extensively in previous works.^{61,62}

Raw AFM and KPFM data were treated by using histogram-flattening procedures⁶³ to remove the experimental artifacts because of the piezoscanners.

3.5 Electronic Microscopy (SEM/EDX)

SEM observations were performed using a Zeiss FEG-SEM LEO 1530 electron microscope at 5 kV and energy dispersive X-ray spectrometer (Oxford INCA) were used for elemental analysis (EDS). (ISOF-CNR Bologna, Italy)

3.6 X-ray Photoelectron Spectroscopy (XPS)

X-ray photoelectron spectroscopy (XPS) – also called Electron Spectroscopy for Chemical Analysis (ESCA) – allows to quantitative analysis of elements and their chemical states of surfaces. Derived from photoelectric effect evidenced by H. Hertz in 1887,⁶⁴ XPS is a *charge-particle*-based chemical analysis technique that is extremely sensitive to the developed electrical potentials due to the uncompensated charges in the sample.⁶⁵ It is used for surface characterization, providing information about presence of the elements on a surface (elemental composition at the parts per thousand range) and giving insight about other elements that they are bounded to.

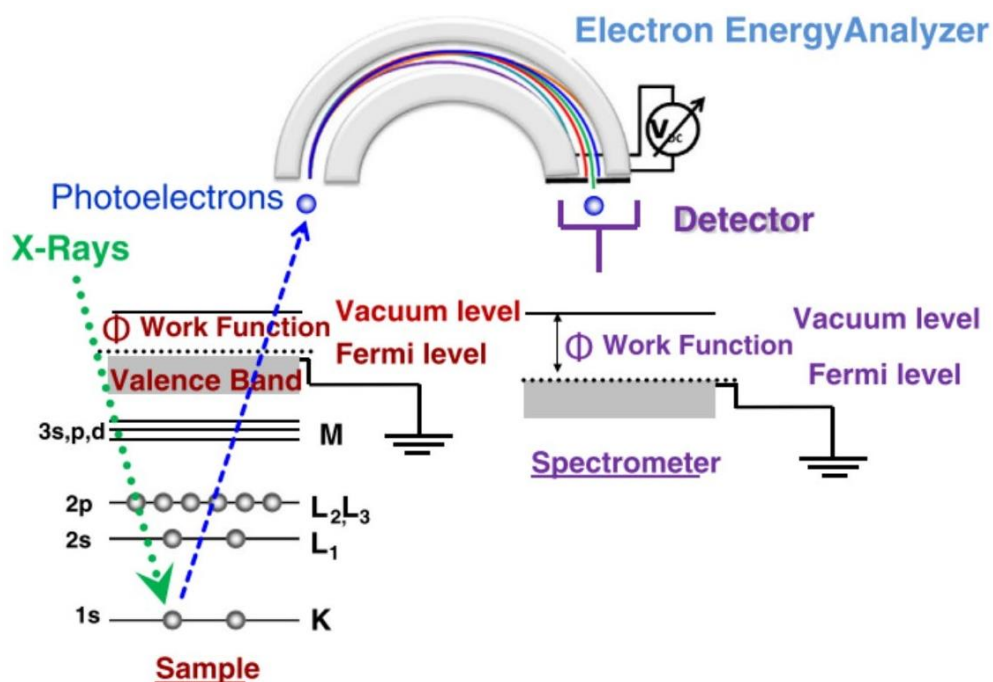


Figure 25. XPS working principle (adapted from⁶⁵): XPS spectra is obtained by irradiating the sample surface with X-rays, while simultaneously measuring the kinetic energy and number of electrons that escape from the top of the surface by means of the Electron Energy Analyzer.

In order to characterize a desired surface, a solid sample is inserted inside a chamber which is constantly kept under ultra-high vacuum (UHV) (below 10^{-8} mbar). UHV assures that there is almost no presence of the adsorbed gaseous contaminants on the sample surface (without interfering with XPS signal in this way) and that the inelastic mean free path of the electrons (defined as the average distance that electrons need to travel before they are inelastically scattered) is enough for allowing them to exit the sample and enter the spectrometer analyzer without changing their kinetic energy (KE). Afterwards, the sample surface is irradiated with X-rays, usually with energies of 1253.6 eV or 1486.6 eV, and the resulting effect is related to the production of multiple ionizations from core and valence energy levels of the irradiated atoms or molecules.⁶⁶ In this manner, it is possible to thoroughly study the photoemission from core level photoelectrons by means of an indirect calculation of the binding energy (BE) of photoelectrons, by

measuring their kinetic energy (KE) using an electron energy analyzer (Figure 25), as described by the equation:

$$BE = \hbar\omega - KE + \Delta WF + V_{bias} \quad (3.6.a)$$

where $\hbar\omega$ is the photon energy, ΔWF is the difference between the work function of the sample and the analyser, and V_{bias} is the electrical potential of the sample which is typically grounded ($V_{bias} = 0$).

The probed depth of XPS is roughly independent on the nature of the sample, and mainly depends on the photoelectron (energy and polar angle). Usually, the XPS can probe samples on depth between 1 and 20 nm, thus this method is usually considered as surface analysis technique.

XPS spectra of all samples were obtained using a Phoibos 100 hemispherical energy analyser (Specs GmbH, Berlin, Germany) and Mg Ka radiation ($\hbar\omega=1253.6$ eV; power = 125 W) in constant analyser energy (CAE) mode, with analyser pass energy of 40 eV. The overall resolution of 1.5 eV was measured and analyser was calibrated using the Ag 3d 5/2 (368.3 eV) and Au 4f 7/2 (84.0 eV) signals from freshly Ar⁺ sputtered samples. Charging effects was corrected by calibration of Binding Energy on C 1s (285.0 eV) for all spectra. (ISOF-CNR Bologna. Italy)

3.7 UV-VIS Spectroscopy

The spectral measurements were carried out in the UV-Vis region using the Perkin-Elmer Lambda 650 instrument over a wavelength range 200–800 nm. Quartz cuvettes were used for measurements in solution with an optical path of 1 cm. The photoisomerization of the studied azo-based compounds was measured in DMF, water and PEG solutions with UV light illumination of intensity 3.2 mW/cm². Trans→ Cis isomerization was induced with a $\lambda=365$ nm (Pd=3.2 mW/cm²), while Cis→ Trans isomerization was induced with a Vis $\lambda=440$ nm (Pd=0.56 mW/cm²), or $\lambda=520$ nm (Pd=2.4 mW/cm²). Light passing through a heat filter (to avoid heat radiation) was directed onto the samples for different time

intervals until they reached the photosaturation. The light intensity on the sample surface was measured with a thermal power sensor (Thorlabs). All UV–Vis spectroscopy measurements presented in this work have been performed under atmospheric pressure.

Reflectometry: The UV–Vis spectra of the solid samples were recorded in the diffuse reflectance mode on a spectrophotometer (Perkin–Elmer—Lambda 650) equipped with a 150 mm integrating sphere (same excitation wavelengths and power used in standard UV-vis spectroscopy, see above). (ISOF-CNR Bologna, Italy)

3.8 Ultrafast UV-VIS Spectroscopy

The pump and probe experiments were performed with a laser system consisting of a 800 nm, 1 kHz chirped pulse amplifier seeded by a Ti:Sa oscillator. The pump pulses (385 nm and 410 nm) were produced in an Optical Parametric Amplifier pumped by the amplifier. The probe is a white light supercontinuum (350 – 800 nm) generated in a commercial Transient Absorbance (TA) spectrometer (FemtoFrame II, IB Photonics), by focusing the 800 nm radiation of the amplifier into a rotating CaF₂ crystal.

The optical layout of the TA spectrometer consisted of a split beam configuration in which 50% of the white light passes through the sample solution contained in a 1 mm static cell, while the remainder is used as a reference to account for pulse to pulse fluctuations in the white light generation. The pump pulse is focused (circular spot of diameter = 400 μm) onto the sample with an energy density of 280 $\mu\text{J}/\text{cm}^2$. The spot diameter of the probe pulse is approximately 150 μm , and its time delay with respect to the pump pulse is scanned in time by varying the length of its optical path.

The instrument response function (IRF) was measured to be approximately 50 fs. All measurements were performed in air at room temperature. More

experimental details on the set-up can be found in previous works.^{67,68} (ISM-CNR Rome, Italy)

3.9 Computational Calculations (DFT)

Ground state properties and molecular geometries relaxations were calculated at Density Functional Theory (DFT) level of theory within the Becke, 3-parameter, Lee-Yang-Parr (B3LYP) functional⁶⁹ and 6-31G(d,p) basis set. The calculation of the excited state properties has been done by means of Time-Dependent DFT (TD-DFT) calculations on the previously optimized structures. This functional and basis set have been successfully applied in the description of the excited states in similar azobenzene based compounds.^{70,71} The effects of the solvent have been introduced in our calculations by the Polarizable Continuum Model (PCM).⁷² All the theoretical calculations presented in this work have been performed within Gaussian16 package program.⁷³ (Laboratory for Chemistry of Novel Materials - University of Mons, Belgium).

3.10 Electrochemical Characterization.

The electrical characterization of the devices presented in this thesis was performed with an Agilent B2912A Source-Measure-Unit (SMU), shown in Figure 26, that features two channels for independently sourcing voltage/current and measuring current/voltage. Each channel features 6 banana outputs, which are converted to two triaxial outputs (Low and High Force) by means of Agilent N1294A adapters; the low terminal can be grounded to the chassis of the instrument or left floating. Triaxial cables are used to connect, by means of feedthroughs, coaxial probes that are inside a Faraday cage to the SMU terminals. Custom-made software controls both channels of the SMU and allows the analysis with the pulse method. Figure 26d shows an example of the user interface of the software.

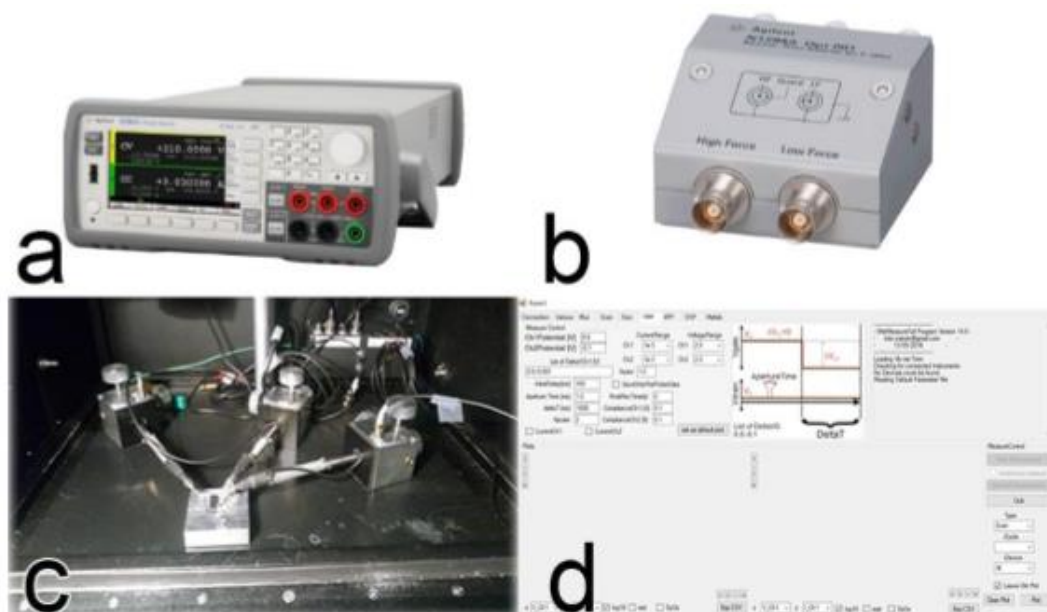


Figure 26. a) Agilent B2912A SMU; b) Agilent N1294A banana-to-triax adapters; c) sample holder and contact probes inside the Faraday cage; d) user interface of the SMU.

AUTOLAB: Pulse Method

Further measurements were acquired by using the modular Autolab/PGSTAT128N, is a low noise and fast potentiostat/galvanostat capable of measuring maximum 800 mA (10 A with BOOSTER10A), with a compliance voltage of 12 V. The electrochemical cells used for the measurement tests contained three electrodes per cell, the reference electrode (RE), the working electrode (WE) and the counter electrode (CE). (LEO-UNIMORE. Italy)

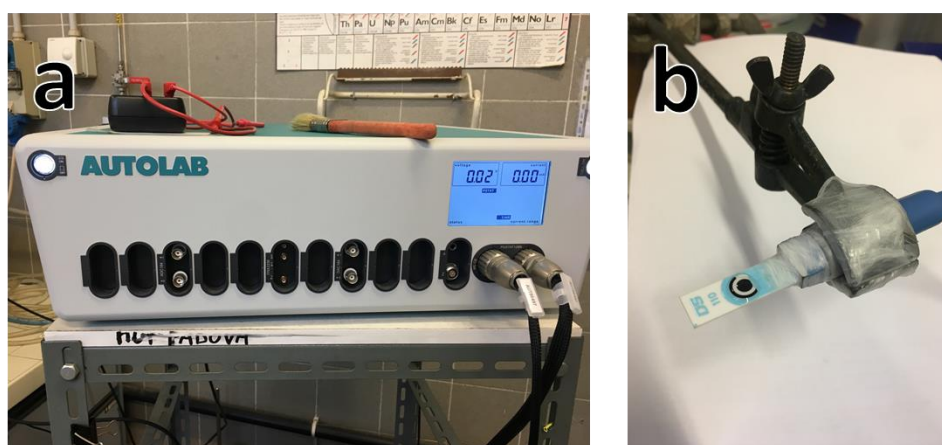


Figure 27. a) Autolab b) sample holder with an electrode for pulse method.

3.11 Fabrication Methods

During this thesis several fabrication techniques and methods has been employed in the development of the devices and preparation of samples.

3.11.1 3D Printer

Additive Manufacturing (AM) also known as three-dimensional (3D) printing has been introduced in 1980s and has been growing rapidly since.⁷⁴ It has a wide range of applications in different areas, starting from physical prototyping of mechanical parts up to 3D tissue printing in health-care products.^{75,76} The 3D printer of choice was **B9Creator® V1.2HD**, featuring high-precision characteristics: i) Z resolution: 25-100 microns; iii) XY resolution: 30/50/70 microns (multiple configurations); iv) full HD projector resolution: 1920 x 1080 (1080p); v) build volume: 57.6 x 32.4mm at 30 μm x - y ; 96 x 54 mm at 50 μm x - y ; 104 x 76.6 mm at 70 μm x - y . Figure 28 represents this Digital Light Processing (DLP) 3D printer.



Figure 28. 3D printing process: from 3D CAD design to the printed object.

Drawings of the desired 3D model are made in CAD software and imported to the printer. This type of 3D printer works with liquid photopolymers (resins) which are contained inside a resin reservoir. It uses a conventional light source to project an entire slice/layer of the 3D model and solidify it on

the build table which slowly moves up when each consecutive layer is being projected. By the end of the manufacturing process, the desired model is entirely printed (Figure 29).

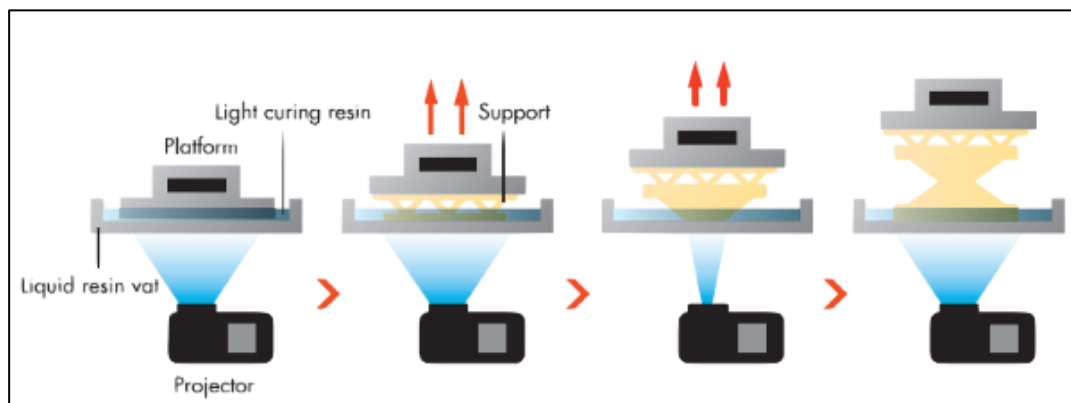


Figure 29. DLP printing technique.⁷⁷

High resolution, ranging up to 30 μm on XY and Z axis and fast printing creates almost unlimited possibilities for the high precision prototyping. (Scriba Nanotechnology-Bologna. Italy)

3.11.2 Spin Coating

Spin coating is one of the most used techniques for deposition of thin film on the substrate. By spinning the substrate, it uses centrifugal forces in order to evenly spread the solution over the substrate, creating a uniform film and expelling the excess of solution.⁷⁸

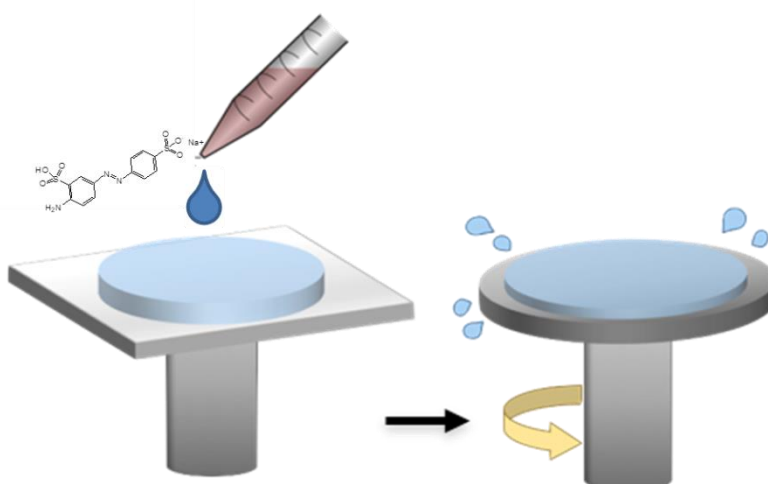


Figure 30. Spin coating technique.

Since some of the materials in organic electronics are in liquid form, the method of spin coating has been widely employed for semiconductor or polymer deposition on a substrate. On the spin coater, parameters such as acceleration, speed, spin duration and deceleration can be tuned to achieve the desired film thickness. Rheological properties, such as viscosity, thixotropy (liquid's capability to shear thin); appropriately matching the surface tension with the substrate and the solvent evaporation rates are of critical importance and should be considered when designing the spin-coating profile for obtaining the desired thin film in nm to higher thicknesses and reproducibility. At the end of spin coating, the sample can be cured by a method of choice (UV, electron-beam, thermal, etc.) and then patterned where necessary.



Figure 31. Laurell WS 400B-6NPP/LITE spin coater.

In order to obtain the desired film thickness, parameters such as the angular velocity and concentration (or viscosity) need to be taken into consideration, since they are shown to be correlated to the final film thickness.⁷⁹ Thus, thickness of the film (h) depends on the rotation speed of the substrate (ω)

as determined by the phenomenological equation:

$$h = k_1 \cdot \omega^\alpha \quad (3.11.2.a)$$

where ω is the angular velocity, while k_1 and α are empirically determined constants.

Some of the organic semiconductors and polymers used in this dissertation were in liquid form, thus Laurell WS 400B-6NPP/LITE (North Wales, USA) spin coater was one of the chosen instruments for organic molecules deposition over the substrates. (ISOF-CNR Bologna. Italy)

3.11.3 Drop-Casting

A solvent-assisted drop casting is a very straightforward technique for creation of semiconducting thin-films on the substrate. It allows one to lower the rate of film formation by creating a solvent rich and/or higher temperature environment, factors which contribute to improve the multiscale morphology of the film, thus increasing the performance and stability of the final device.⁸⁰ The angle of the support on which the substrate is fixed can be as well manipulated. (ISOF-CNR Bologna. Italy)

4 GOM: EXPERIMENTAL ACTIVITIES

The current chapter introduces the experimental GOM activities: preparation of the membrane, chemical characterization, set-up for ion transport, pulse method measurements and results.

4.1 GO Preparation & Chemical Characterization with XPS

Graphite was oxidized by a modified Hummers method to obtain water-soluble graphite oxide.⁸¹ Briefly, graphite (100 mg) and sodium nitrate (100 mg) were added into 5 mL of fuming sulfuric acid (97-98%). Then, solid potassium permanganate (1 g) was slowly added to form the green manganate dimer (Mn_2O_7). The mixture was stirred for 3 days, diluted with sulfuric acid (5%; warning: this has to be done with extreme caution; the process is highly exothermic) and heated for 3 h to about 100-120 °C. After slow addition of 1 mL of hydrogen peroxide (30%), the resulting solid was collected by centrifugation and washed five times with sulfuric acid (3%) and hydrogen peroxide (3%), two times with hydrochloric acid (3.7%) and two times with water. Ions remaining in the solution were removed by dialysis against ultrapure water (3 days; water was changed every day). The water was removed by lyophilization to yield ~50 mg of water-soluble graphite oxide in the form of a light brown powder. The purity was checked by elementary analysis. The amount of sulfur, nitrogen and chloride was under wt 0.1% each. Solutions of exfoliated GO are obtained by dissolving small amounts of graphite oxide in water (e.g. 0.5 mg/mL).

Characterization

The uniformity of the film was confirmed by SEM measurements performed on the electrodes after coating (Figure 32). In particular, a flat morphology was observed, with ripples and folds typical of 2-dimensional materials, significantly different from the morphology of the uncoated substrate.

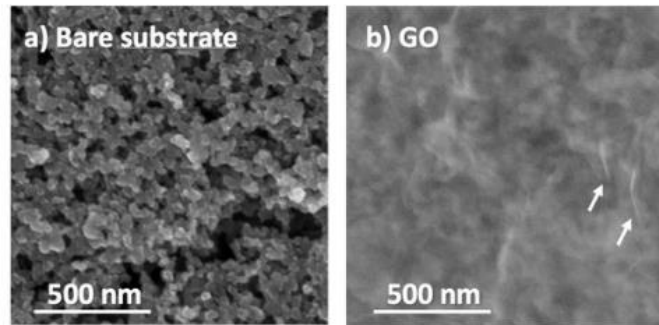


Figure 32. FEG-SEM images collected by secondary electrons at (a) bare substrate (b) GO. White arrows indicate ripples typical of 2-dimensional nanosheets.

The pristine GO is mainly composed by Carbon and Oxygen, Sulphur and Nitrogen are present in small amounts. The Carbon to Oxygen ratio of GO is usually between 2 and 3, the GO used in present work has $C/O = 2.4 \pm 0.2$. The O/C ration can be obtained by the ratio of C 1s and O 1s areas, by taking into consideration the relative sensitivity factors, the transmission of the analyser and the inelastic Mean Free Path of photoelectron in the photoelectrons. The C/O ratio can be obtained also from the fit of C 1s peak, in case of GO the C/O ratio from fit is 2.7 ± 0.2 .

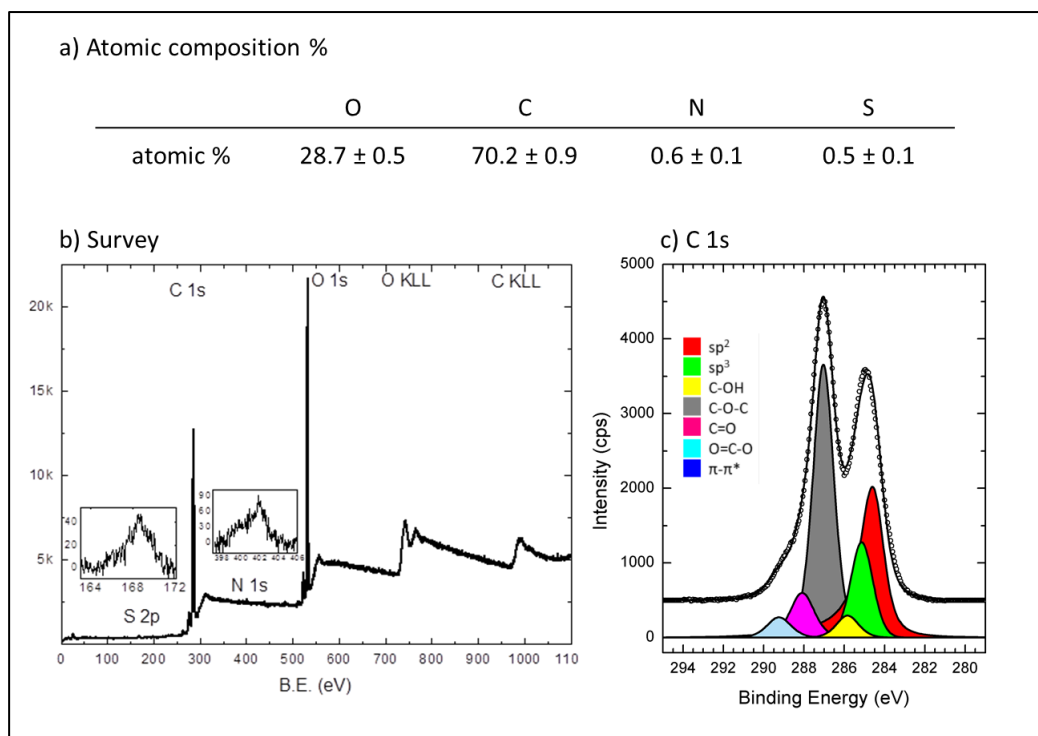


Figure 33. XPS spectra of GO. a) Atomic concentration of GO measured by XPS; b) survey spectrum and high-resolution C 1s spectrum of GO.

4.2 Membrane Preparation

Preparation and characterization of GO membranes

The aqueous suspension of GO was prepared by dispersing GO flakes in distilled water using bath sonication for 4 hours. The resulted suspension was filtered onto an anopore inorganic membrane composed of aluminum oxide by vacuum filtration method ($0.02 \mu\text{m}$, diameter 47 mm, purchased from Whatman). The membranes were fished and cut into rectangular strips of dimension of $3 \times 1 \text{ cm}$. The strips were then covered with a $500 \mu\text{m}$ PDMS slide both sides by an *in situ* cross-linking using a Film Applicator and Drying Time Recorder Coatmaster 510.

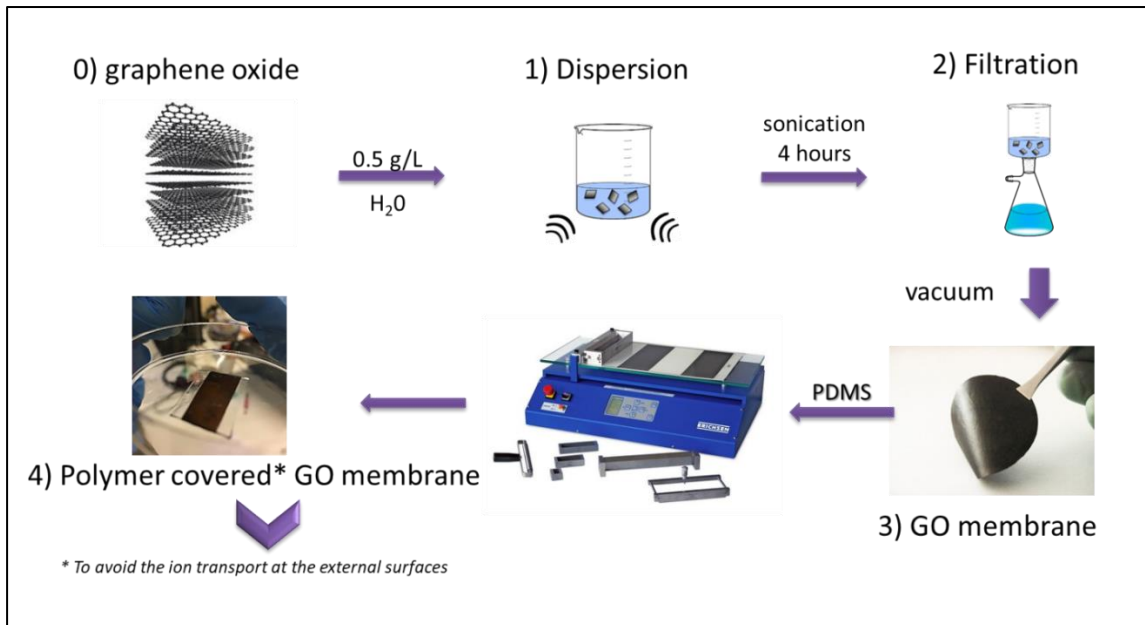


Figure 34. Scheme of membrane fabrication.

PDMS was mixed in a 1:10 ratio in weight of Sylgard 184 Silicone Elastomer Curing Agent and PDMS monomers. The mixed ingredients were placed in a vacuum chamber for degassing under vacuum pressure for 30 minutes.

PDMS was used for preventing the transport of ions on the surface of the membrane and the disintegration of the GOM in water. It is a polymer widely used for the fabrication and prototyping of microfluidic chips. Apart from microfluidics, it is used as a food additive (E900), in shampoos, and as an anti-foaming agent in beverages or in lubricating oils. It is transparent at optical frequencies (240 – 1100 nm), it has a low autofluorescence, it is considered as biocompatible (with some restrictions), and it is deformable, which allows the integration of microfluidic valves using the deformation of PDMS microchannels. It is easy to mold, because, even when mixed with the cross-linking agent, it remains liquid at room temperature for many hours.

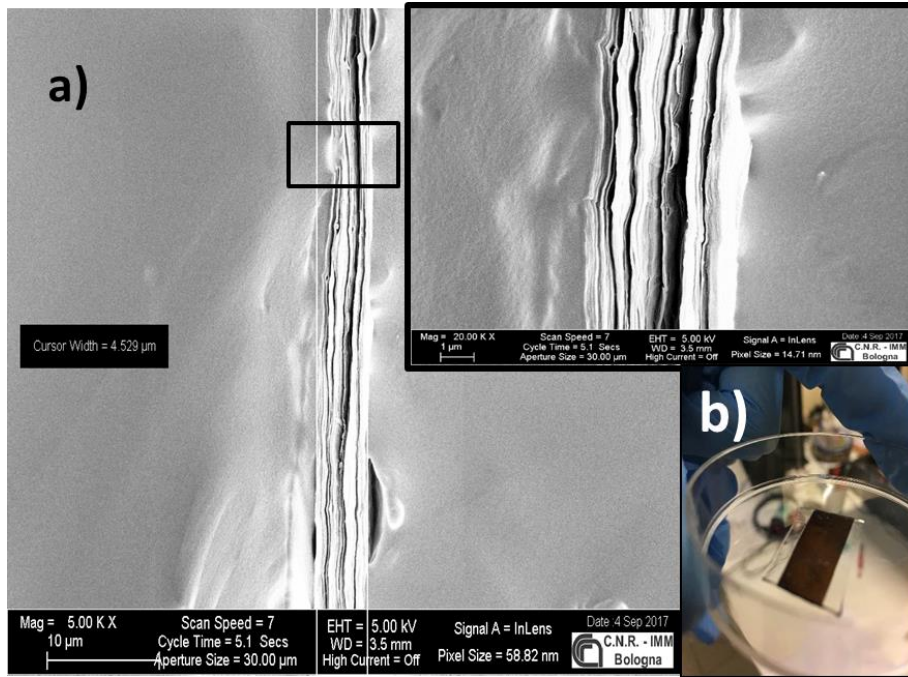


Figure 35. a) SEM images of obtained GO membranes after coverage with PDMS polymer and zoom b) Photograph showing GO nanofluidic device.

SEM analysis of obtained GO membranes

The thickness of the membranes can be tuned by varying the GO concentration in water. The measurement of the thickness has been performed by SEM imaging of the membrane cross-section, as depicted in figure 36.

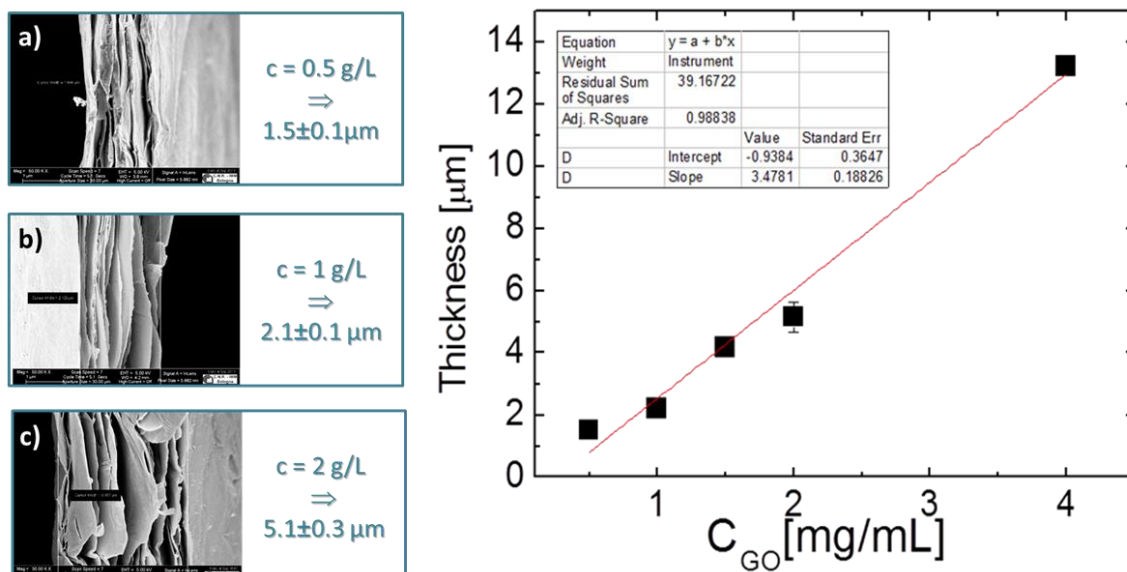


Figure 36. Left: SEM image of the cross-section of GOM. a) $c = 0.5 \text{ g/L}$; $1.5 \pm 0.1 \text{ } \mu\text{m}$, b) $c = 1 \text{ g/L}$; $2.1 \pm 0.1 \text{ } \mu\text{m}$, c) $c = 2 \text{ g/L}$; $5.1 \pm 0.3 \text{ } \mu\text{m}$. The error was calculated with 4 membranes for each concentration of GO. Right: Tuning of the thickness, membrane thickness vs GO concentration. Red line is the calibration curve calculated by the fit.

The correlation of thickness of the membrane and the concentration of GO is linear, meaning the production of the GOM is reproducible.

4.3 Chemical Analysis of GOM

The chemical analysis of GO were performed using XPS. Sample were prepared by mechanic peeling of the upper PDMS layers of PDMS/GO/PDMS membrane after 2 hours of bias; pristine GO and pristine membrane on PDMS were measured. Base pressure in the analysis chamber during analysis was $5 \cdot 10^{-10}$ mbar. Data analysis and fitting were performed with CasaXPS software, after Shirley background subtraction.

Peak positions of the non-equivalent carbon species, based on literature data, were: aromatic carbon (C=C sp², 284.4 eV), aliphatic carbon (C-C sp³, 285.0 eV), hydroxyl (C-OH, 285.7 eV), epoxy (C-O-C, 286.7 eV), carbonyl (C=O, 288.0 eV) and carboxyl (O-C=O, 289.1 eV).⁸² All line-shape were voigts, the only exception was the asymmetric pseudo-voigt used for sp² aromatic carbon. All the doublets were fitted by a doublet with fixed spin orbit split of for Si 2p (0.63 eV), Ca 2p (3.60 eV), K 2p (2.77 eV), Cl 2p (1.6 eV) and Br 3p (1.05 eV) and a fixed area ration between the two components.

The same measurement was performed at PDMS/GO/PDMS membrane, after the peeling of the upper PDMS layer: the C/O ratio seems to increase, but extra amount of Carbon comes from the residual of PDMS. The formula of PDMS's monomeric unit is -SiO(CH₃)₂-, the amount of Si 2p signal is proportional to the amount of PDMS, which is about 13.9%. Silicon is present in all samples and can be associated to PDMS, moreover, a slight amount of Al (Al 2p 1.8%) is present to due to a residual of Alumina filter used for the preparation of GO membranes.

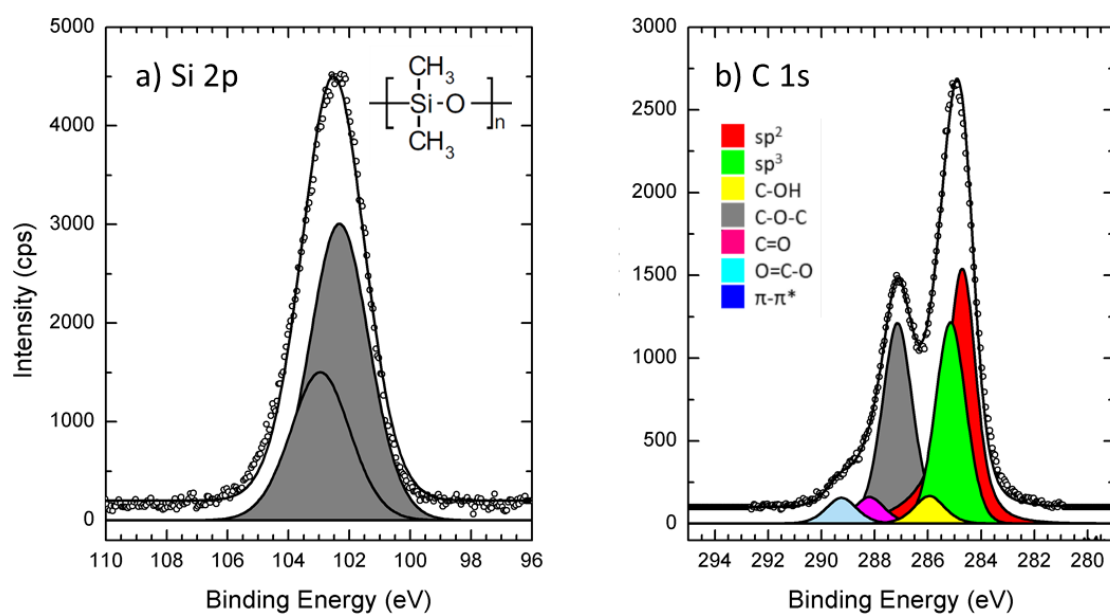


Figure 37. XPS spectra: A) Si 2p and b) C 1s of GO on PDMS.

4.4 Set-up for Electrochemical Measurements

The experimental set-ups for electrochemical measurements were developed in Laboratorio di Elettronica Organica (LEO), UNIMORE. The scheme is simple: two “vials”, one with water/salt and the final with pure water are bridged by GOM, as shown in figure 38. The ions were forced to go through GOM by an external potential bias: one electrode set in the “initial” Petri is grounded. Cation moved when the other electrode is negative polarized, otherwise anion in the case of positive polarization.

The list of the investigated ions is reported in Table 1.

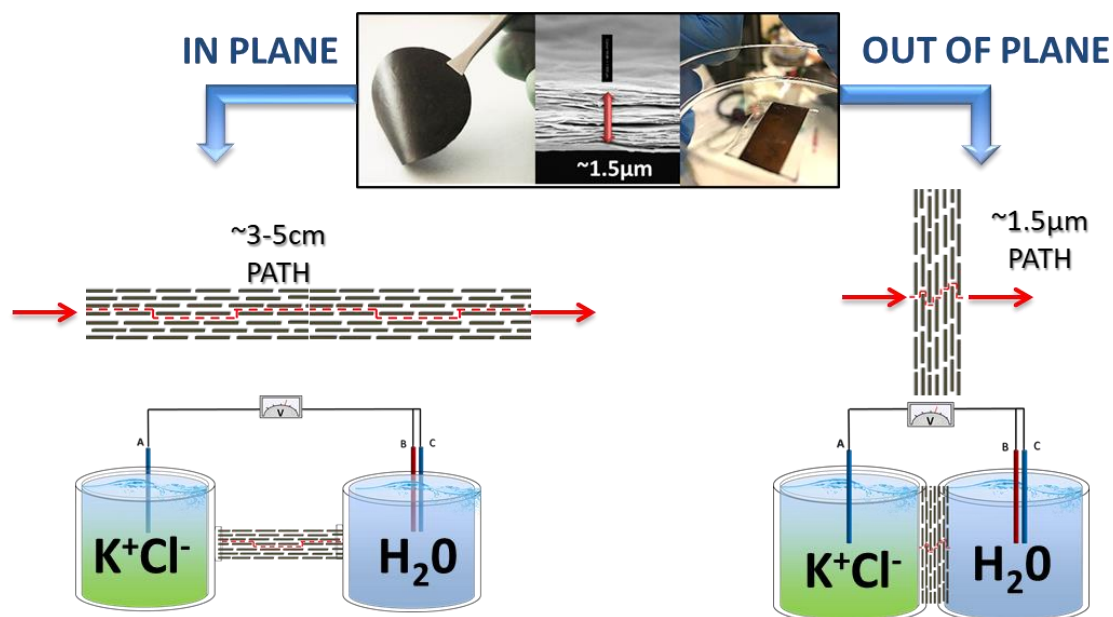


Figure 38. Scheme of the set-up for ion transport in plane and out of plane.

Table 1. Parameters of the ions under study and the salt used in the experiments. * The parameter *Calculated Effective Density* ($C/\text{\AA}^3$) is an estimated value of number of charge / hydrated volume.

Ion	Li ⁺	Na ⁺	K ⁺	Mg ²⁺	Ca ²⁺	F ⁻	Cl ⁻	Br ⁻
Used salt	LiCl	NaCl	KCl	MgCl ₂	CaCl ₂	KF	KCl	BrK
Ionic radius (pm)	76	102	138	72	100	133	181	196
Crystal radius (Å)	0.60	0.95	1.33	0.65	0.99	1.36	1.81	1.95
Stokes radius (Å)	2.38	1.84	1.25	3.47	3.10	1.66	1.21	1.18
Hydrated diameter (Å)	7.64	7.16	6.62	8.56	8.24	7.04	6.64	6.6
Paulings Electronegativity (X)	0.98	0.93	0.82	1.31	1	3.98	3.16	2.96
$V=4/3 \pi r^3$ (Å ³)	2.33496 E+02	1.92193 E+02	1.51905 E+02	3.28413 E+02	2.92941 E+02	1.82691 E+02	1.53286 E+02	1.50533 E+02
Calculated Effective Density* ($C/\text{\AA}^3$)	6.86094 E-22	8.33537 E-22	1.05461 E-21	4.87801 E-22	5.46868 E-22	8.76892 E-22	1.04510 E-21	1.06422 E-21
Charge densities ($C \text{ mm}^{-3}$)	52	24	11	120	52	24	8	6

We developed a three electrodes set-up based on Pulse method in order to:

- i) Apply a DC bias between two Petri dishes and
- ii) Measure the concentration of the ion passed through the GOM.

The scheme is reported in figure 39.

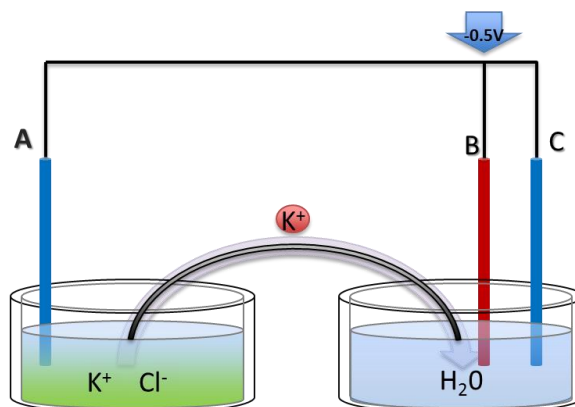


Figure 39. Set-up scheme: Chanel 2; A-B: biasing; VA-B: Voltage to transport ions.

Experimental conditions:

Petri 1: KCl 0.1M/ CaCl₂ 0.1M; Petri 2: DI water; V_B: -0.5V; Membrane: GO 1.5±0.1 μm (hydrated before use). Time of biasing/step: 20min; Total time of biasing: 80min. Volume solution: 10 mL.

Pulse-method:

The pulse-method consists in apply a DC bias between two electrodes A and B to drive the ions from one petri to the other through the GOM (from the salt petri to the DI water petri); the typical biasing time is 80 minutes, and the voltage ±0.5V.

The measurement of the ion concentration in the final Petri dish is performed by using a further electrode, called C in figure 39, and applying a further pulse bias between B and C. The duration of the pulse is 1 second and does not perturb the ion concentration in the dish.

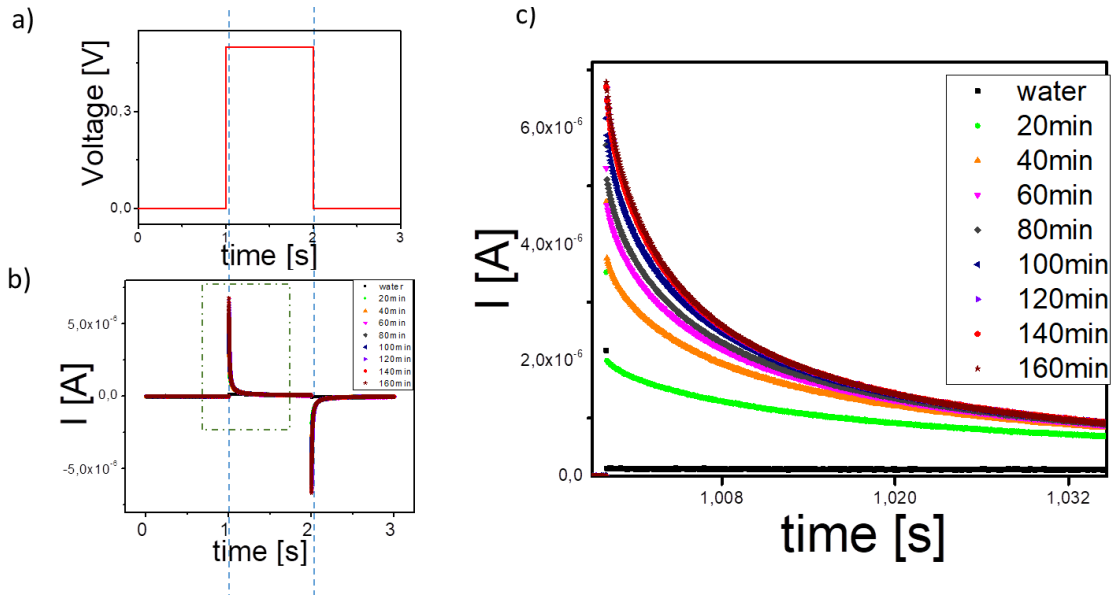


Figure 40. a) Applied pulse in BC. b) transient displacement current (I_{displ}) versus time. c) Zoom.

As it is shown in Figure 40a), a short pulse was applied in BC every 10 minutes (in the petri dish with DI water) to measure the current in that vial. While in figure 40b) is possible to observe the increase of the current in the final vial (I_{BC}) with time (meaning the increasing of salt concentration due to the increased presence of ions). Afterwards the maximum point of each curve (the maximum current) can be correlated with the concentration of the ions, giving information about how many ions are actually travelling through the GOM.

Capacitive current: The current flow onto a capacitor equals the product of the capacitance and the rate of change of the voltage:

$$I = C \frac{dV}{dt}; \quad C = A \frac{\epsilon \epsilon_0}{\lambda_D}; \quad \lambda_D \propto \frac{1}{[M]} \quad 4.4.a$$

In which ϵ_0 is the value of the permittivity for air which is $8.84 \cdot 10^{-12}$ F/m, and ϵ is the permittivity of the dielectric medium used between the two plates with area A.

When a bias is applied between the two electrodes, ions flow from one petri dish to the other. The fitting follows the following equation (drift-diffusion):

$$I = I_0 + I_{displ} \times \left[1 - e^{-(t/\tau)^\alpha} \right] \quad 4.4.b$$

where the transient displacement current (I_{displ}) corresponds to the gate voltage

ramp rate (dV_G/dt). I_{displ} is the current value corresponding to the asymptotic limit, where there is not any variation of the current. It is the maximum of current, as can be observed in Figure 40c.

Thus, the transient displacement current as a function of KCl solution, which is proportional to the concentration, is also included for comparison. (Each concentration was measured 6 times to calculate the errors) The following graph shows a different behaviour between the diffusion of K^+ and Ca^{2+} .

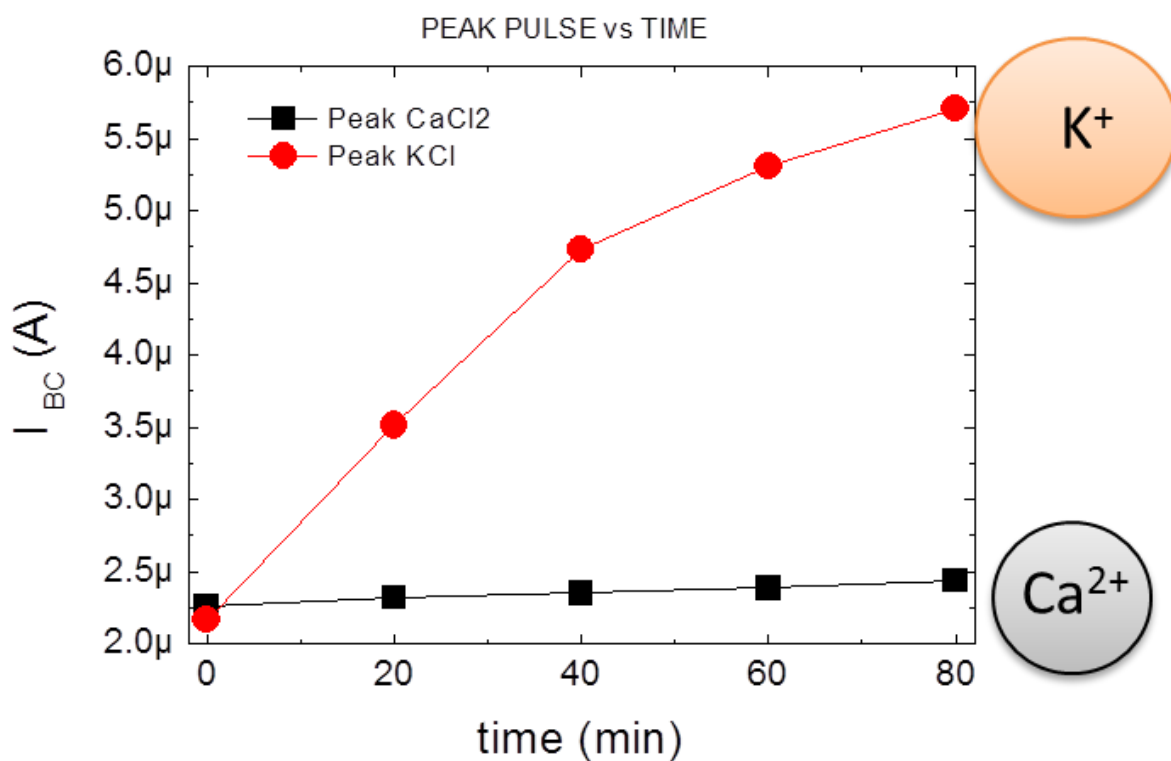


Figure 41. Transient displacement current (I_{displ}) versus time for KCl and $CaCl_2$. Fitted with equation 4.4.b.

- Reproducibility Testing :

To ensure the reproducibility of the method, this was repeated on different days, with different ion solutions and different membranes.

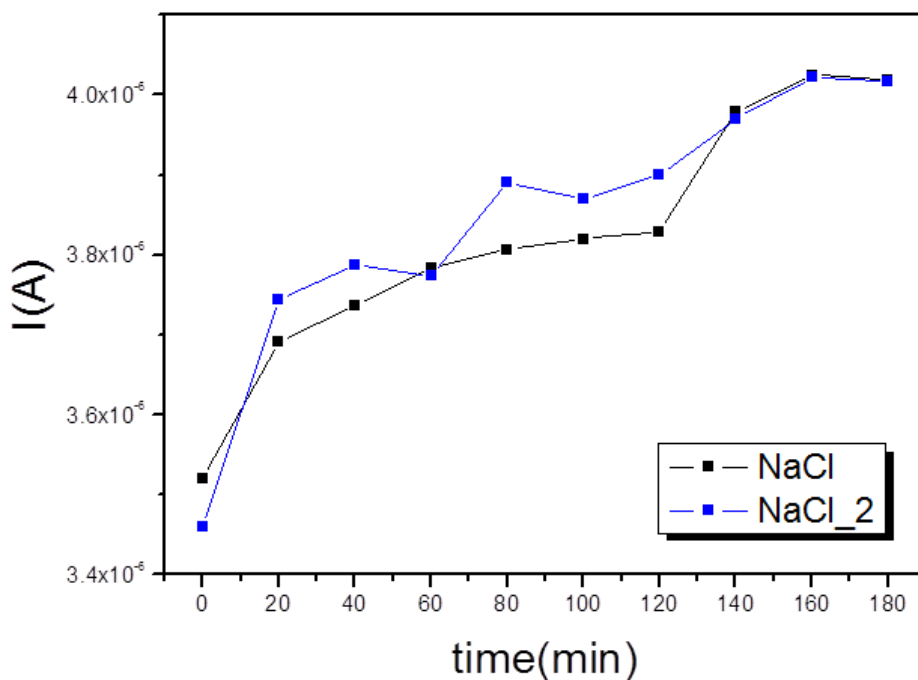


Figure 42. Transient displacement current (I_{displ}) versus time for 2 different solutions of Na^+ (petri dish A, conc = 0.1 M), with same concentration but different days and membranes.

To correlate the previous current with the concentration of the ions, the following calibration curve was performed which shows a sensitivity of 0,001 mM K^+ . (Each concentration was measured 6 times to calculate the errors).

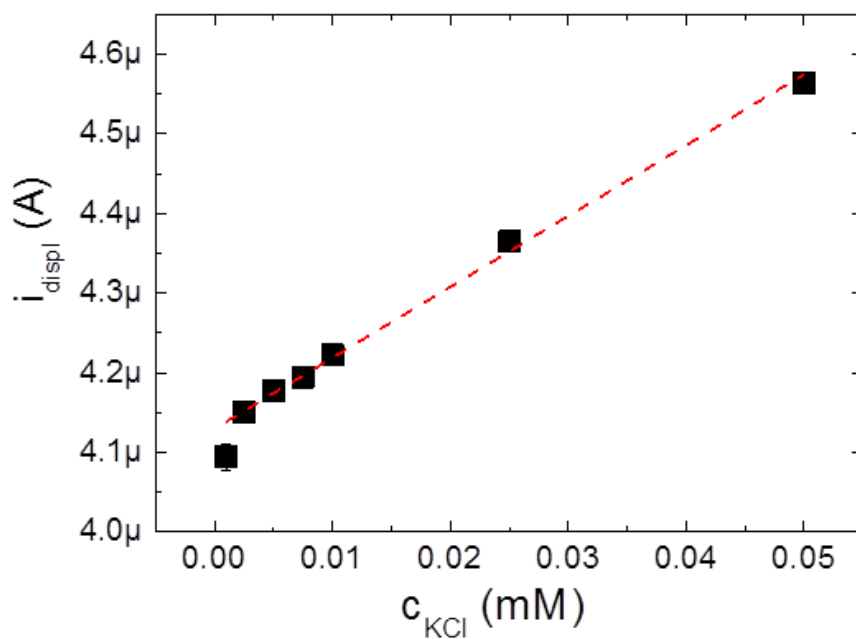


Figure 43. Correlation of the transient displacement current (I_{disp}) and the concentration of KCl.

Conclusions

- Current signal does not depend on intervals between sampling time (i.e. 10 min = 20 min)
- Reproducibility = range 0.1 uA
- Sensitivity= 0.001mM ion

4.4.1 Set-up Out of Plane

For out of plane transport the follow set-up was used. Two vials connected by a membrane holder which place the membrane in vertical position.

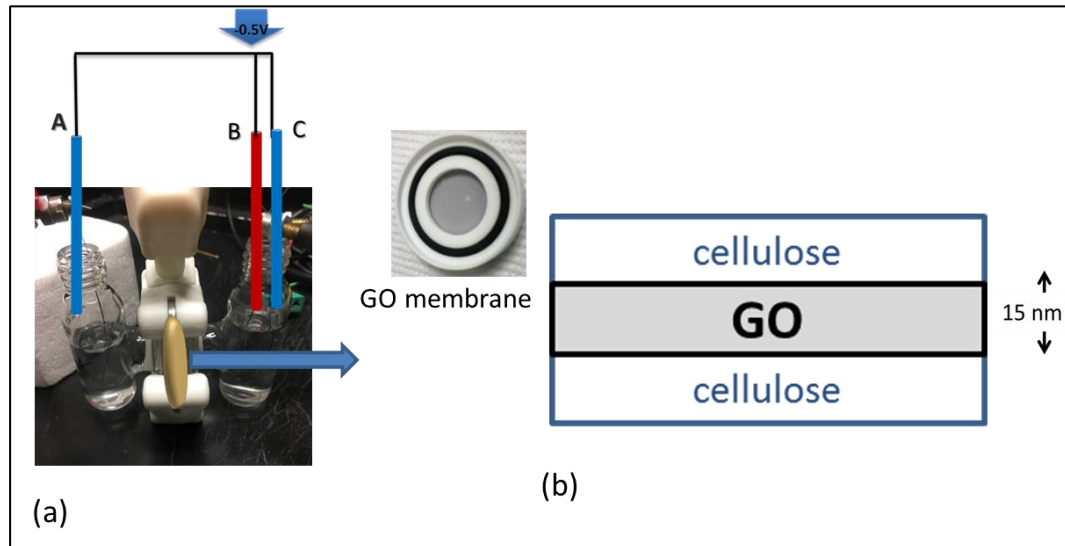


Figure 44. (a) Photograph showing GO out of plane device. (b) GO strip membrane covered with cellulose to prevent GO degradation.

To avoid the degradation of the GOM, it was covered with a cellulose layer which does not interfere in our purpose.

The electrochemical measurement is the same explained above for in plane system.

4.4.2 Set-up in Plane

Preliminary set-up

We built a set up in where we had two petri dishes, one with salt and one with DI water. A bias (negative voltage) was applied on the petri with DI water, and the GO membrane was acting as a bridge to transport the cations from one side to the other:

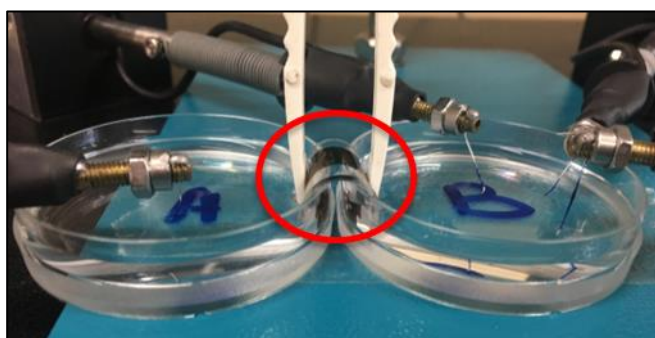


Figure 45. Picture of the preliminar experimental set-up. Petri A: KCl 0.1M; Petri B: DI water. Volume: 10mL.

To decrease the noise and increase the reproducibility we reduced the system to only 2 electrodes and 2 channels.

3D-printed set-up

Once we demonstrated that our system worked, we designed a 3D printed device in order to:

- Have more electrical stability
- Have a fixed geometry to reduce noise and increase the reproducibility
- Reduce the dimensions (LEGO size: 4×2×1.6 cm)
- Have a fixed volume: 4mL

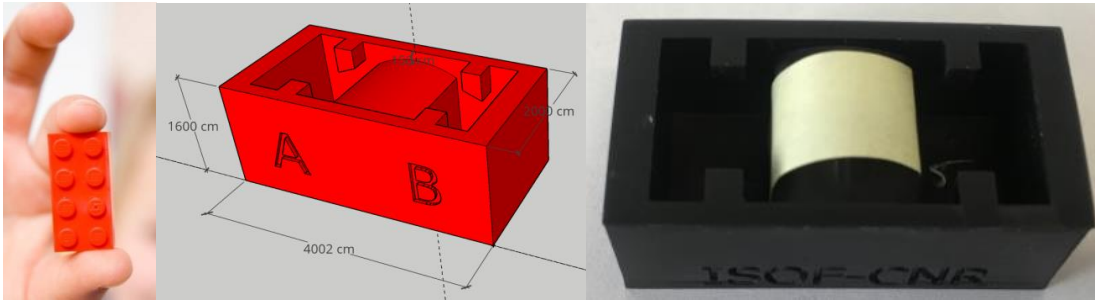


Figure 46. Design of the device built with B9Creator® V1.2HD. *Dimensions divided by 1000.

The result was the following compact and portable device, which will be used in all further analysis.

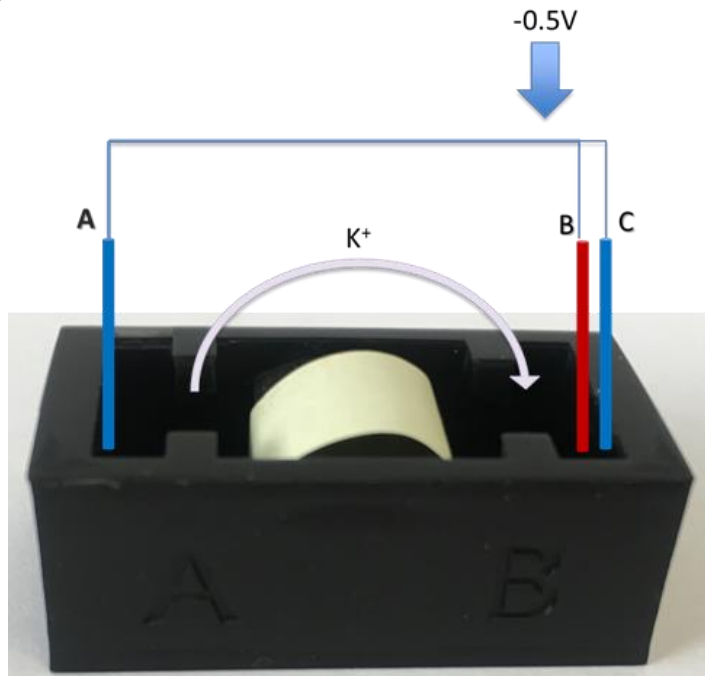


Figure 47. Scheme of the final set-up created by 3D printing.

4.5 Results and Conclusions

As described in the previous paragraphs, GOMs form a uniform laminar structure with a well-defined interlayer space, and they have been studied extensively for applications such as nanofiltration and pervaporation. Though the interlayer space of the GOMs has endowed the membranes with excellent molecular and ion sieving properties,⁸³ where the rejection of small molecules in

nanofiltration was mainly through size exclusion.^{84,53}

The typical set-up to study the ion sieving is related to the so-called pressure-driven permeation, where the water permeation is given by the hydraulic pressure applied (typically < 10 bar), as shown in figure 48).

In this thesis, we focused on the analysis of the ion transport in static condition of water flow. The amount of the ion charges passed through the membrane was monitored without applying any driving-force, such as hydraulic or osmotic pressure due to the presence of meniscus. GOM was completely wetted connecting two Petri dishes (figure 45) and ions were forced to diffuse through the membrane because of a potential bias without any moving of water.

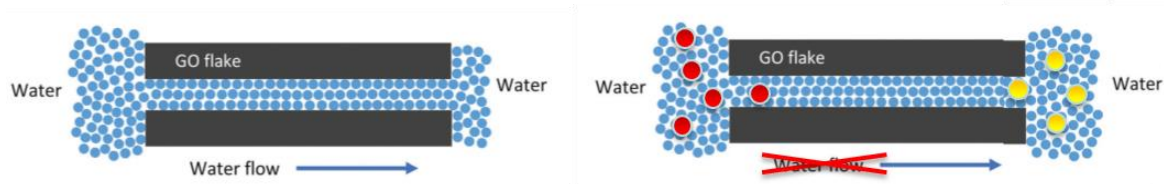


Figure 48. Illustration of the transport mechanisms in the nanochannels in GOMs under the (a) pressure-driven permeation of water, as typically used in ion sieving set-up and (b) Ion flow due to the potential bias applied, as we performed in this thesis.

4.5.1 Ion Transport, a Brief Introduction

The diffusion of ions (or molecules) is due to their random motion in a medium (i.e. water in our case) is described by the two Fick's Laws. The first one describes the tendency of ions to move from regions of higher concentration to regions of lower,^{85,86} and is written as:

$$J_D = D\nabla C \quad (4.5.1.a)$$

where J_D is the diffusive flux density, D is the diffusivity, and C is the concentration. The time dependence of the concentration – called Fick's second law – is obtained from the divergence of the flux density:

$$\frac{\partial C}{\partial t} = D\nabla^2 C \quad (4.5.1.b)$$

D depends on the microstructure in which the material is diffusing in (i.e. water in GOM in our case which can differ from the case of pure bulk water).

In the case of a 1D channel with infinite length and for a given solution with concentration C_0 , the equation 4.2 assumes the form:

$$C(x, t) = C_0 \cdot \left[1 - \operatorname{erf} \left(\frac{x}{2\sqrt{Dt}} \right) \right] \quad (4.5.1.c)$$

where x is the position along the channel and erf is the well-known Erf function – a.k.a. Gauss error function – available from standard mathematical tables or computer programs.⁸⁷

Electrically-driven diffusion

The dispersion of a dilute solution of ions when driven by an applied electric field is described by

$$\frac{\partial C}{\partial t} + \vec{v}_E \cdot \nabla C = D \nabla^2 C \quad (4.5.1.d)$$

The ion velocity \vec{v}_E driven by an electric field E , is given by $|\vec{v}_E| = \mu z F E$, where μ is the ion mobility, z is the ion charge number, F is Faraday's constant. The solution of the above equation assuming constant concentration C_0 at the entrance of the channel with infinite length is:

$$C(x, t) = \frac{C_0}{2} \cdot \left[e^{ax} \operatorname{erfc} \left(\frac{x+aDt}{2\sqrt{Dt}} \right) + \operatorname{erfc} \left(\frac{x-aDt}{2\sqrt{Dt}} \right) \right] \quad (4.5.1.e)$$

where $a = zFE/RT$. It is noteworthy to underline that in the case of no applied external field ($E = 0$), we obtain the equation 4.5.1.c.

Other effects should be taken into account, such as we should consider the loss of the diffusing ions due to absorption or chemical interaction with the constituents of channel. Also, to properly use such model it is important to understand the chemistry of electro-osmosis and ionic migration.

Membrane geometry. In plane & out of plane diffusions

Equations 4.5.1.2 and 4.5.1.4 show analytic solution in the case of channels with infinite length. In general, it is useful to define the *diffusion length* as a measure of

how far the concentration has propagated in the x-direction by diffusion in time t:

$$l_{diff} = 2\sqrt{Dt}.^{88}$$

Since the water trapped in GOM shows a bulk behaviour,⁴⁷ we assume that the diffusivity in GOM is similar to that measured in bulk water.

In figure 49 is depicted the diffusivity measured in bulk water vs the hydrated diameter of the ions involved in our analysis, as reported in literature.⁸⁹ It is noteworthy to underline that the diffusivity increases with the decreasing of the ion diameter.

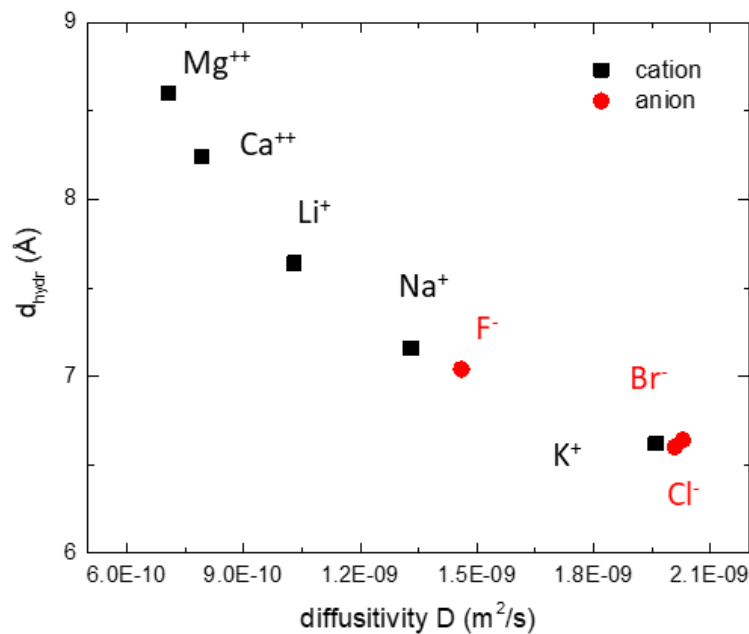


Figure 49. Diffusivity vs hydrated diameter

Using the values reported in figure and a typical diffusion time of 200 min used in the experiments, we obtain a diffusion length of the ions studied in this thesis of about 1 cm.

$$l_{diff} = 2\sqrt{D \cdot t} < 1cm \quad (4.5.1.f)$$

In first approximation, we can describe GOM of a simple layered system where the in plane channel length corresponds to the GOM length. Taking into account the high-defectivity, a similar approach can be performed in the case of out of plane, where the corresponding channel length takes the same order of

magnitude of the GOM thickness.

Hence, taking into account that the typical sizes of the used GOM is 3 cm length and 1 μm thick, it is clear that in plane and out of plane transport correspond to different regimes: in the first case the channel length $L \approx L_{\text{diff}}$ while in the latter $L \ll L_{\text{diff}}$.

In plane regime. The ion concentration along the GOM is described by eq 4.5.1.e, where $x = L$.

Out of plane regime. The gradient concentration is negligible along the vertical direction of GOM. Thus, eq 4.5.1.f assumes a simplified form as the time derivative of the ion concentration is proportional to the applied potential bias:

$$\frac{\partial c}{\partial t} \propto E.$$

The two regimes are fitted by the equations showing a good agreement, as depicted in figure 50.

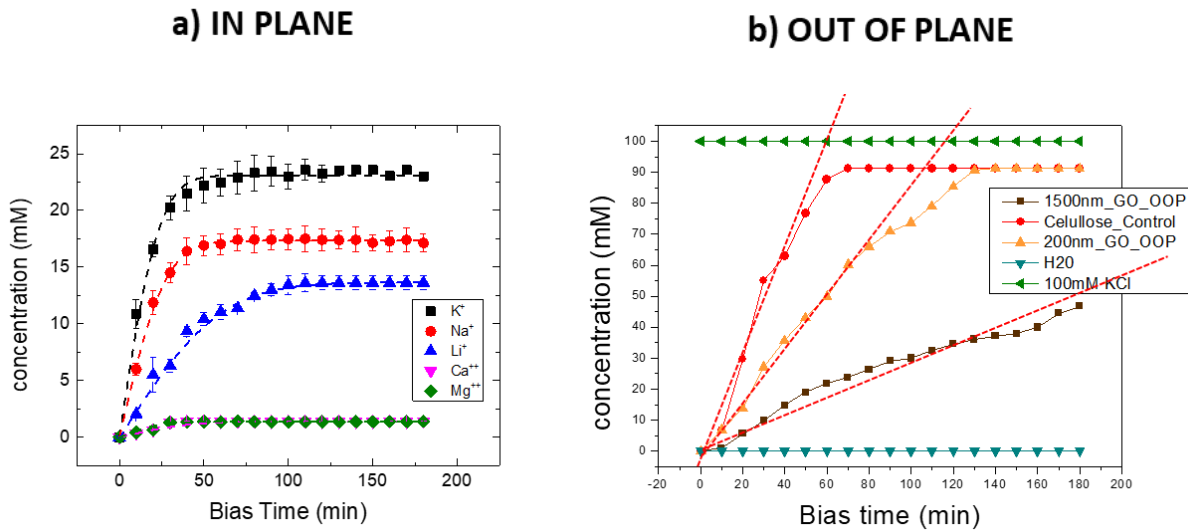


Figure 50. Ion concentration vs bias time: a) in plane and b) out of plane (dashed lines show the linear behaviour for eye guide) Red: cellulose; Orange: 200nm GOM; Brown: 1500nm GOM. 0.1m 1M KCl and H₂O included as a reference. Error bars denote standard deviation.

4.5.2 Out of Plane

Transport out of plane: Concentration (calculated by Transient displacement current) versus time for K^+ , with different concentrations (thickness) of GO. ($c = 0.5 \text{ g/L}$, $1.5 \pm 0.1 \text{ } \mu\text{m}$) and ($c = 0.33 \text{ g/L}$, $0.20 \pm 0.05 \text{ } \mu\text{m}$). Double layer cellulose membrane included as a control. H_2O and 100 mM KCl signals included as a reference. No differences in pH were detected.

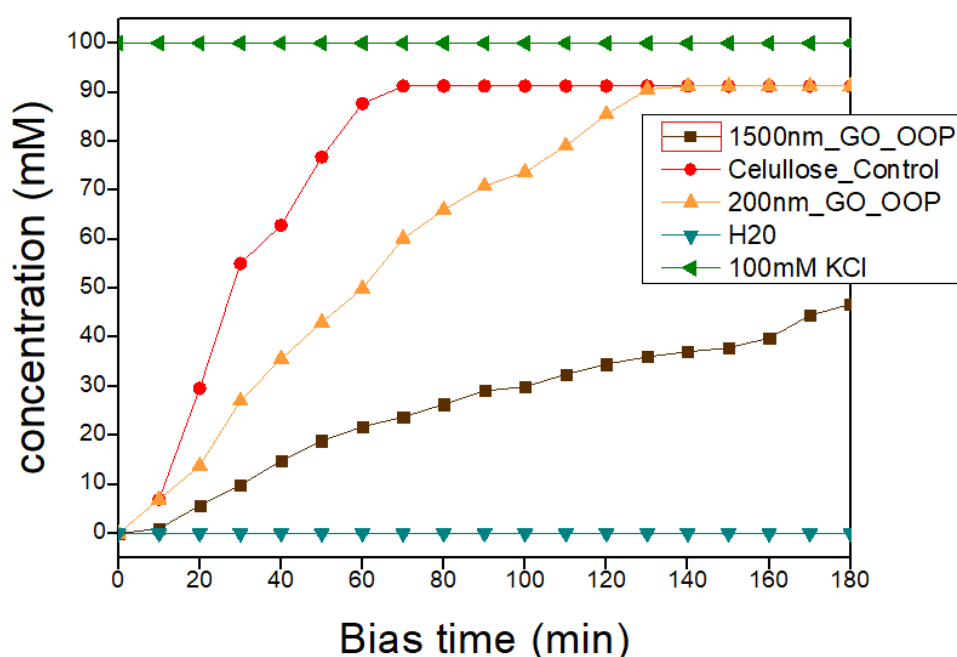


Figure 51. Concentration (calculated by Transient displacement current) versus time for K^+ , with different concentrations (Thickness) of GO. ($c = 0.5 \text{ g/L}$, $1.5 \pm 0.1 \text{ } \mu\text{m}$) and ($c = 0.33 \text{ g/L}$, $0.2 \pm 0.05 \text{ } \mu\text{m}$). Double layer cellulose membrane included as a control. H_2O and 100 mM KCl signals included as a reference.

In Out of plane transport, the maximum concentration will depend on the thickness of the membrane. In thinner membranes the maximum concentrations of ions transported will be reached faster.

4.5.3 In Plane

The ion transport in plane depends on the thickness of the membrane. At a fixed salt concentration, biasing time and voltage, the maximum concentration of the ions at the final vial increase with the thickness of the GOM (figure 52).

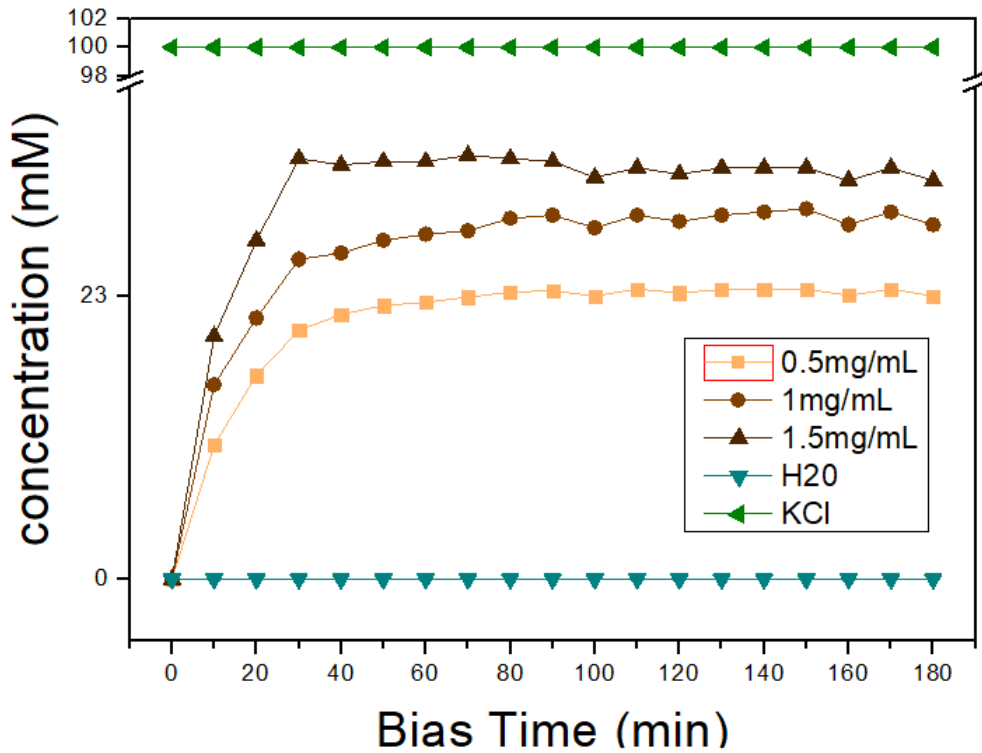


Figure 52. Concentration (calculated by Transient displacement current) versus time for K^+ , with different concentrations (Thickness) of GO a) $c=0.5g/L$; $1.5\pm 0.1\mu$, b) $c=1g/L$; $2.1\pm 0.1\mu$, c) $c=2g/L$; $5.1\pm 0.3\mu$. H_2O and $100mM$ KCl signals included as a reference.

In order to study the behaviour of different ions, GO membranes with fixed thickness ($h = 1.5\pm 0.1 \mu m$) were used. At a fixed thickness the C reaches a plateau because an equilibrium is reached between A and B reservoirs (this will be further explain in figure 60). No differences in pH were detected.

Ion sieving for cations and anions.

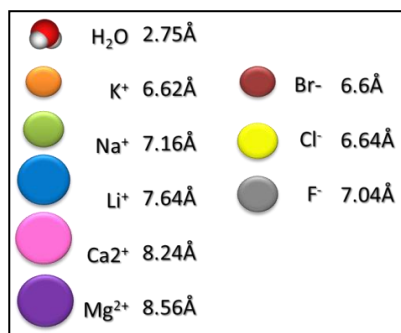


Figure 53. Hydrated diameter of the ions under study.

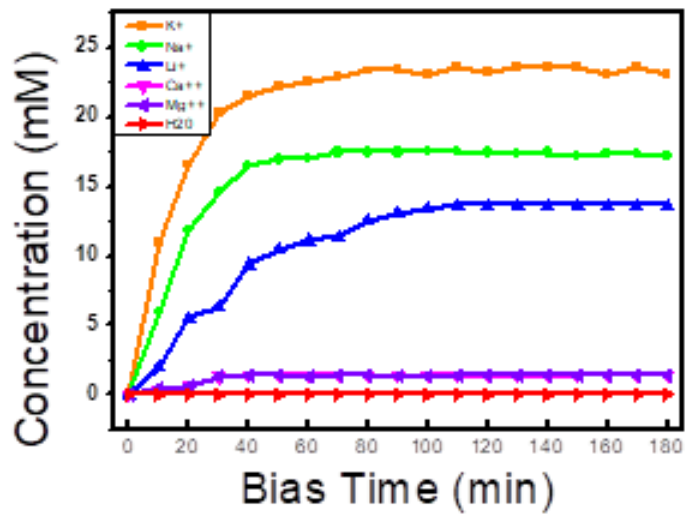


Figure 54. Graph: Concentration versus time for 2 different solutions of Na⁺ K⁺, Na⁺, Li⁺, Ca⁺⁺, Mg⁺⁺. (Cell A, conc = 0.1 M), with same concentration but different days and membranes.

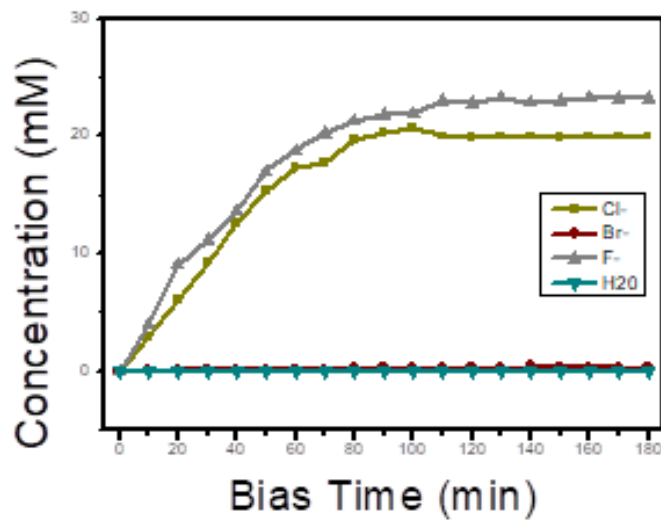


Figure 55. Graph: Concentration versus time for 2 different solutions of F⁻, Cl⁻, Br⁻ (Cell A, conc = 0.1 M), with same concentration but different days and membranes.

In figure 56 is reported the maximum concentration of ions measured in cell B after 180 minutes of negative biasing. In plane nanofluidic ion transport on GO membranes:

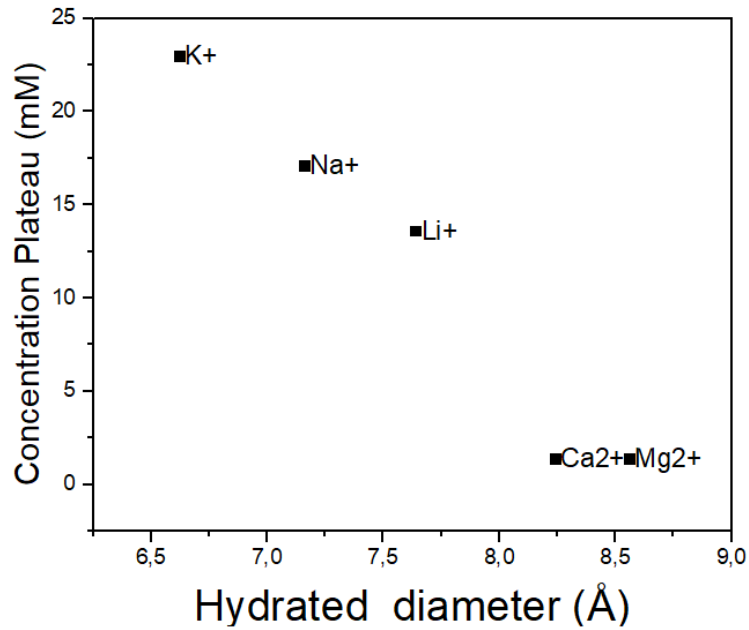


Figure 56. Plateau Concentration vs hydrated diameter

For positive ions: I plateau, meaning the maximum concentration, decrease with the hydrated ratio. Divalent ions can not pass through the membrane. That can be readily rationalized in terms of the chemical interactions between the functional groups of the GO sheets and the divalent metals ions (Figure 57)

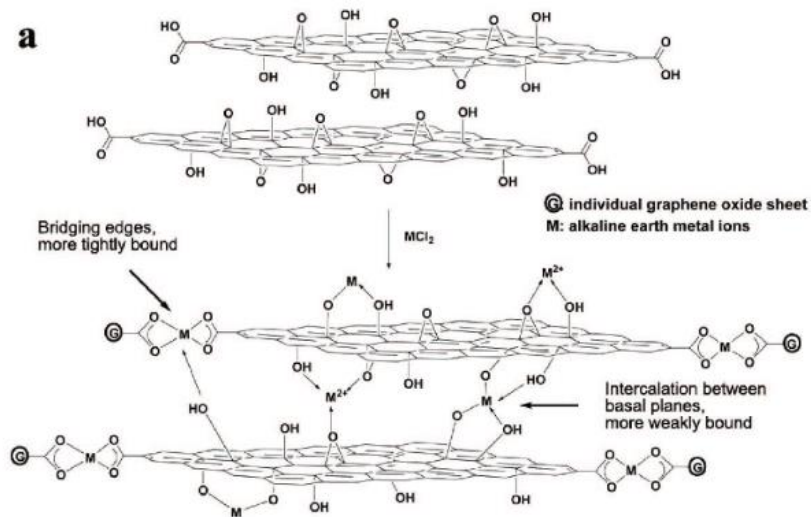


Figure 57. Models of the M-modified GO papers: (a) schematic model of the reaction between GO paper.⁹⁰

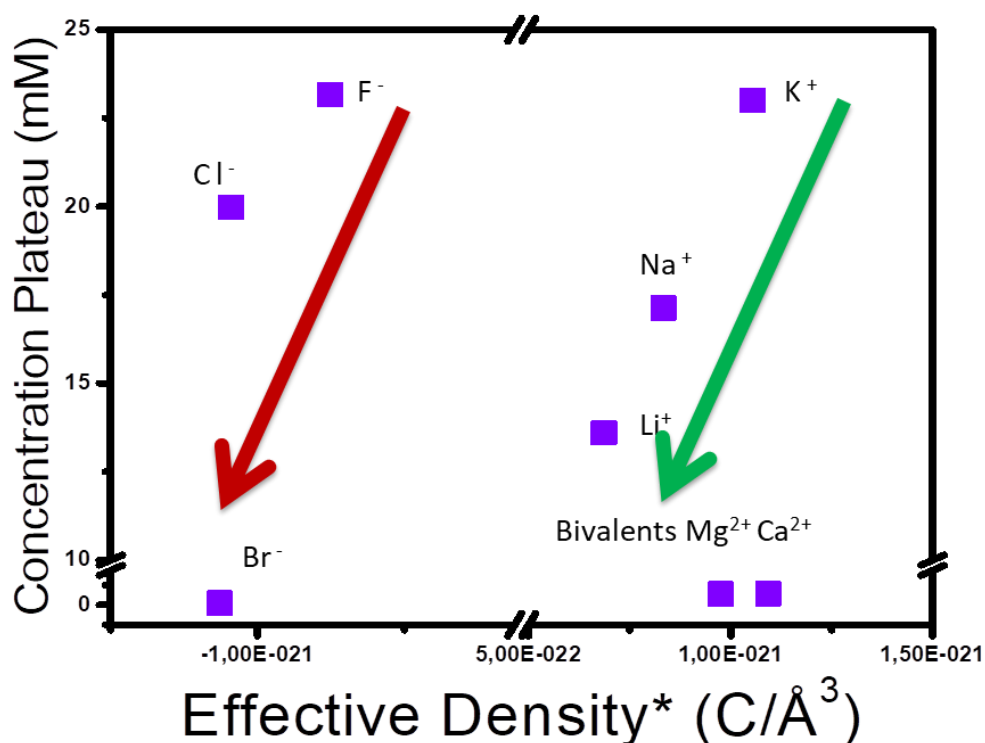


Figure 58. Concentration Plateau (mM) vs recalculated* Effective Density, which is new parameter calculated taking into account the hydrated ion volume.

For negative ions: The order of decreasing electronegativities for negative ions $F > Cl > Br > I$ is another sequence that we will use to interpret the chemical and physical properties of organic compounds. GO membrane surface repels anions owing to its high interaction energy barrier demonstrating remarkable enhancement of ion rejection, a common natural phenomenon “like charges repel while unlike charges attract”. Thus, it is the rule of ion transport that is essential to understand this mechanism.

Table 2. Calculated data for K^+ , Na^+ , and Ca^{2+} .

Ion	Charge density (C mm ⁻³)	R (Å)	R _i (Å)	Mass (uma)	I ₀ (A)	I _{plateau} (A)	τ (s)	α
K ⁺	11	1.33	3.31	39	3.63E-06	1.11E-06	25.1 ± 0.001	0.7408
Na ⁺	24	0.95	3.58	22.99	3.48E-06	3.82E-07	28.33 ± 0.001	0.59255
Ca ²⁺	52	0.99	4.12	40.78	3.46E-06	1.29E-07	222.31 ± 0.001	1.66903

As a particle travels in a solid state device it collides with other particles as well as the atoms in the device. For the drift-diffusion equations individual lattice scattering events or collisions are averaged and all the particles have an average constant drift velocity under the effects of an electric field. The movement of the particles due to the electric field is called the drift current.

Other cases for positive ions with transport behaviour:

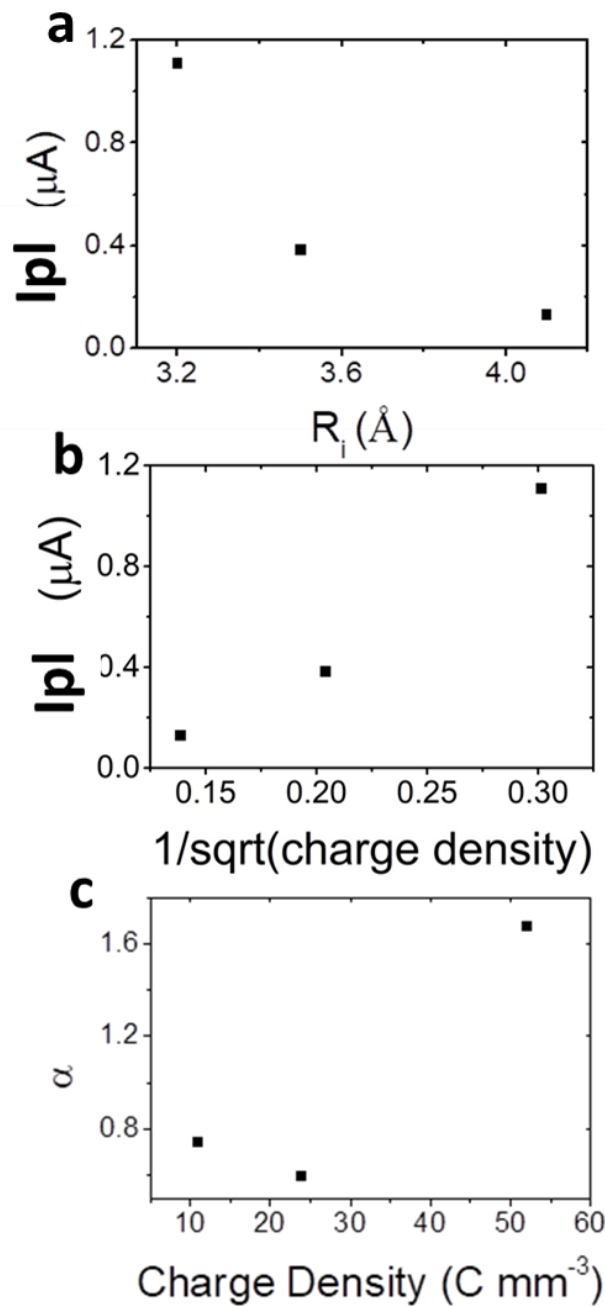


Figure 59. Graph a: I plateau versus hydrated Radio. Graph b: I plateau versus 1/charge density. Graph c: α versus charge density.

I_{plateau} (which means the maximum current) decreases exponentially with ionic radius, and so does I_0 , which may indicate that part of the ions, especially if they are small, redistribute amongst the two dishes even in the absence of biasing; the exponent alpha seems to follow the reciprocal of the charge, or maybe the inverse of the charge density, since it is 0.74 in the case of potassium, then it decreases to 0.6 for sodium, which has the same charge but is bigger, and then it jumps to 1.65 for divalent calcium.

Chemical analysis

We performed a further experiment to better understand the ion transport and why in plane the concentration reaches a plateau. A -0.5V bias is applied in two systems, in which the cell A is 0.1M of K^+ , and cell B DI water, connected by a GOM. The experiment was performed in plane and out of plane (figure 60).

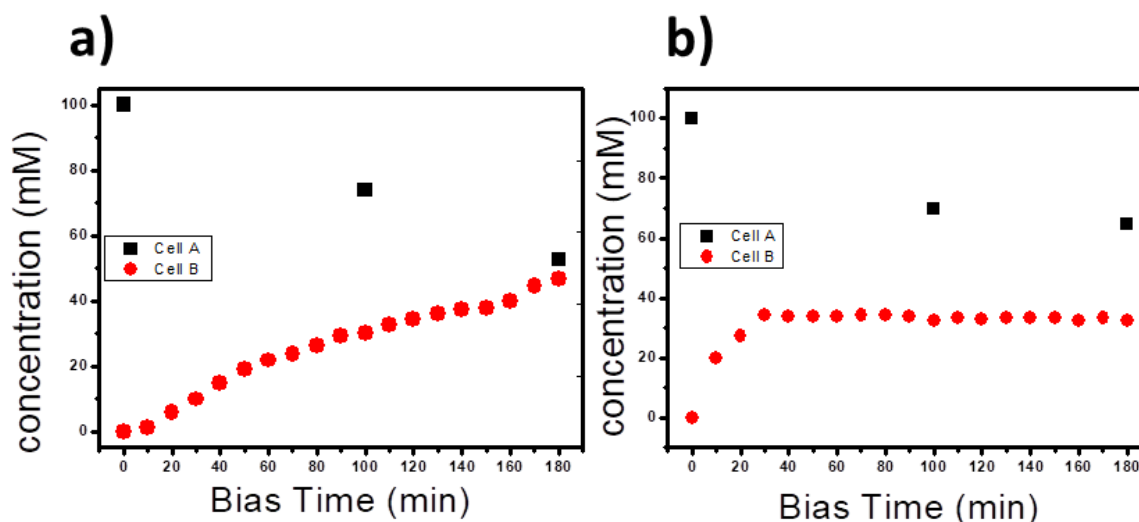


Figure 60. Ion concentration vs time of biasing in cell A feed (black), and cell B (red) in: a) Out of plane b) In plane

While in out of plane we can observe that the bias forces a transport till the systems arrive to an equilibrium, in plane is easy to see that some ions remains inside the membrane, probably due to their length and without applying a flux as

an external force to push (wash out) the ions out of the membrane. That phenomenon is independent of the initial concentration, tests have been made with higher initial concentrations, such as 1M, the only difference is that it takes more time to reach the plateau at the same conditions of thickness and voltage.

To further understand what remains inside the membrane, we proceed to open the membranes and perform some chemical analysis.

The anions studied by XPS are summarised in table XPS, the chemical state of all ions was confirmed by the position of Binding Energy for photoelectron emission and Kinetic energy for Auger emission. Ca, Na, K and Mg are in ionic form, but the anionic counterpart was not clearly identifiable, the positive charge could be compensated by the acid groups present in GO or, as in the case of Potassium by other cations (i.e. OH^-) that form a bulk crystal. No Cl^- , F^- or Br^- was found in the sample after the transit of anions. The pristine GO membrane on PDMS does not contain any ion of those used in present work. Contrary to the anions, the cations (K^+ , Na^+ , Ca^{2+} , Mg^{2+}) are always present with a clear positive counter ion, the potassium, thus no separation between positive and negative ions is present and the most probable mechanism of transport could be the diffusion of positive and negative ions.

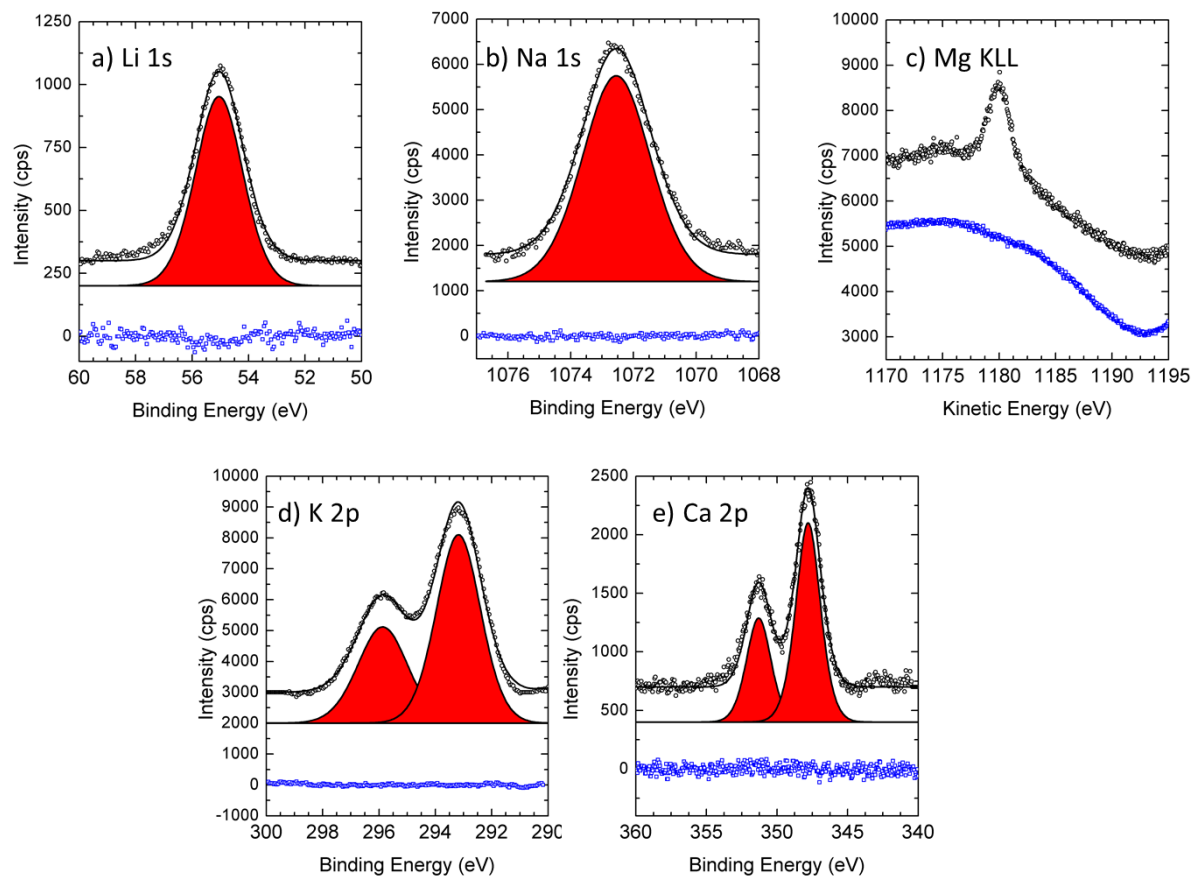


Figure 61. XPS signal of GO membrane after bias (upper black circle) and reference signal from GO membrane on PDMS before bias (lower blue squares) in a) Li^+ , b) Na^+ , c) Mg^{2+} , d) K^+ and e) Ca^{2+} solutions.

Table 3. Identification of cations present on GO membrane in PDMS after bias: characteristic transitions observed and reference values. KE=Kinetic Energy, BE=Binding Energy. *Presence of Ca contamination (0.3% at).

Sample	Transitions	Peak position (eV)	Reference values (eV)	Chemical state	At. % Cation	At. % Anion
GO	C 1s	284.4 (BE)	-	-	-	-
Ca^{++}	Ca 2p _{3/2}	347.8 (BE)	347.5-348 ⁹¹	Ca^{++}	1.2	-
Na^+	N 1s Na KLL	1072.5 (BE) 988.8 (KE)	1071.5-1072.5 ⁹¹	Na^+	2.2	-
K^+	K 2p _{3/2}	293.2 (BE)	292-294 ⁹¹	K^+	6.7	-
Mg^{++}	Mg 2p _{3/2} Mg KLL	51.2 (BE) 947.0 (KE)	51-51.5 ⁹¹	Mg^{++}	1.4 *	-
Li^+	Li 1s C 1s	55.1 (BE) 289.9 (BE)	55.1 289.6	Li_2CO_3	22.9	6.9

Table 4. Identification of anions present on GO membrane in PDMS after bias: characteristic transitions observed and reference values. KE=Kinetic Energy, BE=Binding Energy. * Presence of K contamination (3.7 % at.).

Sample	Transitions	Peak position (eV)	Reference values (eV)	Chemical state	At. % Anion	At. % Cation
F ⁻	F 1s	685.6 (BE)				
	F AP	1340.3 (BE)	1340.2 ⁹²	CaF ₂	12.2 *	16.8
	K 2p _{3/2}	347-348 (BE)				
Cl ⁻	CL 2p _{3/2}	197.4 (BE)	198.5 ⁹¹	KCl	1.1	1.3
	K 2p _{3/2}	292.6 (BE)				
Br ⁻	Br 3d _{5/2}	68.3 (BE)	68.8 ⁹¹	KBr	1.1	0.7
	K 2p _{3/2}	293.2 (BE)	292.2			

XRD analysis

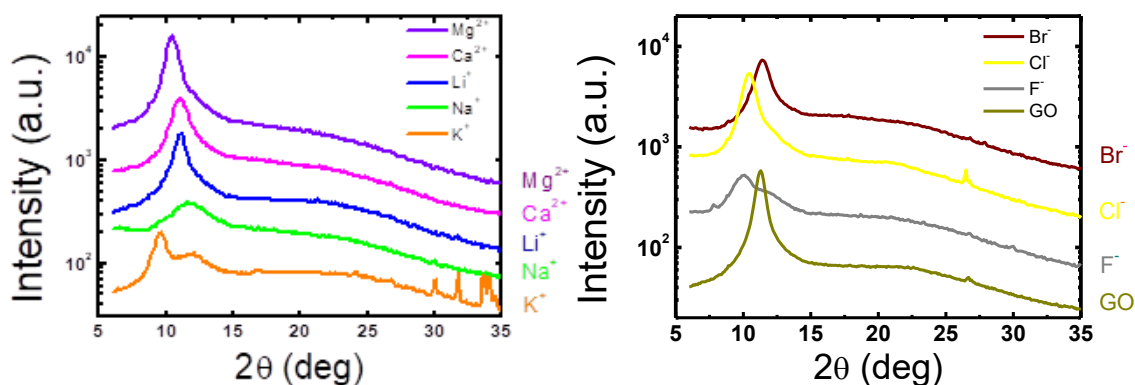
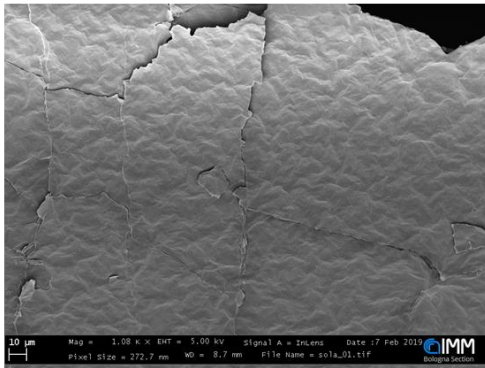


Figure 62. XRD spectra showing the change in the *d*-spacing of GO membranes in different salt solutions: (A) cation (fixed anion = Cl⁻), (B) anion (fixed cation = K⁺).

After 180 minutes of biasing, the membrane was cleaved and the internal surface was analysed by SEM and EDS techniques.

GOM before and after biasing of K^+ (-0.5V):

Before Bias



After Bias

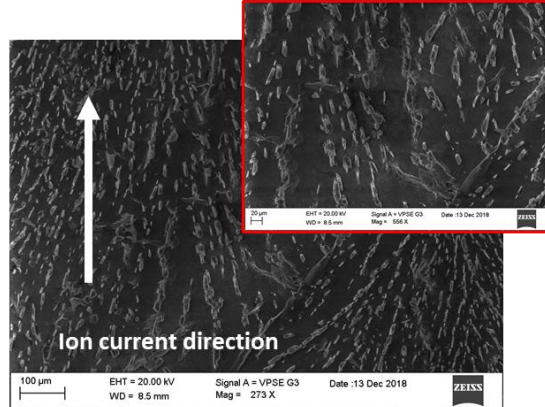
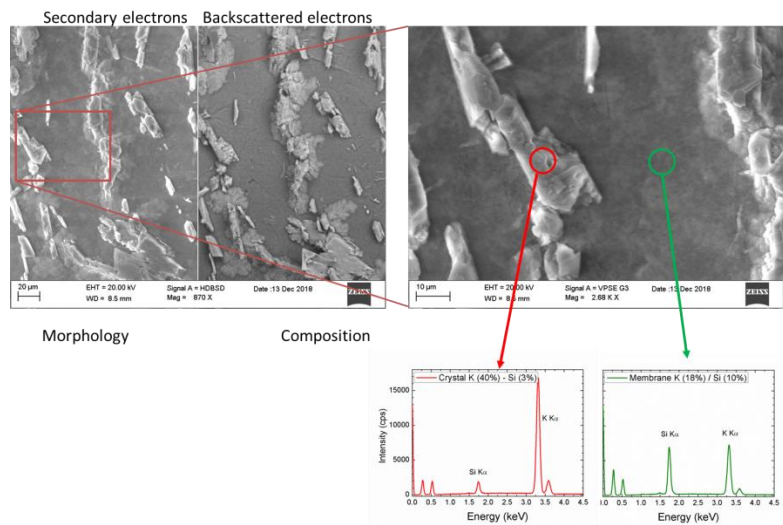


Figure 63. Environmental SEM image of GOM before and after biasing of K^+ . Small crystals oriented along the ion current direction.

After the biasing, K^+ ions remains inside the membrane forming small crystals oriented along the ion current direction.

EDS spectroscopy confirms the composition of crystal.

GO- K^+



Those crystals are salts formed with the OH^- , $-COO^-$, HCO_3^- present inside the membrane as confirmed by EDS analysis.

GO-Ca²⁺

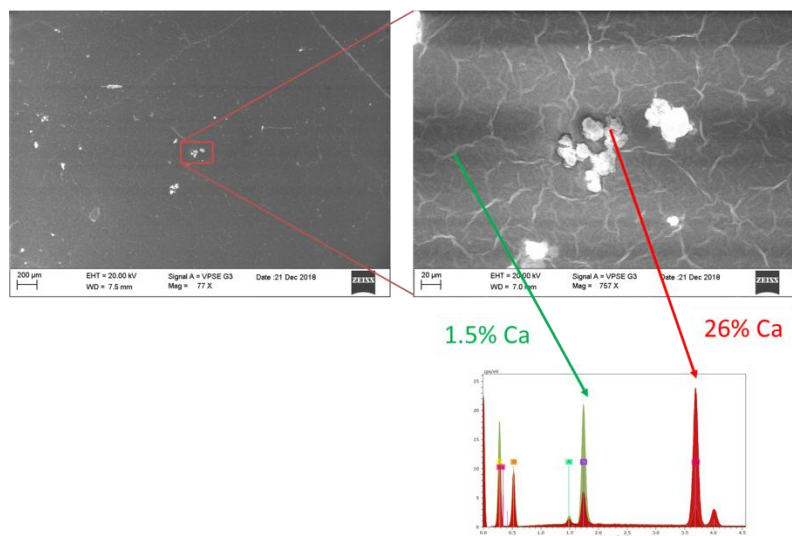


Table 5. Chemical state of the ions inside the GOM after biasing confirmed by XPS and ESD spectroscopy.

Initial Salt	Ion	Chemical state
KCl	K ⁺	KOH, K ₂ CO ₃
NaCl	Na ⁺	NaHCO ₃
LiCl	Li ⁺	Li ₂ CO ₃
CaCl ₂	Ca ²⁺	Ca(OH) ₂ , CaCO ₃
MgCl ₂	Mg ²⁺	Li ₂ CO ₃
KF	F ⁻	CaF ₂ , KF
KCl	Cl ⁻	KCl
KBr	Br ⁻	KBr

Conclusions:

- Fabrication of GO membranes with controlled thickness and spacing, validated via SEM.
- Delivery of ions through GO channels, description of the biasing experiments and results (I plateau decrease exponentially with ionic radius, and so does I₀, which may indicate that part of the ions, especially if they are small, redistribute

amongst the two dishes even in the absence of biasing; the exponent alpha seems to follow the reciprocal of the charge, or maybe the inverse of the charge density, since it is 0.74 in the case of potassium, then it decreases to 0.6 for sodium, which has the same charge but is bigger, and then it jumps to 1.65 for divalent calcium).

The resulting GO-based membranes show remarkable ion selectivity toward the specific ion of interest, for the transport across the membranes as in the biological ion channels.

Comparison in plane vs out of plane with the same thickness membrane.

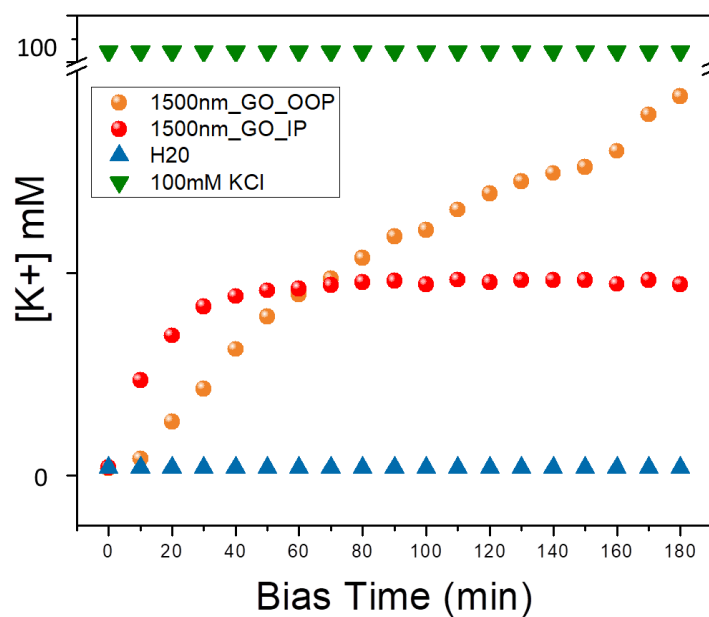


Figure 64. Concentration of K^+ ions versus time for in plane (red) and out of plane (orange) method. Same thickness of GO, $c = 0.5 \text{ g/L}$, $1.5 \pm 0.1 \mu\text{m}$. H_2O and 100mM KCl signals included as a reference.

5 PAH: AZOBENZENE

This chapter introduces small organic molecules (PAH); we study the behaviour of a well-known class of photoswitching molecules (azobenzenes) from cis to trans isomer using light stimuli as an ideal probe to study conformational freedom and in different constrained environments.

PAH: AZOBENZENE

Introduction azobenzenes

Azobenzene can exist in either the cis or trans conformation (Figure 65). The trans-cis isomerization occurs following irradiation with UV-visible light, mechanical stress or electrostatic stimulation.

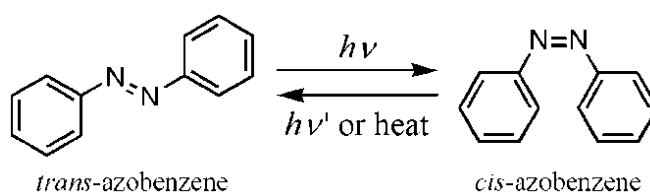


Figure 65. Isomerization of an azobenzene molecule.

The ability to manipulate the quantum yield of photoisomerization and the rate of thermal isomerization is more important than the knowing the isomerization mechanism in practical applications, but both properties depend on the isomerization pathway.¹⁴

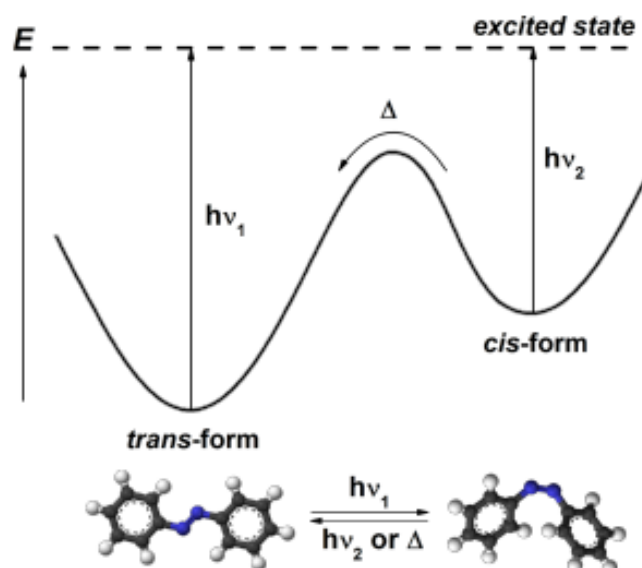


Figure 66. Photochromism of azobenzene derivatives and energetic profile for the switching process.⁹³

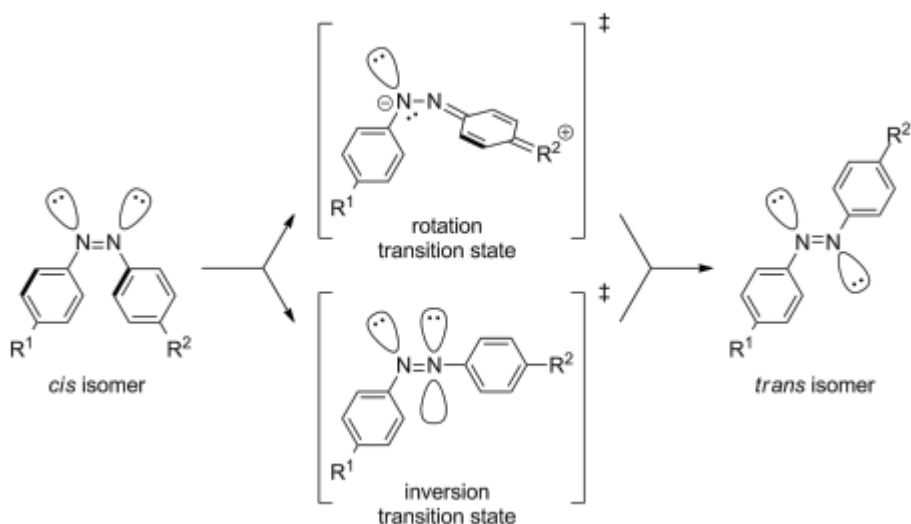


Figure 67. Rotation and inversion mechanisms proposed for the thermal *cis*-to-*trans* isomerisation processes of azobenzenes.

Molecular switches are a class of molecules which are able to reversibly change their chemical structure upon the effect of a certain stimuli such as light irradiation or change of the temperature⁹⁴. They have been extensively studied for a wide range of applications, including solid-state electronics⁹⁵ molecular sensing,⁹⁶ thermal fuel storage,⁹⁷ or nanobiology,⁹⁸ etc; thus attracting more and more interest from the scientific community, what can be seen with the recognition of the Nobel Prize in Chemistry in 2016, awarded to Sauvage, Stoddart and Feringa “for the design and synthesis of molecular machines”.¹³

Molecules with a central axis formed by a double bond are usually hindered rotors in the ground state, but they can also twist upon optical excitation, leading to *cis-trans* isomerization.^{99,100,101} In most cases, such conformational switching process occurs between two different well-defined states and is accompanied by the on/off switch of a certain property, which can be measured by a change in the properties NMR, electronic absorption spectra or luminescence signals.¹⁷

One of the most well-known class of molecular switches are azobenzenes (figure 66). These molecules show photoisomerization from *trans*- to *cis*- conformation around the N=N bond by absorbing UV light, while returning to a *trans* conformation when they are exposed to visible light or heating. This conformational switch can be easily observed in real time by using optical

spectroscopy (figure 67)¹⁰² and it can be ideally exploited in order to obtain a light-driven operation in molecular machines or smart materials.¹⁰³

In particular, dyes featuring the azo linkage (-N=N-) are important for both fundamental studies and technological applications, due to their extensive use as dyes in the textile industry and colorant inks, and more recently due to their new applications in optical switching and optical data storage techniques.^{104,105}

Most of the published works have studied the switching of azobenzenes in solution, where a significant amount of molecules can be switched and studied by optical techniques.¹⁰⁶ In an ideal case molecules are free from steric hindrance, isolated one from each other and dispersed in a uniform medium. Even in such ideal situation, the switching mechanisms may occur by following different reaction pathways, including direct N=N bond torsion, N center inversion or more complex coordinated movements of nitrogen groups and phenyls.^{107,108,109,110} In addition, the switching process in solution is influenced by the solvent polarity and proticity, while the solvent viscosity seems to have a lower impact in the switching dynamics (see ref.¹¹¹ and references therein).

While switching of azobenzenes in organic solvents can be easily studied for bulk solutions, most of the interesting including electronic and industrial purposes are taking place in a more constrained environment, which are challenging to be studied. Azobenzene is able to go upon isomerization even under the effect of strong constraints,^{112,113} such as the tight environments derived from solid matrices or from their inclusion in polymer chains; which has never been observed for other photoswitchable molecules such, as example, stilbenes. This unique feature present in azobenzenes leads to its prominence in the development of new materials with light-switchable properties.¹⁰⁴

As an illustrating example, some applications in electronics require the deposition of the azobenzenes on a 2D substrate, possibly in ordered layers.¹¹⁴ Instead, applications as industrial dyes require the dispersion of the azobenzenes in a 3D material (typically a polymer).

Switching of self-assembled monolayers (SAMs) based on azobenzene molecules has been already studied at macroscopic ensemble level by using spectroscopic techniques^{112,115–117} or at molecular level by means of microscopic or computational techniques.^{116,111} The influence of the environment on the isomerization of azobenzene in constrained confinements is still an important matter of debate in the community, and it requires careful consideration when comparing various methods.¹¹²

There is a huge interest in modify the surface properties and the spacing of the 2D nanochannels that can be conveniently controlled by modifying the starting sheets. One possibility is to add binding sites for further bio-functionalization with organic molecules, such as azobenzenes. In this chapter two different approaches will be studied: Supramolecular and covalent functionalization of graphene oxide with PAH molecules.

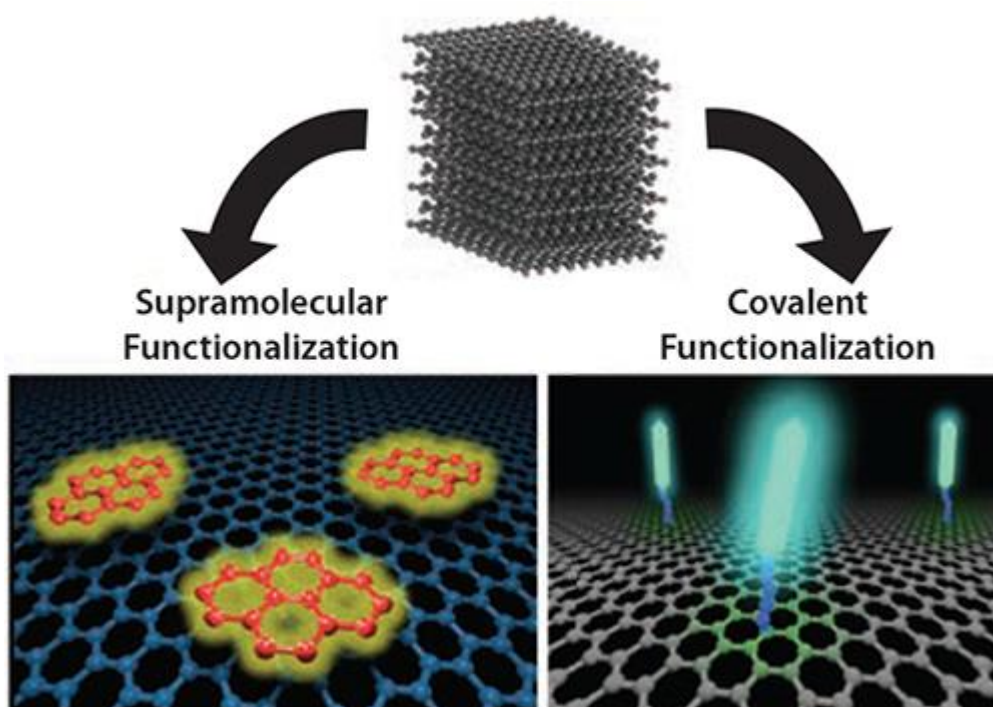


Figure 68. Schematic of different approaches to functionalize graphene by using covalent or non-covalent (supramolecular) approaches.

5.1 Azomolecules for Supramolecular Functionalization

Graphene is a π -system. There are several options for supramolecular functionalization such as π -complexes including the nonpolar gas- π interaction, H- π interaction, π - π interaction, cation- π interaction, and anion- π interaction. The strength of the π -interactions is determined by the combined effect of attractive forces (electrostatic, dispersive, and inductive interactions) and repulsive forces (exchange repulsion). Each of these components shows characteristic differences in physical origin, magnitude, and directionality.¹¹⁸

One approach is the strategy of using triazole molecules is by anchoring an active metal-site into the graphene substrate via the metal-N coordination bonds.

1,2,3-triazoles derived by 'click' chemistry have received rapidly growing interest for their application in new ligand systems for transitions metal complexes.

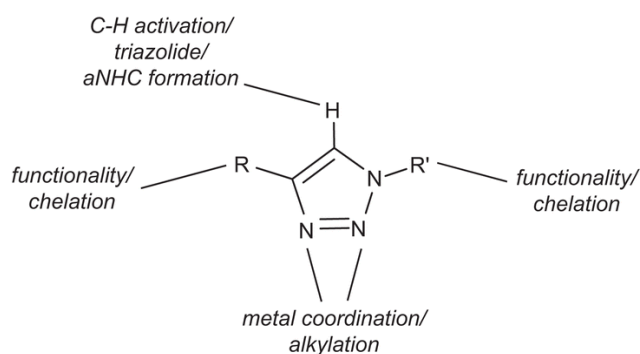


Figure 69. Triazole structure.

For that purpose, a new bunch of triazoles azobenzenes was synthesized.

5.1.1 Synthesis Triazole Azobenzene

Reduction of Disperse Orange 3 (DO3):

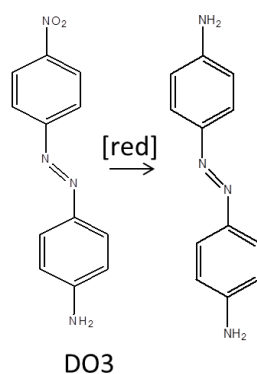


Figure 70. Scheme of the reduction of DO3.

A solution of DO3 (0.2 g, 0.82 mmol, 90% purity) and sodium sulfide nonahydrate (0.35 g, 1.48 mmol, 2 equiv) in ethanol (20 ml) was refluxed for 5h and passed through a column of Geduran Silica 60 (~15 g). The solvent was evaporated under vacuum.

The powder was redissolved in Ethyl acetate. Was extracted a mixture of water (500 ml) and brine (30 ml), extracted with ethyl acetate (3 x 300 ml), dried (MgSO_4), concentrated (~100 ml), as a reddish solid (mp. 244°C, lit. 238-241).

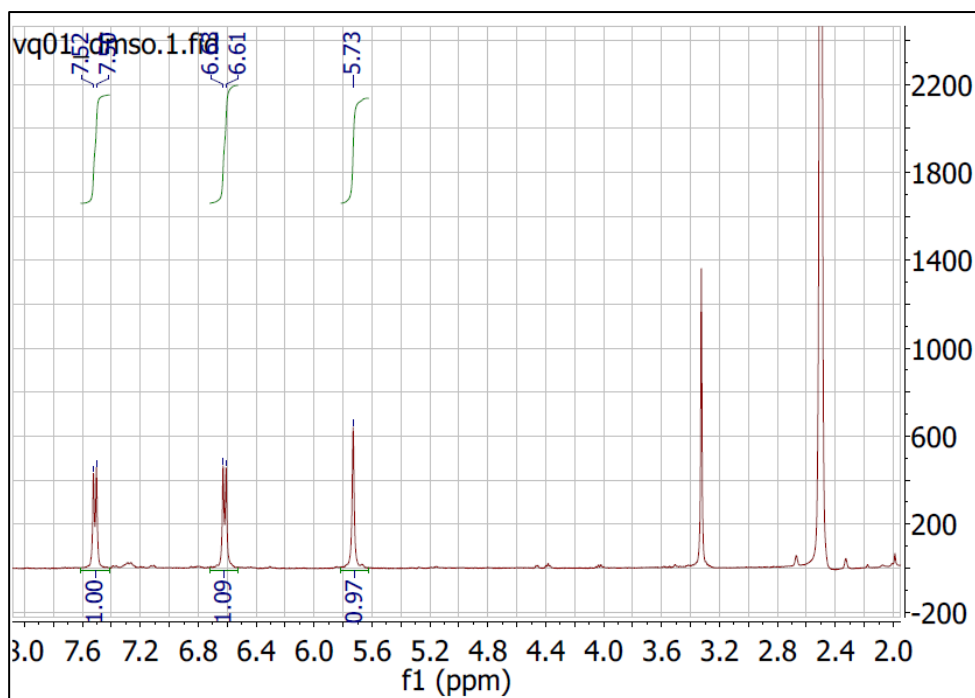


Figure 71. NMR spectra of compound reduced DO3 in DMSO- d_6 (400MHz). Experimental: ^1H NMR (400 MHz, DMSO) δ 7.55 (d, J = 8.8 Hz, 4H), 6.65 (d, J = 8.8 Hz, 4H), 5.73 (s, 4H).



Figure 72. TLC of reduced DO3. $R_f,3$ = 0.55, $R_f,2$ (Disperse Orange 3) = 0.74 (hexanes - ethyl acetate 1:1 v/v)

Experimental Section Chemicals: Thionyl chloride (SOCl_2), hydrazine hydrate ($\text{N}_2\text{H}_4 \cdot \text{H}_2\text{O}$, 65%), diethyl ether, o-xylene, 4-aminobenzoic acid and N, N'-dimethylformamide (DMF). All starting materials were used without further purification.

Synthesis of N,N'-Dimethylformamide Azine Dihydrochloride (DMAZ): Thionyl chloride (SOCl_2 , 14.3 mL, 0.2 mol) was added with stirring to DMF (75 mL) at 5 °C. After addition keep this mixture at 5 °C for 24 h and then added slowly

aqueous hydrazine hydrate (3 mL, 0.065 mol) in 20 ml DMF. After addition the mixture was stirred at room temperature (rt) for 48h and the white precipitate of N, N'-dimethylformamide azine dihydrochloride was collected by filtration and washed with DMF and diethyl ether: 12,16 g (87,4%).

Mw DMAZ: 214.08g/mol. React Lim: Hydrazine: 0,065mol; max 13, 91, product: 12,16g, RT: 87, 4%)

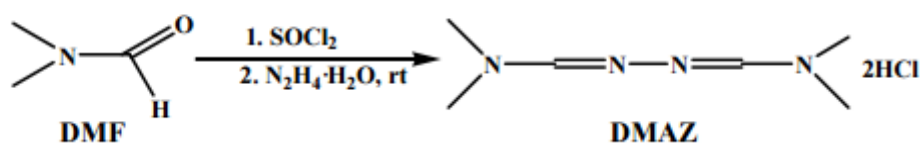


Figure 73. Scheme of Synthesis of DMAZ and 4-(4H-1,2,4-Triazol-4-yl)benzoic Acid (Hept).
NMR DMAZ

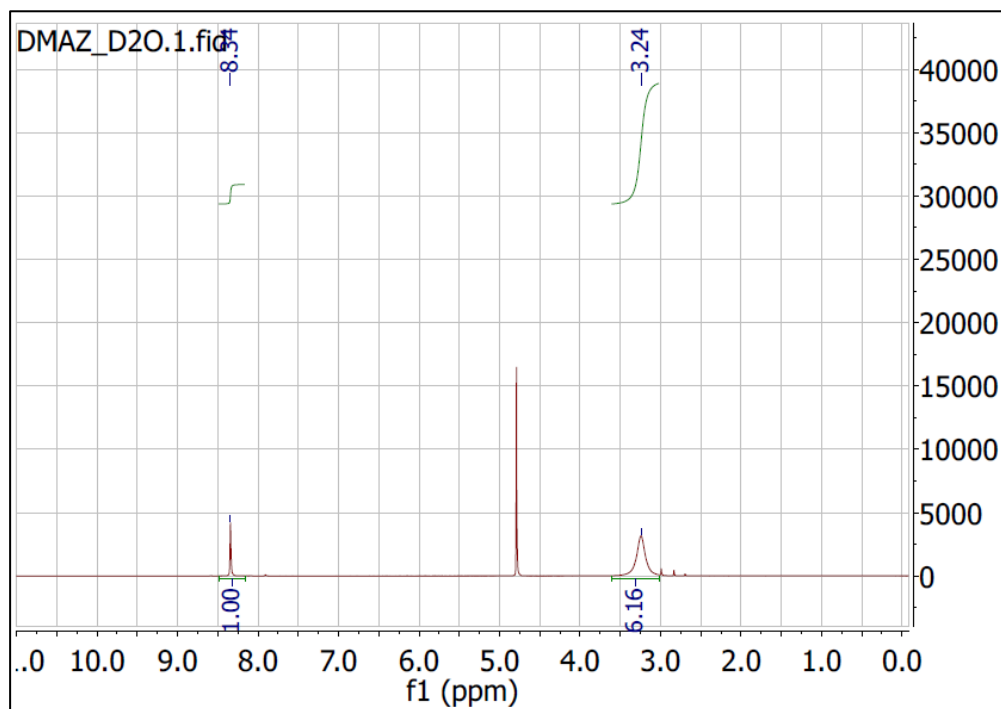


Figure 74. NMR spectra of DMAZ in DMSO-d₆ (400MHz). Experimental: ¹H NMR (400 MHz, DMSO) δ 3,24 (s, 6H), 8,34 (s,1H).

This reaction was performed according to reported procedures.¹¹⁹

Synthesis of VQ10 (Triazole):

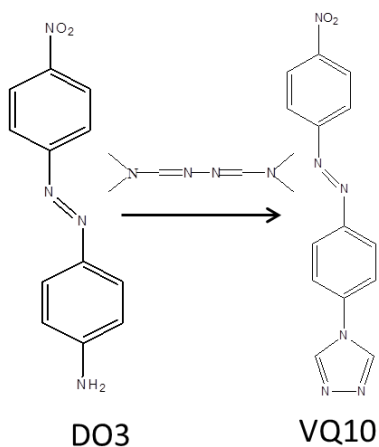


Figure 75. Scheme of the synthesis of the compound VQ10 from DO3 and DMAZ.

Refluxing a mixture of N, N'-dimethylformamide azine dihydrochloride, DMAZ (0.88 g, 4.12 mmol) and Disperse orange, DO3 (1 g, 4.12 mmol) in 25 ml xylene (reaction should be conducted in a fume hood) for 24 h gave a brown solid, which was filtered and washed with EtOH (1×10 mL) and Et₂O (1×8 mL).



Figure 76. TLC of reduced VQ10. $R_f, 3 = 0.55$, $R_f, 2$ (Disperse Orange 3) = 0.74 (hexanes - ethyl acetate 1:1 v/v)

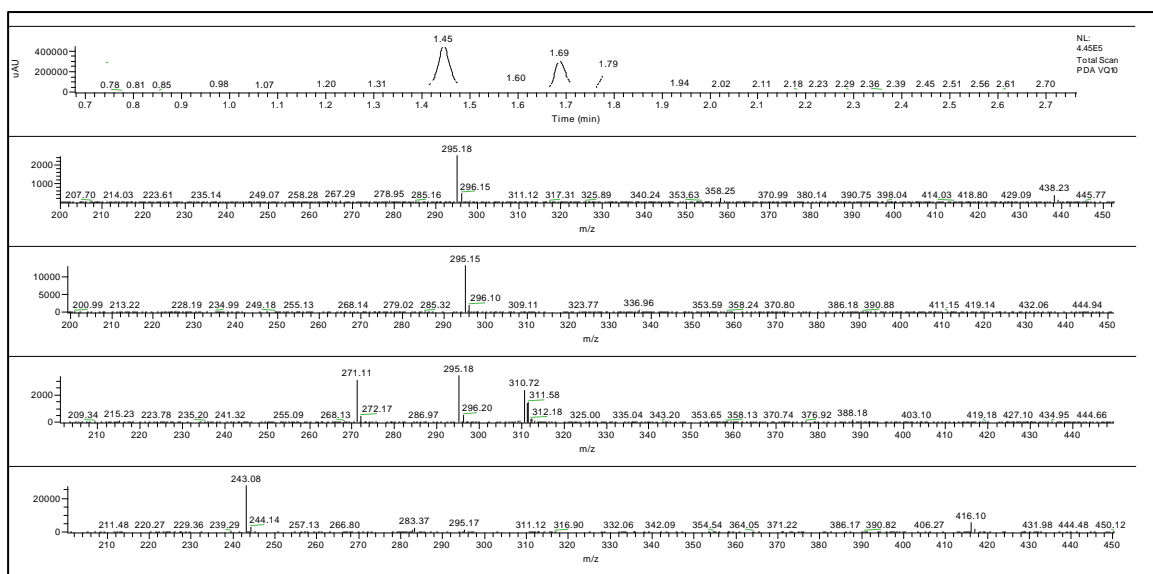


Figure 77. HPLS-MS spectra of the compound VQ10.

Synthesis of VQ11 (reduction of VQ10):

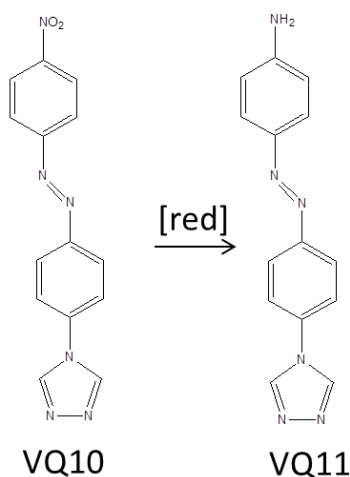


Figure 78. Scheme of the reduction of VQ10.

A solution of VQ10 (0.6 g, 2mmol) and sodium sulfide nonahydrate (0.98 g, 4 mmol, 2 equiv) in ethanol (20 ml) was refluxed for 5h. The solvent was evaporated under vacuum.

The solvent was evaporated under vacuum and resulting brown oil was redissolved in a mixture of water (500 ml) and brine (30 ml), extracted with ethyl acetate (3 x 300 ml), dried (MgSO₄), concentrated.

TLC: Hexane/Ethyl acetate. Column: 1. Hexane 2/Ethyl acetate 2. Ethyl acetate 3.

Ethyl acetate-15%MeOH. This reaction was performed according to reported procedures.¹²⁰

Synthesis of amide:

1.3 eq of base *N,N*-Diisopropylethylamine (75 μ l, 0.4 mmol, 1.3 equiv) was added to a solution of VQ11 (85mg, 0.32 mmol, 1 equiv) dissolved in CHCl₃ (20ml) 0°C. Then the Octanoyl chloride (55 μ l, 0.32 mmol, 1 equiv) was added drop by drop and leave it overnight till room temperature.

The solvent was evaporated under vacuum, then redissolved in basic water (Sodium hydrogen sulfate), extracted with CHCl₃, dried (MgSO₄), and concentrated. Precipitation with ether. TLC: Ethyl acetate-5%MeOH

5.1.2 Switching Study in Solution

Here the study of the switching in solutions is reported. UV-Vis spectra of triazole synthesized molecules.

UV $\lambda=365\text{nm}$ ($P_d=3.2\text{ Mw cm}^{-2}$) Vis $\lambda=440\text{nm}$ ($P_d=0.56\text{ Mw cm}^{-2}$)

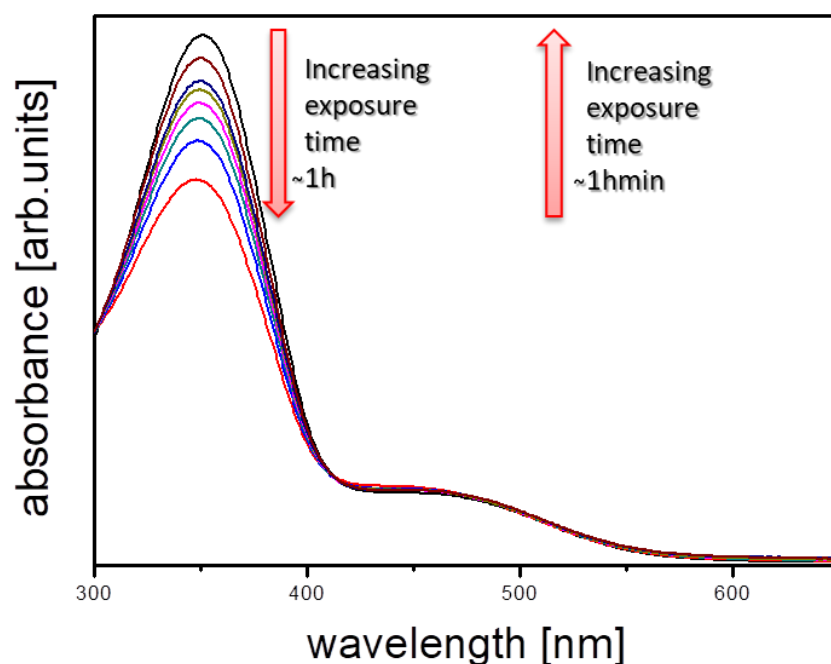


Figure 79. Changes in the absorption spectra of the triazole azobenzene in DMF upon irradiation at 365 nm.

Although the efficiency with supramolecular functionalization is good enough, it is difficult to monitor the rate of non-covalent functionalization.

5.2 AZOMOLECULES FOR COVALENT FUNCTIONALIZATION:

In most cases when organic molecules are covalently attached on the graphene surface, its extended aromatic character is perturbed, enabling the control of its electronic properties. The development of a band gap through chemical doping is a powerful method for the use of graphene in nanoelectronic devices.¹²¹

By using this strategy the interlayer space between GO sheets can be controlled by the size of PAH molecules.

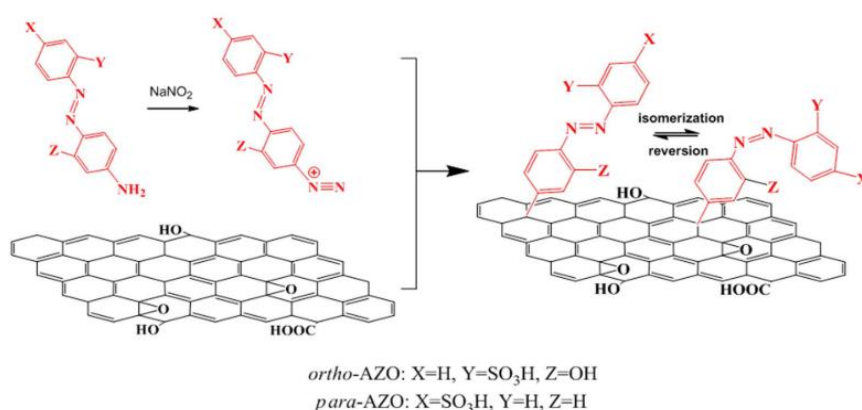


Figure 80. Example of covalent functionalization of graphene by azobenzene with molecular hydrogen bonds.

5.1.2 Photoswitching Study in Different Environments (AZO1, AZO2)

From commercial azobenzenes:



Figure 81. Scheme of functionalization of GO sheets with commercial azobenzenes (AZO1).

We used complementary techniques to study commercial azobenzene molecules

(Acid yellow 9 and Disperse orange 3) in different environments for covalent functionalization purpose: polar and apolar solvents, liquid polymers, 2D self-assembled monolayers and 3D crystals. In each case, we determined if and how fast the molecule can undergo *cis*→*trans* and *trans*→*cis* conformational switching. The techniques used to study the different systems were optical absorption spectroscopy, femtosecond transient absorbance spectroscopy, Kelvin probe force microscopy, reflectance spectroscopy, and density-functional calculations. In this way, we could monitor the conformational switching from femtosecond scale, in water, to milliseconds scale, in aprotic solvents, while switching in more hindered, 2-dimensional self-assembled monolayers or 3-dimensional crystals was not observed at all. Switching in solid, at monolayer level, was observed instead in nanoscale islands of an analogue azobenzene molecule where no polar charged groups were present.

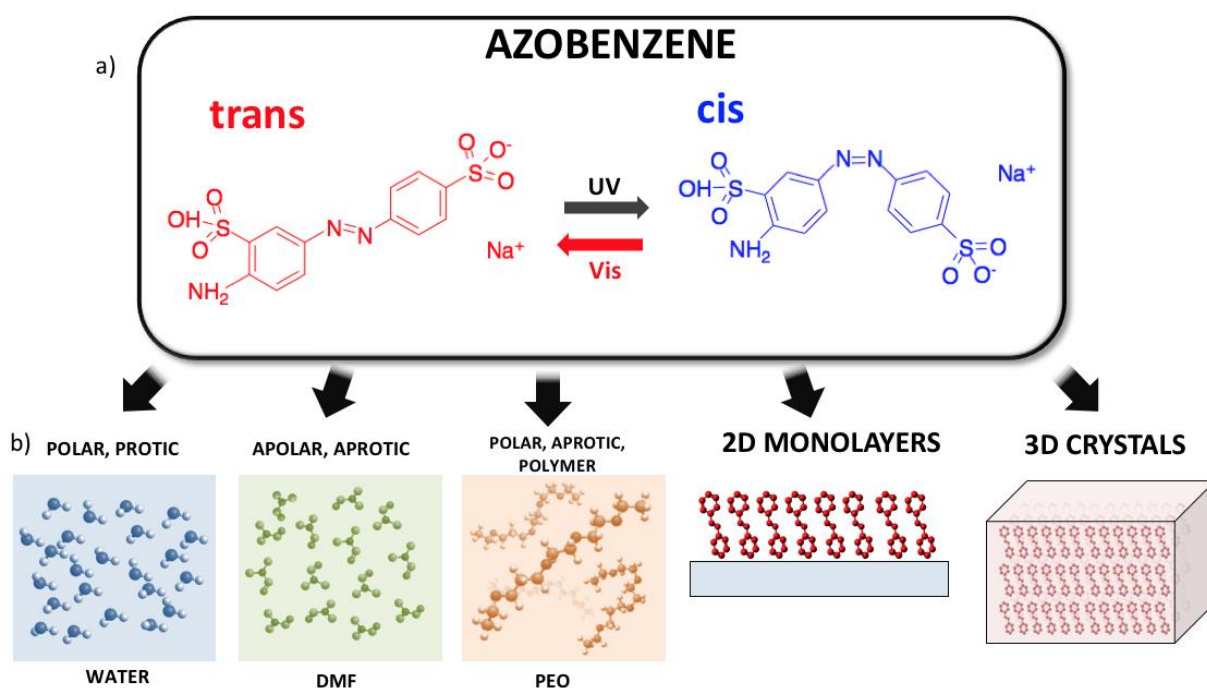


Figure 82. a) Structure and different conformations AZO1, one of the azobenzene molecules studied in this work. b) Schematic representation of all the different solid and liquid environments where the *cis* → *trans* switching of the molecule was studied.

Most of the published works have studied the switching of azobenzenes in

solution, where a significant amount of molecules can be switched and studied by optical techniques.¹⁰⁶ In an ideal case molecules are free from steric hindrance, isolated one from each other and dispersed in a uniform medium. Even in such ideal situation, the switching mechanisms may occur by following different reaction pathways, including direct N=N bond torsion, N center inversion or more complex coordinated movements of nitrogen groups and phenyls.^{107,108,109,110} In addition, the switching process in solution is influenced by the solvent polarity and proticity, while the solvent viscosity seems to have a lower impact in the switching dynamics (see ref.¹¹¹ and references therein).

While switching of azobenzenes in organic solvents can be easily studied for bulk solutions, most of the interesting including electronic and industrial purposes are taking place in a more constrained environment, which are challenging to be studied. Azobenzene is able to go upon isomerization even under the effect of strong constraints,^{112,113} such as the tight environments derived from solid matrices or from their inclusion in polymer chains; which has never been observed for other photoswitchable molecules such, as example, stilbenes. This unique feature present in azobenzenes leads to its prominence in the development of new materials with light-switchable properties.¹⁰⁴

As an illustrating example, some applications in electronics require the deposition of the azobenzenes on a 2D substrate, possibly in ordered layers.¹¹⁴ Instead, applications as industrial dyes require the dispersion of the azobenzenes in a 3D material (typically a polymer).

Switching of self-assembled monolayers (SAMs) based on azobenzene molecules has been already studied at macroscopic ensemble level by using spectroscopic techniques^{112,115-117} or at molecular level by means of microscopic or computational techniques.^{116,111} The influence of the environment on the isomerization of azobenzene in constrained confinements is still an important matter of debate in the community, and it requires careful consideration when comparing various methods.¹¹²

Here, we present a complete study on the properties of aminoazobenzene and pseudostilbene compounds focusing on how the cis-trans switching behaviour is influenced by the environment, in particular when the molecule is solubilized in different solvents, dispersed in polymers, deposited in 2D layers on a substrate or arranged in 3D crystals (figure 82b). For this purpose, we had to overcome different limitations due to the solubility of the molecule, its processability and the complementary limitations of the different techniques used in this work. By combining spectroscopic studies in solution and on a surface with microscopic techniques, we observed the cis-trans switching of such azobenzene molecules both in bulk ensembles and in nanoscopic structures.

Experimental details

We choose two commercial azo compounds as target molecules: 2-Amino-5-([4-sulfophenyl] azo) benzenesulfonic acid, Acid yellow 9 (CAS: 74543-21-8), named AZO1 and 4-(4-Nitrophenylazo) aniline (CAS: 730-40-5), named AZO2.

AZO1 is an aminoazobenzene class molecule and is commercialized as a biological stain, and formerly used as a food dye (E105).¹²² One of the two azobenzene rings is decorated with one sulfonic acid (Donor) and one amine (Acceptor) group, in meta- and para- positions respectively; while the other ring is substituted with a sulfonic acid sodium salt in a para- position.

The presence of two sulphonic groups gives to AZO1 a good solubility in a wide range of solvents.

We studied the switching behaviour of AZO1 molecules in a highly polar, protic solvent (water) and in a less polar, aprotic solvent (dimethylformamide, DMF).

Previous works have suggested that solvent viscosity could have minimal influence on the switching rate of azobenzenes.^{111,123} Thus, besides small molecular solvents, we tested the switching behaviour of AZO1 also in a polymeric matrix environment, i.e. in Polyethylene glycol (PEG). Such liquid polymer, widely used in academy and industry, also provides a polar, aprotic

environment for solvated molecules. PEG has significant polarity and a viscosity ≈ 90 mPa·s, significantly higher than the one of water (0.89 mPa·s) and DMF (0.8 mPa·s).

AZO2 is a pseudostilbene-type molecule, a dye used in colouring natural and synthetic fabrics. It can be found in many clothing materials such as acetates, nylon, silk, wool, and cotton. AZO2 bears no charged group, but only an electron-donor NH_2 group on one phenyl ring, and an electron withdrawing NO_2 group on the other, giving a significant dipole moment and fast cis-trans switching kinetics (see below for more details). This molecule is less processable than AZO1 but shows anyhow a good solubility in DMF, and was processed using this solvent.

In a first stage, DFT calculations gave us access to the relative stability and the opto-electronic properties of the individual cis and trans conformers of AZO1 for each studied solvent.

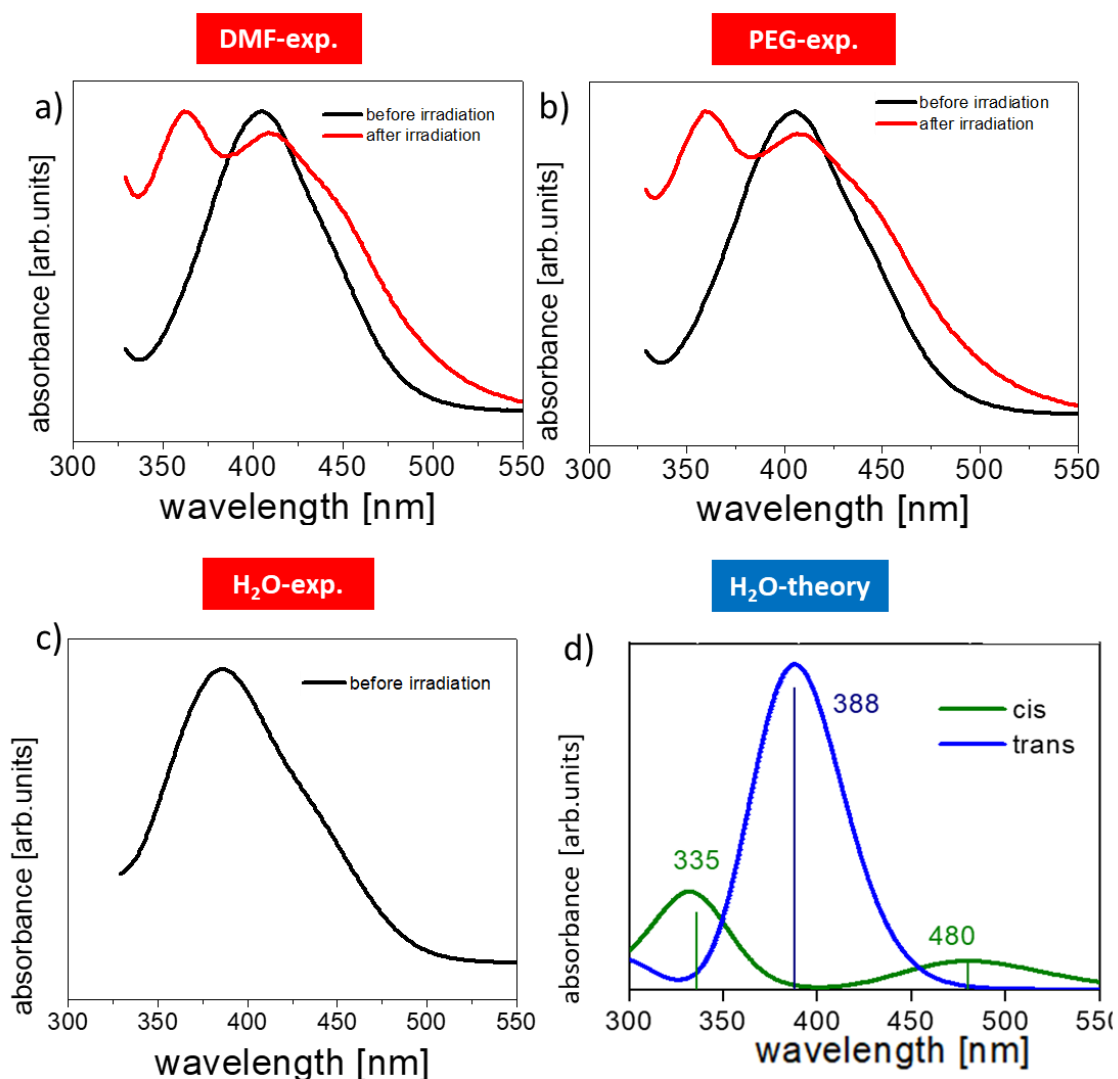


Figure 83. . a,b,c) Optical absorption spectra of AZO1 in different solvents. d) Calculated spectrum for AZO1 in its *trans*- (blue) and *cis*- (green) forms in water before and after UV illumination.

As it is expected for standard azobenzenes, the *trans*- form is energetically most stable respect the *cis*- form in the majority of cases. However, the photoisomerization to the *cis*- form takes place upon UV light irradiation. On the other hand, *cis* → *trans* thermal isomerization occurs spontaneously in the dark owing to the thermodynamic stability of the *trans* isomer. In addition to thermal isomerization, photoinduced *cis* → *trans* isomerization is also possible upon VIS light irradiation.¹²⁴

Theoretical calculations showed the different features in the absorption spectra for the *cis* and *trans* forms, while only a minor effect of the solvent environment

was observed at this level of theory. In all the studied cases, the absorption spectra of the trans- form is dominated by an absorption peak centred between 300 and 400 nm due to the π - π^* transition, while the cis- form presents a dominant peak at 450–500 nm originated from the n- π^* transition. The absorption spectra were acquired for each solution (figure 82a-c) in dark (black curves) and after illumination with UV light, $\lambda = 365$ nm (red curves). In the pristine state (i.e. dark), all azobenzene molecules were in the trans-configuration. In general, the calculations well reproduce the difference in absorption spectra of cis and trans form, but showed only a small effect due to the solvent environment. In all cases after illumination, a wide absorption peak was predicted between 300 and 400 nm assigned to the π - π^* transition, and another at 450–500 nm assigned to the n- π^* transition. The optical absorption of trans-form, as measured in dark, is not significantly dependent on the solvent used, in agreement with DFT calculations. The spectra measured on DMF was indistinguishable to those measured on PEG, both showing the main peak at ca 410 nm and a second one, which is not resolved at ca 445 nm. Similar behaviour was observed in the case of water, where the main peak is shifted at ca 390 nm, while the second one is located to 445 nm. These differences are attributed to the small effect of solvent on the HOMO-LUMO energies, which is directly affecting the photonic band gap.

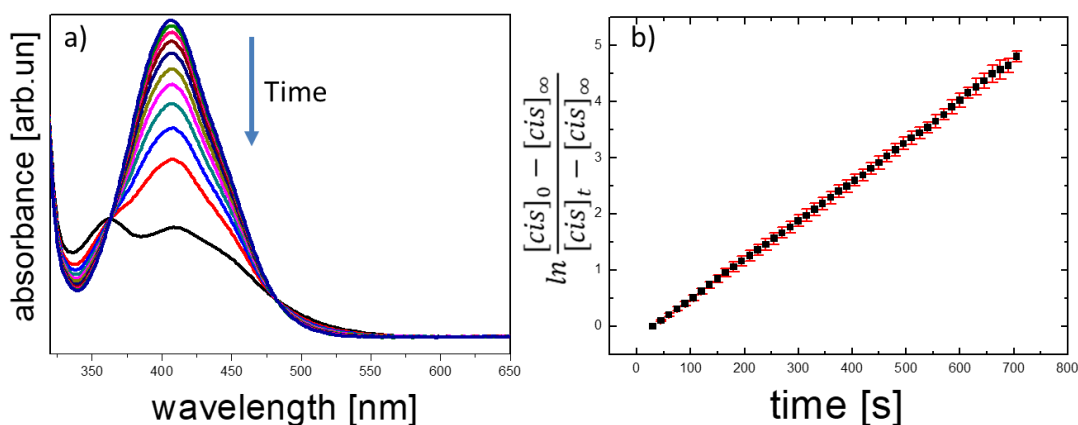


Figure 84. a) Changes in the absorption spectra of AZO1 in DMF upon irradiation at 365 nm. The Arrow indicates the changes upon irradiation time). The different spectra have been recorded each 30 seconds. b) Absorbance at 410 nm

(black squares) as a function of irradiation time. The red solid line shows a fit of the experimental data acquired during 5 cycles of irradiation under the same conditions.

Table 6. Kinetic constants calculated for AZO1 switching in different solvents.

	k ($10^{-3}/s$)					
	DMF	PEG	PEG:H ₂ O (75%:25%)	PEG:H ₂ O (50%:50%)	PEG:H ₂ O (25%:75%)	H ₂ O
trans → cis	2.3±0.2	2.5±0.1	2.4±0.1	–	–	–
cis → trans	7.3±0.1	2.9±0.2	2.2±0.2	–	–	–

Afterwards, the trans→ cis isomerization was induced by light illumination at $\lambda=365\text{nm}$ ($P_d=3.2\text{ mW/cm}^2$) until no further spectral variation was observed, thus reaching the photostationary state (figure 84) given by a racemic solution of both cis- and trans- isomers. Thereafter, we examined the backward (cis → trans) isomerization by turning off the 365 nm light source.

The switching kinetics depended strongly on the polarity and proticity of the solvent used. In the case of DMF and PEG solvents, the formation of cis-AZO1 was clearly observed by the growth of a further peak at ca 360 nm and the decrease of the relative intensity of the peak at 410 nm, thus indicating the presence of a racemic mixture of cis- and trans- isomers. However, no variations in the absorption spectrum were observed for AZO1 compound in water, where the optical absorption was stable upon prolonged illumination.

We used time-dependent measurements to estimate the kinetics of cis-trans and trans-cis switching in the cases where the photoisomerization was observed, i.e. in DMF and PEG. Figure 84 shows a series of spectra obtained as a function of irradiation time for AZO1 in DMF solvent upon illumination at 365 nm. The kinetic rate k of the isomerization followed first-order kinetics (figure 84b), and it was estimated following the same procedure as in previous azobenzene studies¹²⁵ by using the formula:

$$\ln \frac{[cis]_0 - [cis]_\infty}{[cis]_t - [cis]_\infty} = k_{cis} t \quad (51.2.a)$$

Where $[cis]_0$ and $[cis]_t$ denote the concentrations of the cis- isomer at time 0 and t, respectively; while k_{cis} is the rate constant. $[cis]$ was estimated by measuring the absorption intensity at 410 nm. A similar equation was used to measure the kinetics of the trans \rightarrow cis isomerization. The calculated k-values for each solvent are reported in Table 1, while no switching process was observed in water.

The stabilization of the azobenzenes with the polarity of the solvent is not affecting the frontier orbital (HOMO/LUMO) energies which lie in a small range of values (± 15 meV, as estimated by DFT) for the three studied solvents. In particular water is the solvent displaying the largest polarity, thus being more stable than PEG and DMF. However, this difference in the stability has a minor influence in the relative energy between trans- and cis- forms, which is about 0.62-0.64 eV in all cases. At this point, it is important to highlight that the theoretical description of the solvent within our models is based on an explicit continuum model which is mainly dependent on the dielectric constant of the medium, while no implicit effects of the solvents are studied at this stage.

We also performed kinetics measurements in mixtures with different fractions of PEG and water (% v/v see figure 83 and table 6). Mixtures with 75% of PEG still showed a measurable switching, even if it was much smaller than in the case of PEG. Mixtures with 50% or 25% PEG did not show any switching behaviour.

The dielectric constant of such mixtures has been studied previously,¹²⁶ and is not linearly dependent on the % of PEG; following instead a modified Bruggeman model due to the significant interaction between poly ethylene glycols and water in the mixtures.

According to these results, the dielectric constant of 75% and 50% PEG in water is 16 and 19 respectively, is much closer to the dielectric constant of PEG (14.1) respect the one of water (80.1). As a result, the different switching behaviour observed between 100% and 75% PEG:H₂O solutions (showed a switching process) vs. 50%, 25% and 0% (no switching was observed) cannot be ascribed to

the macroscopic dielectric properties of the solvent. One could think that this effect may be originated by the implicit action (i.e. geometrical constraint) of the solvent in the isomerization process for AZO1, which should be larger in the case of water solvent in that case.

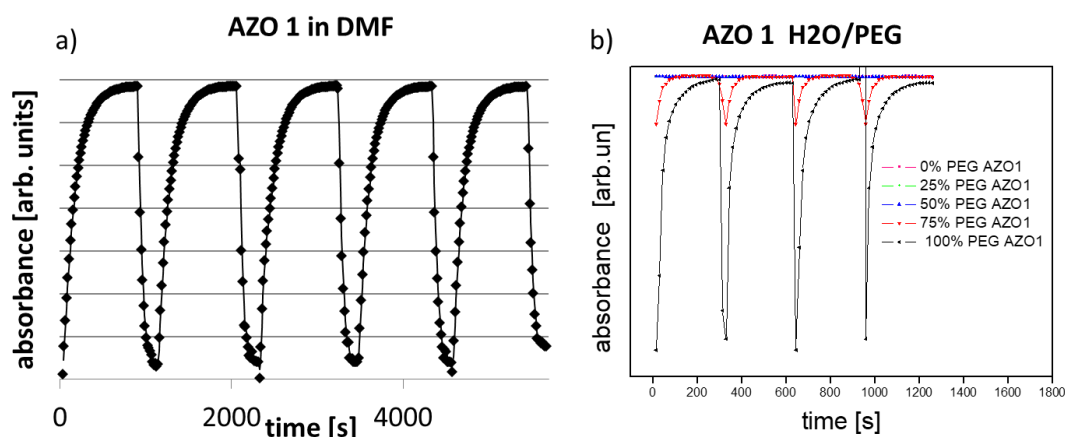


Figure 85. Changes in optical absorption of AZO1 as a function of time a) DMF and b) different mixtures of water and PEG, ranging from pure water till pure PEG.

However, the absence of changes in the absorption spectrum of AZO1 in water can be also motivated by the by a very fast *cis* \rightarrow *trans* reverse switching. In static experiments the limit to measure the switching corresponds to the experimental limitation of few seconds. In order to clarify this point, we used FTAS performed measurements.

We irradiated a solution of AZO1 50 μ M in DMF with a pump pulse at 410 nm, which corresponds to the maximum of the static absorption of the *trans* form. In analogy with the TA spectra of other azobenzene molecules,¹²⁷ the transient spectrum (see figure 86) clearly shows feature coming from the *trans*-form of AZO1. in particular, positive signals in the range 450 - 750 nm (few picoseconds time decay) that can be assigned to excited state absorption and a negative signal around 380 nm (hundreds of picoseconds time decay) due to the ground state bleaching. Also visible is a very weak positive signal at 345 nm. This feature is due to photoinduced absorption from the vibration excited *cis*-AZO1, which is produced by the pump irradiation of the sample. This signal is probably cut on

the high energy side by the edge of the white light which hides the actual intensity of the signal.

Analogous experiment was performed on a water solution of AZO1 (100 μM). Also in this case, the transient measurements seem to indicate that the trans - cis isomerisation does take place but the induced absorption signal of the cis product is less intense.

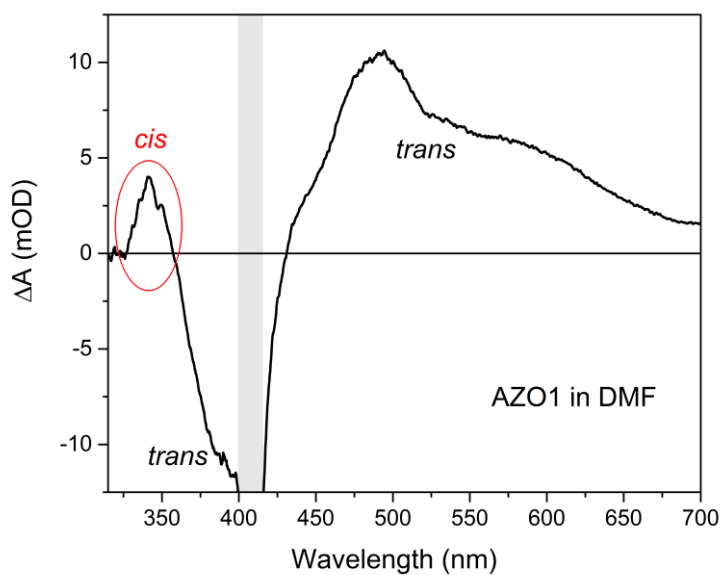


Figure 86. Transient spectrum of AZO1 50 μM in DMF with a pump pulse at 410 nm ($280 \mu\text{J}/\text{cm}^2$). The time delay between the pump and the probe is 0.65 ps. The shaded area in the spectrum shows an intense negative feature due to scattered pump radiation around 410 nm.

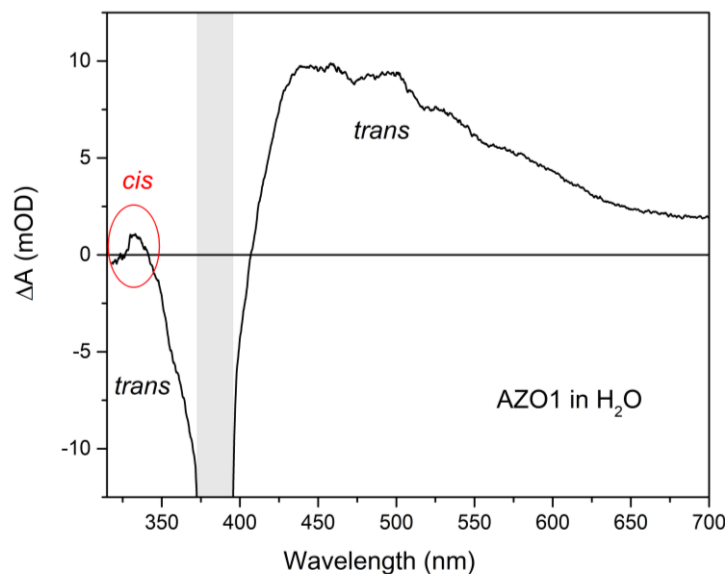


Figure 87. Transient spectrum of AZO1 100 μM in H_2O with a pump pulse at 385 nm ($280 \mu\text{J}/\text{cm}^2$). The time delay between the pump and the probe is 0.5 ps. The shaded area in the spectrum shows an intense negative feature due to scattered pump radiation around 385 nm.

Nevertheless if we consider minor effects coming from the solvent viscosity, these findings point that the increase in the solvent polarity enhances the kinetics of the cis \rightarrow trans isomerization.⁷⁰

Once the photoisomerization process of the molecules in solution is assured, we then tried to study the switching of AZO1 molecules in a much more constrained and demanding environment, i.e. in self-assembled monolayers (SAMs). Switching of azobenzene based SAMs has been already measured at the macroscopic level, using I-V spectroscopy¹¹⁵ optical spectroscopy,¹¹⁶ X-rays absorption spectroscopy¹¹² and contact angle measurements.¹¹⁷ In such assemblies, the molecules are arranged in 2D arrays featuring high crystallinity, and they are typically oriented with the long axis perpendicular on the substrate.

Here we tried a different approach to observe switching at nanoscale level, in nanometric islands of AZO1, by using KPFM. Such technique is able to measure changes in surface potential, and it has been successfully applied to study changes in dipole moment in the monolayer.^{128,129} In particular, SAMs based on azobenzenes absorbed on Au(111) showed a change in the surface potential

upon photoimerization ranging from a few to 100 meV depending on the chemical structure.¹³⁰

AZO1 molecules were deposited on flat silicon substrates by drop casting from 0.01 g/L solutions in water solvent. By tuning the deposition conditions, we could obtain well-defined islands with a lateral size of ca 1 μm and a uniform thickness of 2.35 ± 0.07 nm, as measured by AFM measurements performed on a statistic sample of 170 islands.

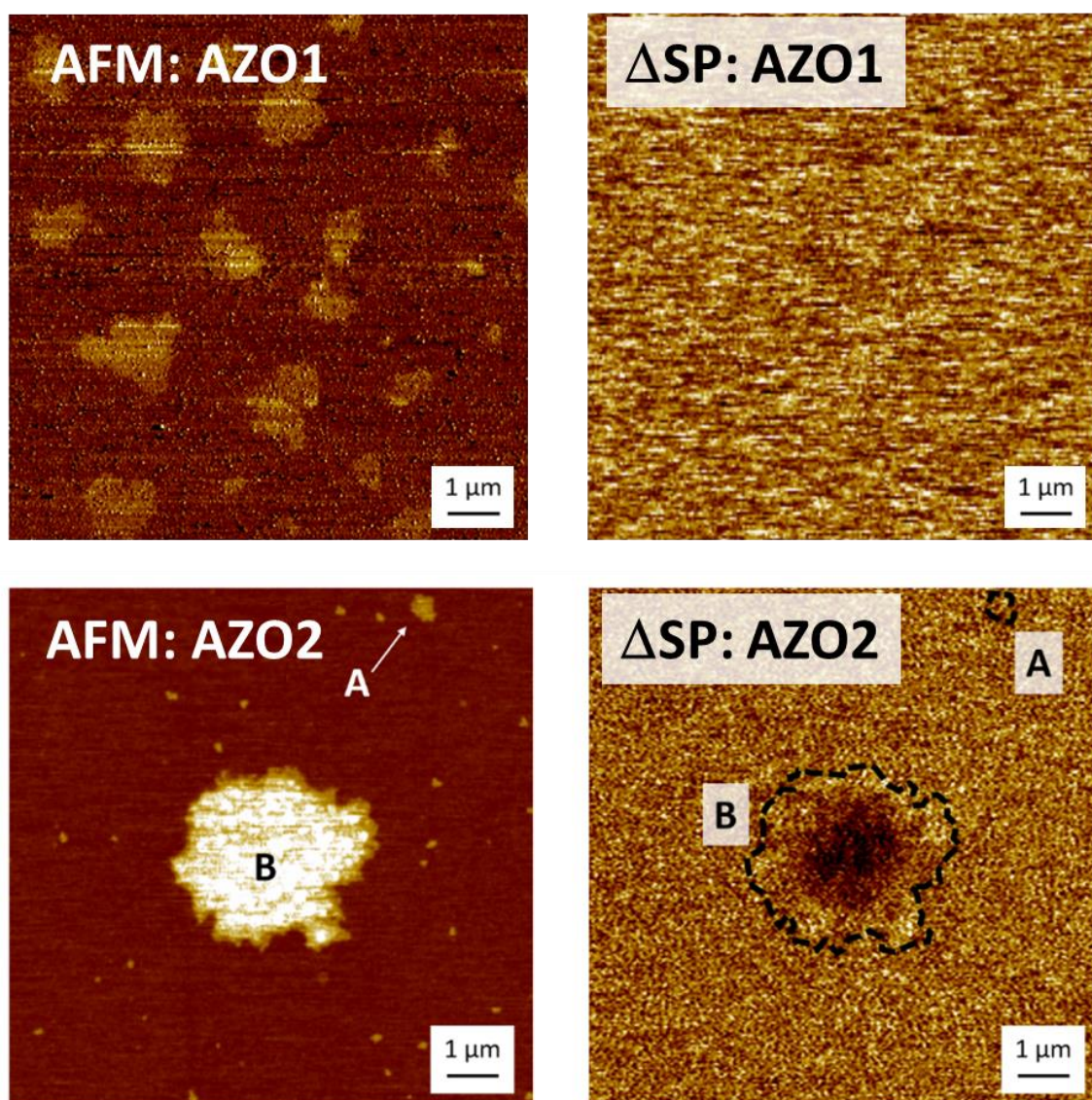


Figure 88. AFM topography and corresponding Surface potential maps (ΔSP) measured on AZO1 and AZO2 islands deposited on ultraflat silicon substrate. ΔSP maps are obtained by comparing the KPFM images acquired after and before irradiation at 365 nm for 60 min: $\Delta\text{SP} = \text{KPFM}_{\text{trans}} - \text{KPFM}_{\text{cis}}$. Z-ranges. AFM images = 8 nm, ΔSP images = 30 mV.

Such uniform thickness indicates an ordered arrangement of the molecules on the substrate. Though, it is much higher than the molecular length in trans-conformation (≈ 1.4 nm, estimated by Molecular Mechanics). Differently from previous studies of azobenzenes SAMs, AZO1 is a high polar salt, thus the presence of Na^+ hydrated counter-ions (diameter in bulk solution diameter of 0.72 nm) with a significant amount of water molecules should be considered within the SAM.

The presence of such charges is a problem for the measurement, because it will act as a double layer, thus screening significantly the changes in the SAM dipole moment due to the switching. As a consequence, no changes of surface potential would be observed by KPFM at the nanoscale.

In order to check that the lack of KPFM signal was due to the presence of charged groups, we used a similar approach with AZO2 (Figure 88). This compound is a more conventional azobenzene bearing no charges, which possess an electron-donor NH_2 group on one phenyl ring, and an electron withdrawing NO_2 group on the other; thus giving rise to a significant dipole moment (14.08 D), comparable to the one of AZO1.

This donor-acceptor asymmetric functionalization causes a strong charge transfer character to the π - π^* transition, which is then red-shifted and overlaps the n - π^* transition, thus lowering the energy barrier between the cis and trans forms and making the switching process extremely easy at room temperature. Such molecule could thus be able to switch even in sterically hindered situations. Due to the lack of sulphonic groups, AZO2 is much less soluble than AZO1 and then it cannot be processed in many solvents. In this case, AZO2 can be solubilized in DMF solvent, where it showed ultra-fast switching, similarly to AZO1 in water.

We successfully assembled AZO2 molecules in SAM, forming two different

classes of islands: i) aggregates smaller than 100 nm with thickness comparable to the AZO1 and ii) larger size islands (few microns) with height of 4.5 ± 0.4 nm. In this case, the reversible cis-trans switching was observed at the nanoscale due to the changes in the KPFM signal. We define ΔSP as the potential difference between the surface potential measured in cis- and trans- configuration (i.e. after and before UV-light irradiation at 365 nm). Figure 88 shows the SP map acquired on single islands of AZO2 SAM. While no significant modification of the topography was observed upon irradiation, a significant, reversible change of the surface potential about 30 ± 10 mV was measured on single islands by KPFM upon illumination at 365 nm for 60 min. KPFM images acquired before and after the illumination are reported in SI. The magnitude of these values is in agreement with the measurements performed on continuous SAM layers,¹²⁹ which though did not reach the single-island lateral resolution obtained here. This fact remarkably demonstrates that it is possible to measure the switching of small ensembles of molecules in real time. Assuming a typical island of $1\times 1\ \mu\text{m}^2$ and, an average footprint of a typical azobenzene molecule of $\approx 0.5\ \text{nm}^2$ obtained from STM measurements,¹⁶ we end up with the estimation that each switching island is formed by $\approx 10^{18}$ moles of azobenzene.

Finally, we tried to measure cis-trans switching also in 3D structures. Coordinated switching of molecules in bulk solids is much more challenging than in solution or in nanostructures, due to the much larger sterical constraints, and the significant rearrangements needed to accommodate the new molecular packing, see the works of Feringa et al.¹⁶ Koshima et al.¹³¹ or Horje et al.¹³² for the sake of illustration.

We were able to assemble 3D mesoscopic crystals for both AZO1 (figure 89a) and AZO2 molecules on silicon substrates. AZO1 assembled in large elongate crystals with typical dimensions of $20\times 2.7\times 22\ \mu\text{m}$ (figure 89). Moreover, AZO2 could

assemble as well in slightly more disordered crystalline structures with typical dimensions of $10 \times 1 \times 0.16 \mu\text{m}$.

The crystallinity of the structures was confirmed also by AFM measurements performed on the surface, which showed pits and steps of thickness $\approx 1.6 \text{ nm}$, comparable to the length of AZO1 molecule. Unfortunately, in these 3D structures no switching behaviour was observed at the nanoscale by means of KPFM. On the other hand, both AZO1 and AZO2 showed changes in their reflectance upon illumination at 365 nm for 30 min (figure 89) as measured by reflectance microscopy.

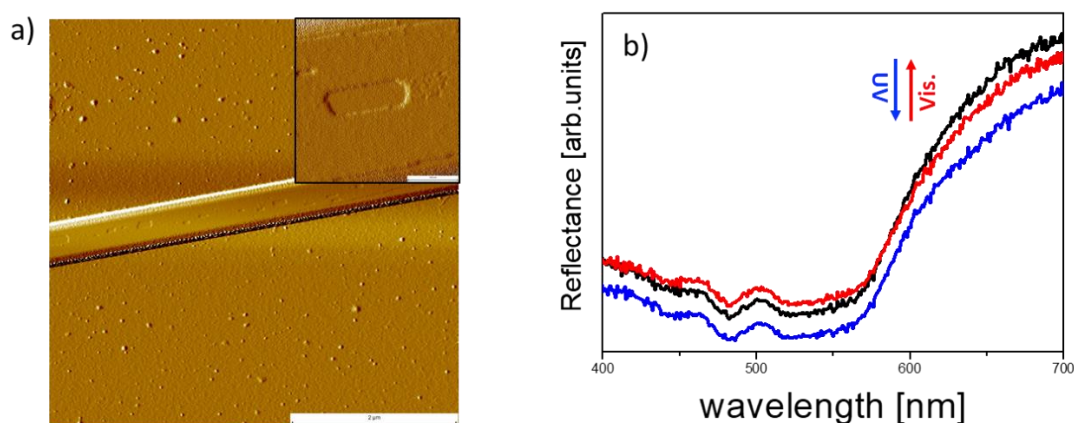


Figure 89. a) phase-AFM topography image of mesoscopic AZO1 crystals self-assembled on silicon. b) Reflectance spectra of mesoscopic AZO1 layer during exposure to UV Black line (initial one). Blue line after 30 min exposure to UV $\lambda=365\text{nm}$ ($P_d=3.2 \text{ mW/cm}^2$). Red line after 30 min exposure to Vis $\lambda=440\text{nm}$ ($P_d=0.56 \text{ mW/cm}^2$).

In conclusion, we studied the conformational switching of azobenzene molecules in a wide range of different environments. The switching kinetics of a single type of azobenzene range from extremely fast, as it is the case of AZO1 in water, to few seconds timescale, in less protic and polar solvents, being then completely hindered in 2D monolayers or 3D crystals. While optical spectroscopy is suitable to study intermediate switching dynamics, more refined techniques such as FTAS or KPFM should be used to study such processes with either high temporal or high spatial resolution.

Theoretical Calculations: DFT calculations have been applied to two azobenzene based compounds functionalized with different electron donor (D) and acceptor (A) groups (see figure 90). In the first case (AZO1), one azobenzene ring is decorated with one sulfonic acid (D) and one amine (A) groups in meta- and para- positions respectively; while the other ring is substituted with a sulfonic acid sodium salt in a para- position. In the latter case (AZO2), the azobenzene rings are substituted with nitro (D) and amine (A) groups in the para- position. For compound AZO1 the effect of the solvent polarity has been determined by studying three different solvents: polyethylene glycol (PEG), dimethylformamide (DMF) and water (H₂O). On the other hand, compound AZO2 has been studied in DMF solvent.

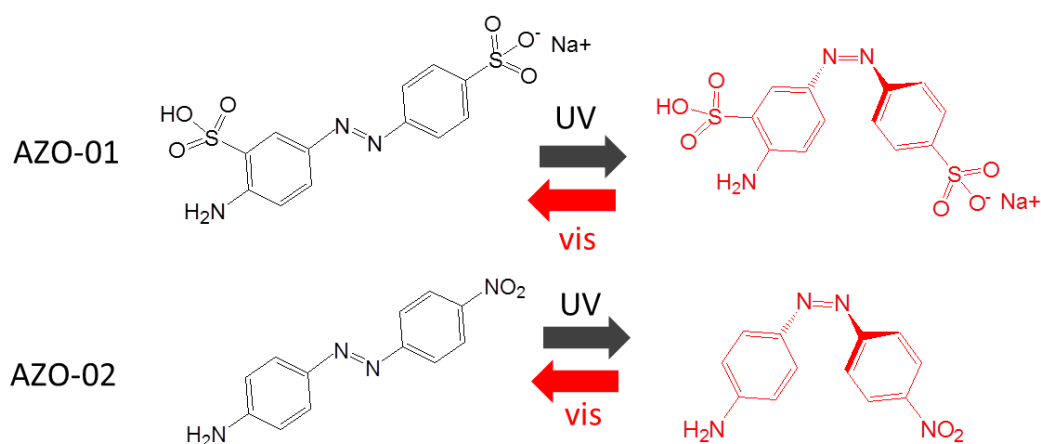


Figure 90. Schematic representation of the two azobenzene based compounds under study.

Table 7 collects the ground state energies for the different systems. The polarity of the solvent produces a stabilization of the different compounds, while difference in energies between isomers is not highly affected by the effect of the solvent or the nature of the substituents (AZO1 vs AZO2). Regarding the electronic properties, the frontier energetic levels are independent of the solvent polarity. However, due the stronger donor character of the nitro respect the sulfonic acid group, AZO2 compounds present a lower bandgap respect their respective isomers of AZO1 (0.72 eV and 0.61 eV for trans- and cis- isomers).

Table 7. Ground state properties for the different systems under study: relative energy (ΔE_{rel}) respect the less stable compound (cis- isomers in PEG and DMF for AZO1 and AZO2 respectively), difference in energy ($\Delta E_{cis-trans}$) between isomers, Lowest/Highest Un-/Occupied molecular orbital (LUMO/HOMO) level energies, electronic bandgap and dipole magnitude.

AZO solvent	isomer	ΔE_{rel} (eV)	$\Delta E_{cis-trans}$ (eV)	HOMO (eV)	LUMO (eV)	Bandgap (eV)	μ (D)	
1	PEG	trans	-0.62	0.62	-5.93	-2.47	3.45	8.81
		cis	0		-5.82	-2.26	3.56	12.86
	DMF	trans	-0.78	0.63	-5.93	-2.48	3.45	8.69
		cis	-0.14		-5.82	-2.26	3.56	15.76
	H ₂ O	trans	-0.82	0.63	-5.92	-2.45	3.47	8.87
		cis	-0.19		-5.81	-2.25	3.56	15.91
2	DMF	trans	-0.61	0.61	-5.63	-2.9	2.73	14.08
		cis	0		-5.63	-2.67	2.95	10.24

The calculated TD-DFT spectra of compound AZO1 for the different solvents are represented in Figure 91. All trans form simulated spectrum presents the main signatures of the trans azobenzene absorption spectrum with the $\pi \rightarrow \pi^*$ transition (H \rightarrow L) at 390 nm dominating the absorption. The cis form spectrum presents the typical characteristics of cis- azobenzenes with the lowest energy $n \rightarrow \pi^*$ transition (H \rightarrow L) at 480 nm and higher energy transitions (H-1 \rightarrow L) around 335 nm (see Table 2). All absorption bands described are blue shifted and lowered in intensity when increasing the polarity of the solvent.

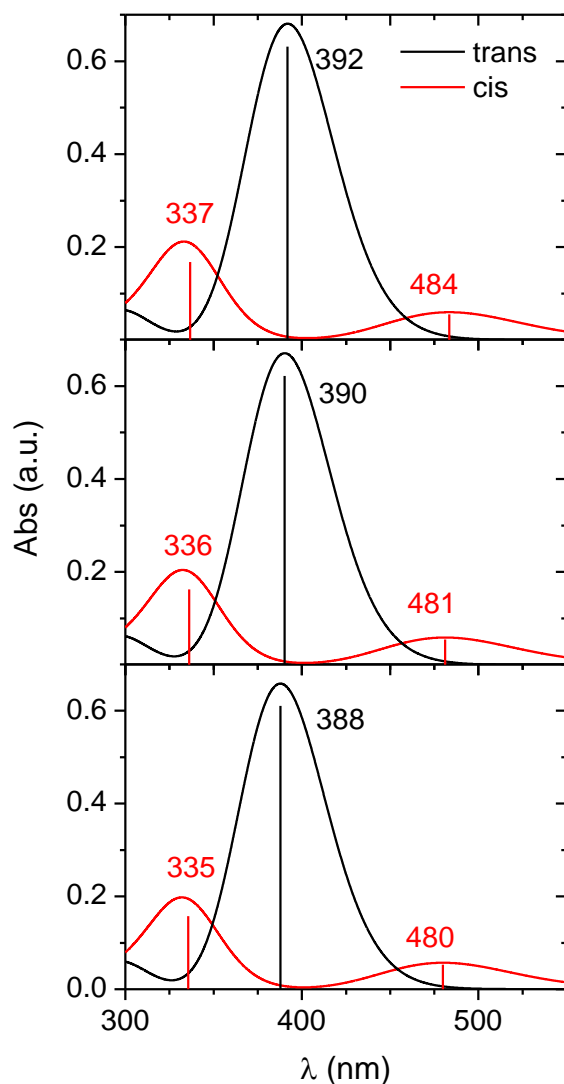


Figure 91. Calculated UV-VIS spectra of compound AZO1 in trans (black) and cis (red line) isomers in PEG, DMF and H₂O solvents (from top to bottom). The vertical lines and numbers depicted in the graph represent the magnitude and wavelength of the main optical transitions respectively.

The calculated spectra of compound AZO2 is considerably red shifted respect AZO-1 due to the band gap decrease described before. Since this effect is higher in the case of the trans form (94 nm vs 36 nm for trans and cis isomers), the lowest energy absorption bands for both isomers (trans $\pi \rightarrow \pi^*$ and cis $n \rightarrow \pi^*$ bands) are overlapped. This fact makes difficult the resolution of both isomers at experimental level.

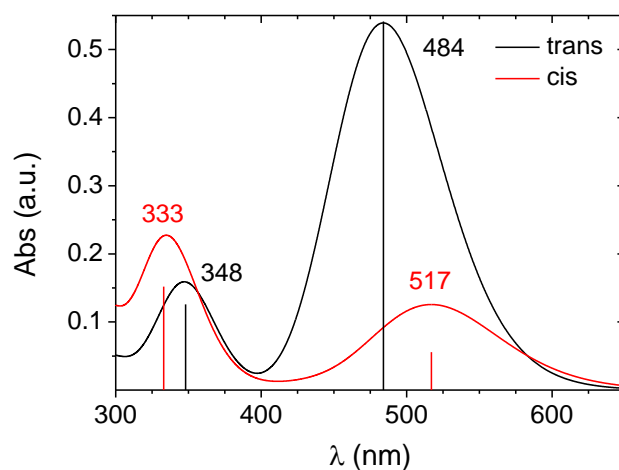


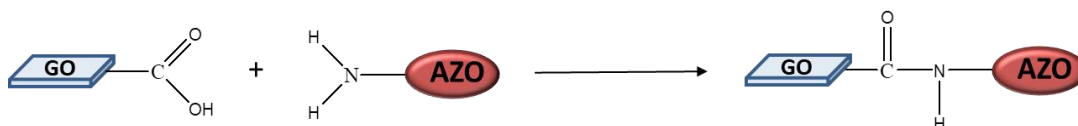
Figure 92. Calculated UV-VIS spectra of compound AZO2 in trans (black) and cis (red line) isomers in DMF solvent. The vertical lines and numbers depicted in the graph represent the magnitude and wavelength of the main optical transitions respectively.

Table 8. Excited state properties in the UV-VIS region for the two azobenzene compounds under study: wavelengths (λ), oscillator strengths (f), major contributions and related percentage (%) of the main optical transitions.

AZO	solvent	isomer	λ (nm)	f	Mayor Cont	%
1	PEG	trans	392	1.26	H→L	70.5
		cis	484	0.11	H→L	64
	DMF	trans	337	0.34	H-1→L	59.3
		trans	390	1.24	H→L	70.6
		cis	481	0.11	H→L	63.7
	H ₂ O	cis	336	0.32	H-1→L	59.2
trans		388	1.22	H→L	70.3	
cis		480	0.11	H→L	63.5	
2	DMF	trans	336	0.32	H-1→L	59
		trans	484	1.22	H→L	70.7
		trans	348	0.28	H-1→L	67.4
		cis	517	0.13	H→L	63.1
		cis	333	0.34	H-1→L+1	52.2

5.2.2 Covalent Functionalization (XPS-XRD)

After the molecules were studied in different environments, the following reaction was performed. The amino group of the azo molecules reacts with the carboxylic group of the GO, resulting and amide group, which forms a covalent bond.



Work-up:

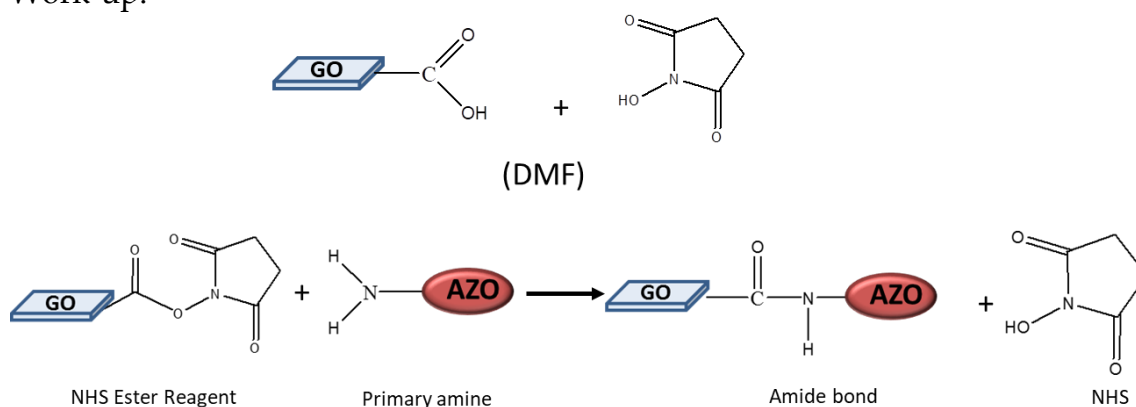


Figure 93. Scheme of the covalent functionalization of GO with azobenzene molecules.

The resulted GO was washed several times to ensure that there were no residual azobenzenes which could alter the chemical characterization of the product.

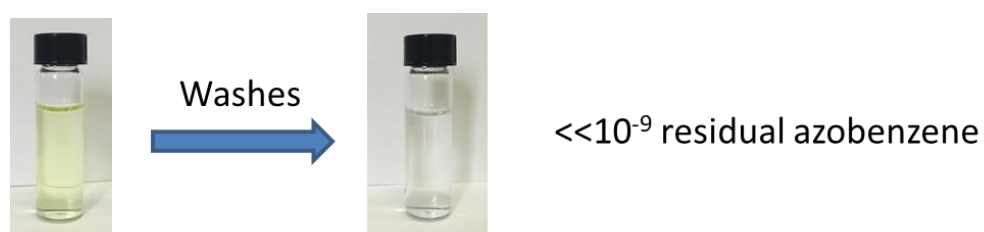


Figure 94. Picture of residual azobenzene after functionalization.

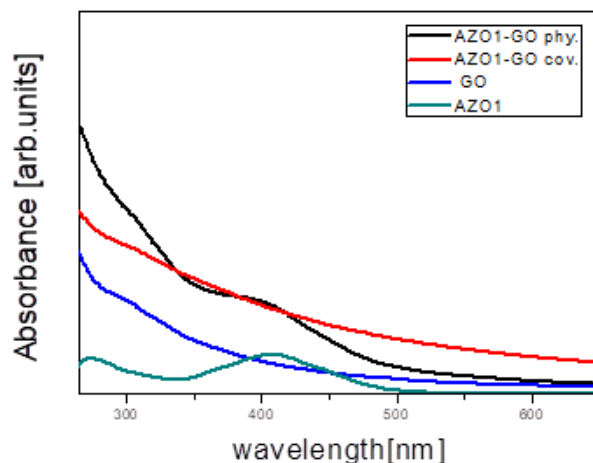


Figure 95. UV-vis absorption spectra of GO (blue), azobenzene (green), GO-AZO covalent (red), GO-AZO physisorbed (black).

- Covalent or supramolecular functionalization tested.
- Poor signal observed, due to strong adsorption of GO.

In order to verify the covalent functionalization, XPS analysis was performed:

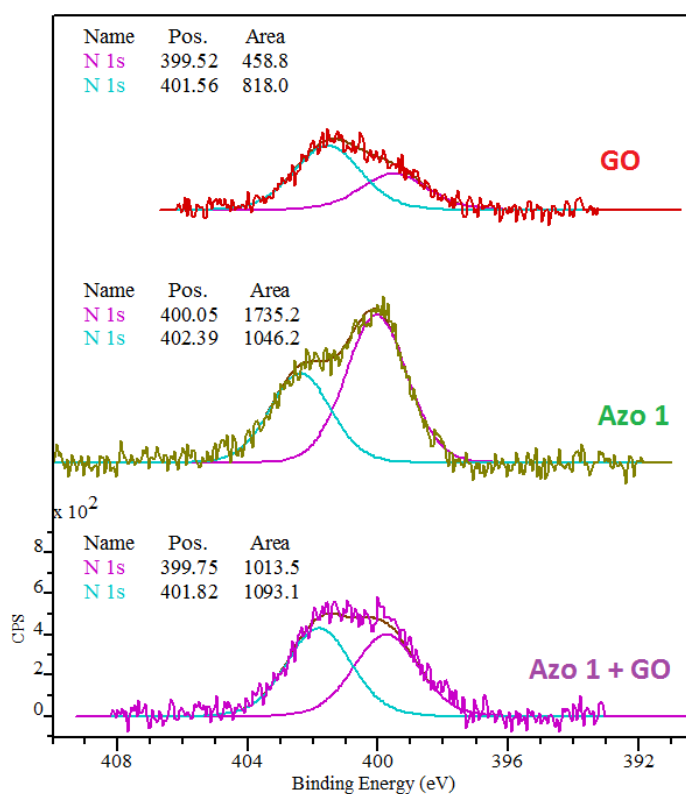


Figure 96. XPS spectra of GO, azobenzene, and GO after covalent functionalization.

The new amide bond, formed by the covalent functionalization was demonstrated by XPS.

6 AZO MEMBRANE

The current chapter is the first step to develop GO-PAH composites. For this reason, the two materials are separately investigated and after mixed.

6.1 Fabrication of GO-PAH Membrane

In this chapter the capability to produce a macroscopic AZO-GO membrane is verified: The surface properties and the spacing of the 2D nanochannels can be conveniently controlled by modifying the starting sheets.

After the study of switching of azobenzenes and the functionalization of GO with these molecules, we developed several smart nanofluidic systems with azobenzene-based gating. In these nanosystems, the modification covers the whole interior surface of the nanochannels.

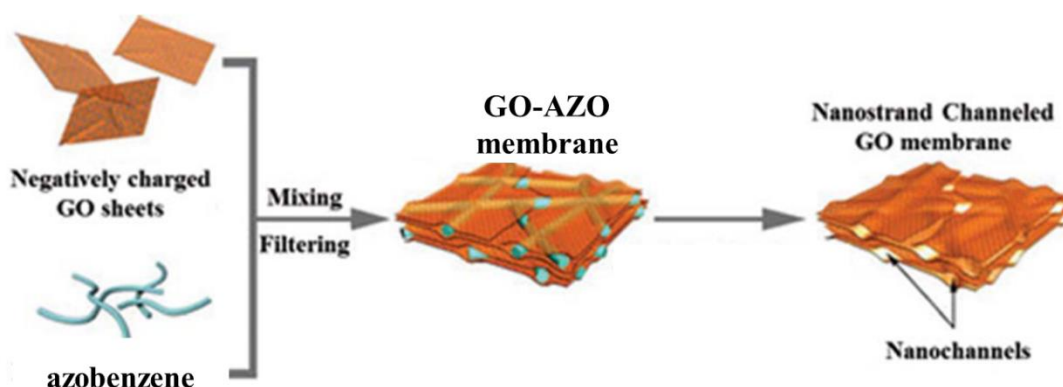


Figure 97. Scheme of GO-AZO membrane.

6.2 Switching of GO-PAH Membrane:

The aqueous suspension of GO-AZO was prepared by dispersing GO flakes in distilled water using bath sonication for 4 hours. The resulted suspension 1mg/mL was filtered onto an anopore inorganic membrane composed of aluminum oxide by vacuum filtration method ($0.02\mu\text{m}$, diameter 47 mm, purchased from Whatman). The membranes were fished and cut into rectangular strips of dimension of 3 cm x 1 cm. The strips were then covered with a $500\mu\text{m}$ PDMS slide both sides by an *in situ* cross-linking using a Film Applicator and

Drying Time Recorder Coatmaster 510.



Figure 98. Picture of the GO-PAH membrane obtained.

The isomerization of AZO1 is 0.37nm, meaning that a nanochannels could be tune in a range of 4 Å, which is a very interesting distance for ion transport (3-9Å).

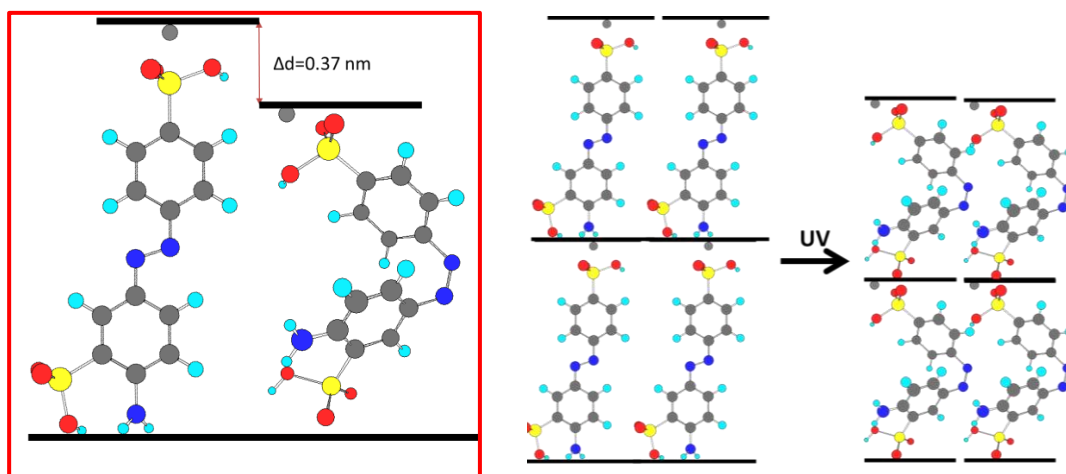


Figure 99. Dimensions of the isomerization of AZO1.

A thin film was deposited in a quartz substrate and analysed by UV-VIS measurements before and after irradiation.

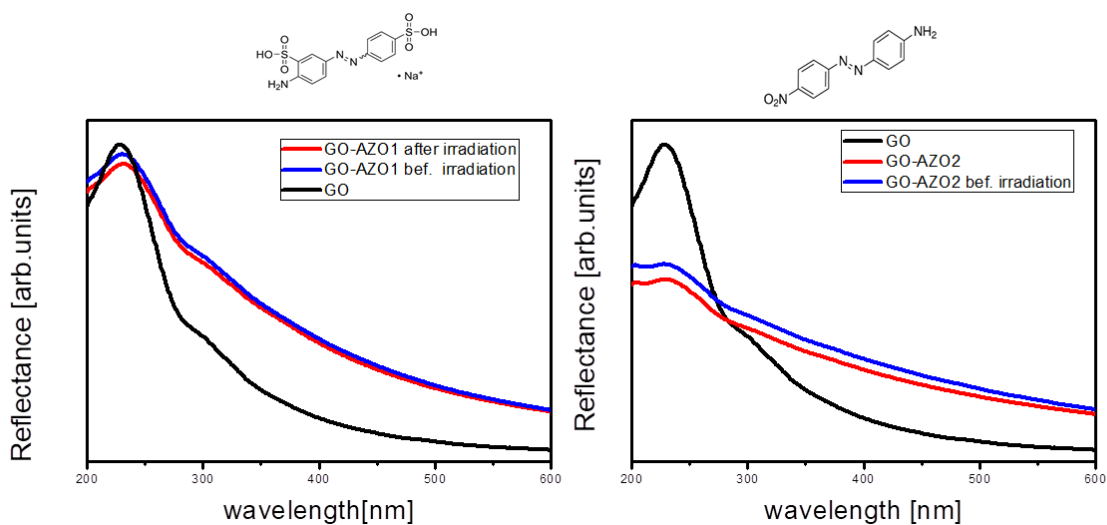


Figure 100. Spectroscopy characterization of GO, AZO1-GO, and AZO2-GO. UV/vis absorption spectra recorded in water after 30min of irradiation.

XRD measurements

To demonstrate the switching inside the membranes, some XRD measurements were performed:

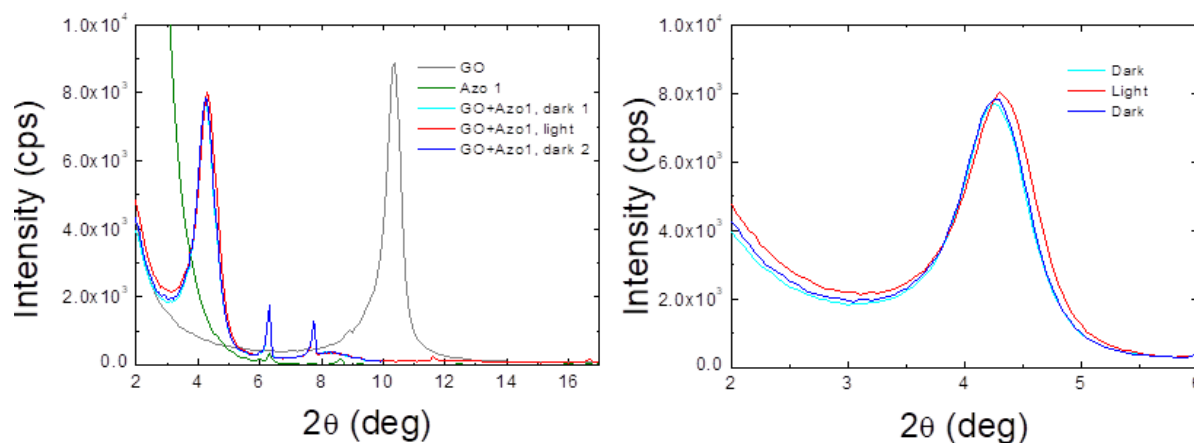


Figure 101. XRD spectra of GO-AZO1 before and after UV irradiation.

Specular scans were collected on 3 samples: GO on SiO₂, Azo on SiO₂ and Azo:GO on SiO₂. When GO is drop casted on SiO₂, membranes with an average thickness of 37MLs (16nm thick) are formed. When Azo is drop casted, molecular crystals are formed.

Spacing of 2nm suggesting that molecules are oriented edge-on with respect to GO surface.

Real time XRD scans were collected in dark and light exposure.

In dark, the layer spacing is 2.08nm.

When sample is illuminates Bragg peak

- 1) slightly shifts towards higher angles, corresponding to a spacing of 2.05nm
- 2) slightly broaden indicating a decreasing of the membrane thickness (from 11.3 nm to 11.2 nm)

This very tiny effect is reversible. The experiment was repeated 4 times at several time exposure. The error bar used in this set-up was 0.001 nm.

Conclusions:

- XRD confirms the presence of AZO1 intercalated in between GO sheets, likely edge-on.
- Reversible change of inter-sheet spacing observed during irradiation.
- The decrease of 0.2nm of the thickness membrane indicated that the trans to cis isomerization is 27.1% efficiency.

7 GOM FOR SENSOR APPLICATIONS

The current chapter introduces several applications of GOM for biosensing.

7.1 Prototypes Biosensors

Electrochemical sensors:

Electrochemical sensors convert the information associated with electrochemical reactions (the reaction between an electrode and an analyte) into an applicable qualitative or quantitative signal. The electrochemical sensors are mainly divided into three types: potentiometric, conductometric, and amperometric/voltammetric.²⁹

Electrochemical sensors can produce electronic outputs in digital signals for further analysis as per the steps as shown in Figure 102. Generally, the reactions found in these sensors are because of the chemical and electrical interactions, which are ultimately based upon the conductometric, amperometric, and potentiometric measurements. Electrochemical transducers are the most commonly used transducers in the construction of innovative sensors including biosensors. They rank first in terms of their availability on the market and have already shown their true benefits. Electrochemical determination is superior to other measurement systems due to its quick and easy features.¹³³

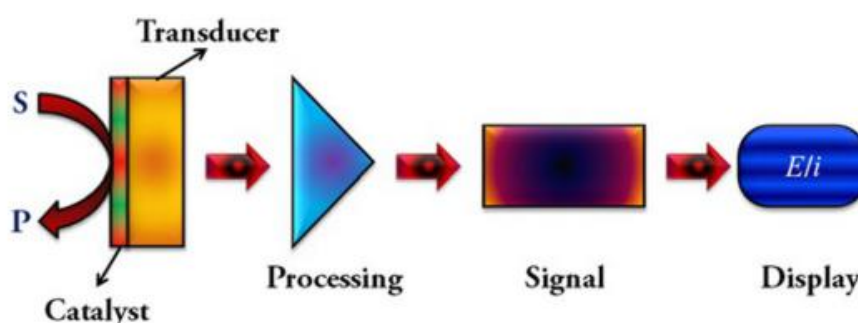


Figure 102. The main stages in the sensor operation.²⁹

The possibility of automation and manufacturing of small sensors is of great benefit for scientific purposes. Electrochemical sensors have many benefits over the conventional analytics that will lead to definite usage in the near future. They

are a fascinating scientific tool because of the innate selectivity and sensitivity towards electroactive analytes, occasionally due to the accuracy and specificity, they are less time consuming, have flexibility and are easy to set up. They are lightweight and transferrable devices, easy to use and compact; resulting in swiftness in research data arrangement. The choice of appropriate functional principles, the design, and the material of a sensing toolbox depends on aspects such as portability, selectivity, sensitivity, the need for single or multivariate discovery, and any appropriate field applications. The choice of fabrication procedures and resources is important for the function of the sensors, and the performing ability of the sensors frequently depends on these important parameters. Therefore, future developments in device design should focus on developing innovative materials and novel technologies. The trends of using nanomaterials and porous particles in electrochemical sensing tools to improve selection and volatility have been progressively growing.

Conductometric sensor method:

The conductivity of liquids results from the dissociation of the dissolved substance, an electrolyte, into ions and the migration of the latter induced by an electrical field. When a potential difference is applied to the electrode, there is an electrical field within the electrolyte, so the chaotic ion movement is influenced by the ordered, oppositely directed movement of ions (those with negative charge move more towards anodes, while positively charged ones move towards cathodes) (figure 103).

Thus, the current in the electrolyte is caused by the ion movement towards the electrodes where the ions are neutralized and isolated as neutral atoms (or molecules) if there is a high enough voltage ($2\text{Cl}^- \rightarrow \text{Cl}_2 + 2\text{e}^-$ $E = -1.36\text{V}$); in this experiment the applied voltage is $\pm 0.5\text{V}$, then electrolysis will not occur. The electrical resistance of pure water is too great to allow electrons to flow through it. Adding electrolytes (which dissociate to form positive and negative ions) reduces the resistance and creates an excellent environment for electrons (current) to flow across our membrane.

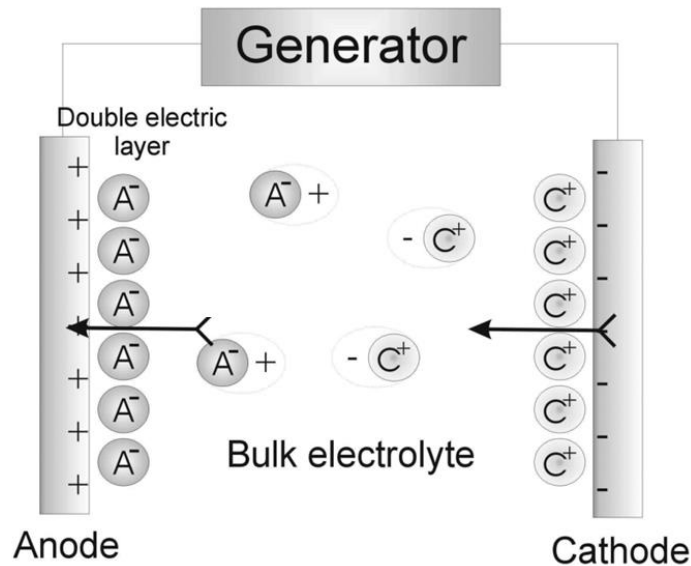


Figure 103. Ion migration in the solution volume and electrolyte conductivity.¹³⁴

We revise the model presented in chapter 4.5.

The ion flux, i.e. the concentration of ions passing through a unit of electrolyte cross-section per unit of time ($\partial C/\partial t$) can be given by a generalization of the formula reported in the eq.4.5.1.d:

$$\frac{\partial C}{\partial t} = v_s C - \vec{v}_E \cdot \nabla C + D \nabla^2 C \quad (7.1.a)$$

where v_s is the speed of solution flow due to natural or forced convection; C the ion concentration; D the diffusion coefficient; \vec{v}_E is the ion velocity driven by an electric field E , is given by $|\vec{v}_E| = \mu z F E$, where μ is the ion mobility, z is the ion charge number, F is Faraday's constant.

Thus, we can distinguish three terms: the first one corresponds to the contribution of the convective flow of ions for a given concentration; the second one to the ion migration induced by the applied field and the third is related to the contribution of their molecular diffusion.

In the case of homogenous and immobile electrolyte the first and third terms of eq 7.1.a can be neglected, and only the ion migration caused by the electric field effect can be considered. Then:

$$\frac{\partial C}{\partial t} = -\vec{v}_E \cdot \nabla C \quad (7.1.b)$$

In Table 9 are reported the values of mobility of some of the most common ions in aqueous solutions at room temperature (i.e. T = 298K).

Table 9. Ion mobility in infinitely diluted aqueous solutions at temperature of 298K in water.¹³⁴

Cation	$\mu (10^{-8} m^2 s^{-1} V^{-1})$	Anion	$\mu (10^{-8} m^2 s^{-1} V^{-1})$
H ⁺	36.23	OH ⁻	20.64
K ⁺	7.62	I ⁻	7.96
Ca ²⁺	6.17	Br ⁻	8.09
Mg ²⁺	5.50	Cl ⁻	7.92
Na ⁺	5.19		
Li ⁺	4.01		

The current density j , i.e. the current per unit of the system area (A) is given of by the flux of the ion charges:

$$J = |\vec{v}_E| \cdot C \quad (7.1.c)$$

On the other hand, according to Ohm's law

$$J = S \cdot E \quad (7.1.d)$$

where S is the conductivity (i.e. reciprocal value of resistivity).

Combining the last two equations we obtain the relation:

$$J = C \cdot \mu z F \quad (7.1.e)$$

Thus, the conductivity of the electrolyte solution depends on the ion concentration C and mobility μ . The resistance of electrolyte solution is well-known to be in direct proportion to the distance (L) between the immersed

electrodes and reciprocal to their area A , therefore:

$$S = \chi \cdot A/L \quad (7.1.f)$$

where χ is the specific conductivity.

This leads to the following conclusions: conductometric measurement commonly consists of determining the conductivity of a solution between two parallel electrodes; its value is a sum of all the ions within the solution tested.¹³⁴

Biosensors based on the conductometric principle present a number of advantages: a) thin-film electrodes are suitable for miniaturisation and large scale production using inexpensive technology, b) they do not require any reference electrode, c) transducers are not light sensitive, d) the driving voltage can be sufficiently low to decrease significantly the power consumption, e) large spectrum of compounds of different nature can be determined on the basis of various reactions and mechanisms. In addition, they can be miniaturized as planar interdigitated electrodes and integrated easily by the use of cheap thin-film standard technology.¹³⁵

The present chapter describes a sensing device for the selective detection of specific ions in biological fluids, in particular sweat. The device includes a membrane made of 2-dimensional stacked nanosheets of graphene or related materials (GRM). Ions and small solvent molecules are able to diffuse between the monoatomic sheets with variable diffusivity depending on the ionic size and charge.

A set of electrodes before and after the GRM membrane applies an electric bias to foster the drift of ions across the membrane and their detection through conductometric sensing. The novelty of the invention relates mainly to its ability to allow the transport of only selected target ions to the inner electrodes. In this way, it is possible to measure the presence and concentration of the analyte in complex matrices with no interference from other substances, thanks to the nano-sieving action of the outer membrane.

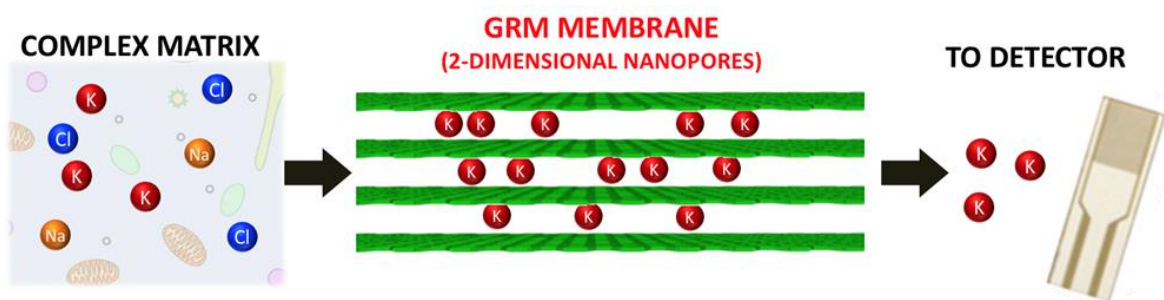


Figure 104. Scheme showing the 2-dimensional sieving effect of the GRM membrane, for detection of specific ions.

Wearable biosensors are becoming widespread in a wide range of applications, from healthcare to biomedical monitoring systems, which enable continuous measurement of critical biomarkers for clinical diagnostics, physiological health monitoring and evaluation (figure 105).^{136,137}

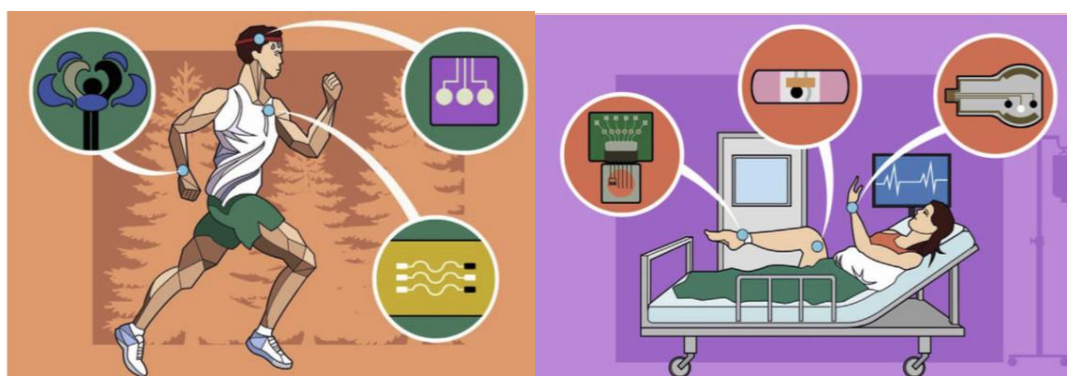


Figure 105. Examples of the two main applications of wearable sensors: health-care monitoring and sport performance.

136

Especially as the elderly population grows globally, various chronic and acute diseases become increasingly important, and the medical industry is changing dramatically due to the need for POC diagnosis and real-time monitoring of long-term health conditions. Wearable devices have evolved gradually in the form of accessories, integrated clothing, body attachments and body inserts. Over the past few decades, the tremendous development of electronics, biocompatible materials and nanomaterials has resulted in the development of implantable devices that enable the diagnosis and prognosis through small sensors and

biomedical devices, and greatly improve the quality and efficacy of medical services. Early diagnosis and continuous monitoring of diseases and conditions is crucial for their successful treatment and the improvement of people's quality of life. The availability of cost effective devices capable of bypassing pathology laboratories, could redirect resources and support comparatively rapid response and action for the patient. This path leads towards the full realization of the mobile-health vision, where portable sensors connected to cloud services and data analytics, will be able to monitor our health and wellbeing continuously and unobtrusively.

Graphene and other related 2-dimensional materials have shown interesting applications in this field. Thanks to its 2-dimensional shapes, GRM show unique selectivity for permeation of water,⁴⁴ gases¹³⁸ and small molecules.¹³⁹ Besides selective filtering, GRM showed also good performance for electrochemical sensing for biological applications, as recently demonstrated for different analytes.^{140, 141}



Figure 106. Picture of the AUTOLAB set-up.

Advantages and Potentials:

- Fast response, user friendly, customizable, tunable for new conditions, Portable, Low cost, customizable

Electrochemical Sensing:

- Instrument: pulse method by electrode cell
- $i \propto [\text{analyte}]$

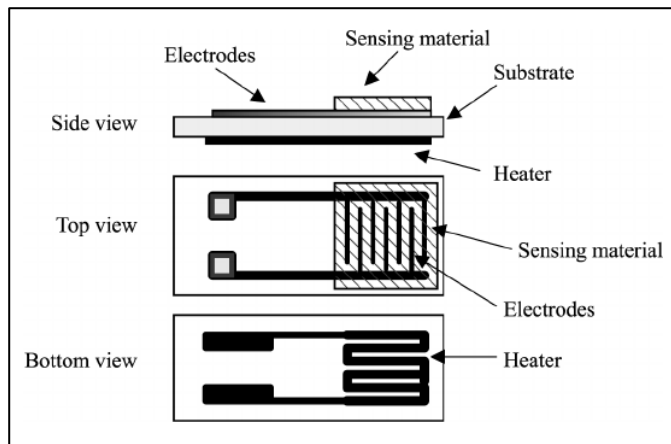


Figure 107. Scheme of an electrode for biosensing.

Prototypes:

3electrodes

With the aim to develop a suitable biosensor for real applications, different prototypes were design. One of them is by using a porous membrane in which the ionic sample (such as sweat) is deposited, then the ions will move through the membrane by capillarity, and once they arrive to the GOM membrane it will act as a filter, by applying a voltage it will be selective to positive or negative ions as was previously demonstrated in chapter 4.

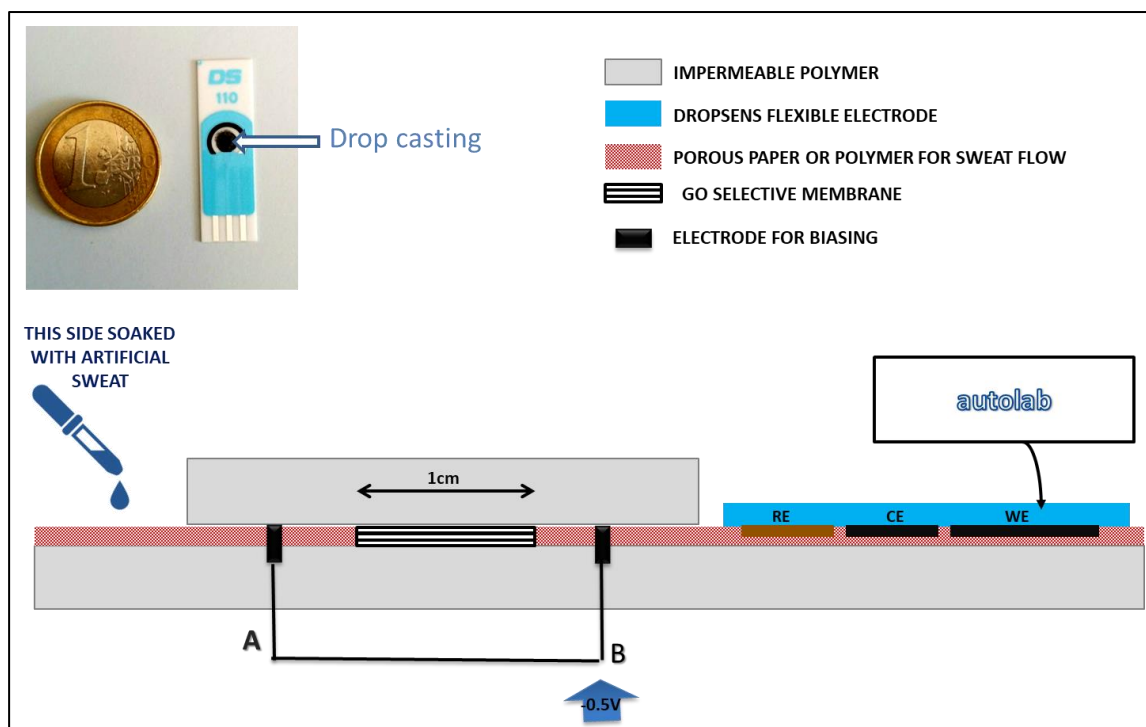


Figure 108. Scheme of the 3 electrodes prototype biosensor.

The ions arrive to the electrode, a commercial DRP- 100 which collects the sample, and afterwards the concentration of the selected ions is measured by the autolab (using the pulse method previously reported in chapter 4).

The three-electrode cell set-up is the most common electrochemical cell used in electrochemistry. In this case, the current flows between the CE and the WE. The potential difference is controlled between the WE and the CE and measured between the RE (kept at close proximity of the WE) and S. Because the WE is connected with S and WE is kept at pseudo-ground (fixed, stable potential), by controlling the polarization of the CE, the potential difference between RE and WE is controlled all the time. The potential between the WE and CE usually is not measured. This is the voltage applied by the control amplifier and it is limited by the compliance voltage of the instrument. It is adjusted so that the potential difference between the WE and RE will be equal to the potential difference specified by the user. This configuration allows the potential across the electrochemical interface at the WE to be controlled with respect to the RE.¹⁴²

(Connections available on the cell cables of the Autolab; WE: Working electrode; CE: Counter electrode; RE: Reference electrode; S: sense; Ground connection)

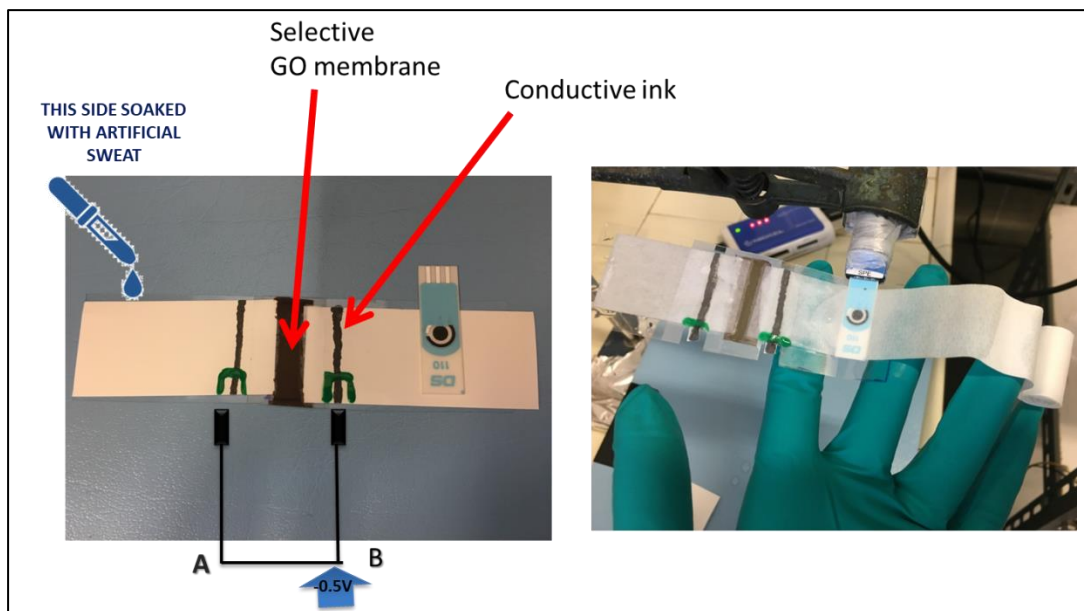


Figure 109. Picture of the 3 electrode prototype connected to the AUTOLAB.

Interdigitated electrodes

The second prototype follows the same scheme, but using a flexible-interdigitated electrode: DropSens Interdigitated Gold Electrodes over plastic substrate are composed of two interdigitated electrodes with two connection tracks, all made of gold, on a plastic and flexible substrate. These IDEs offer several advantages, such as working with low volumes of sample and avoiding tedious polishing of solid electrodes.

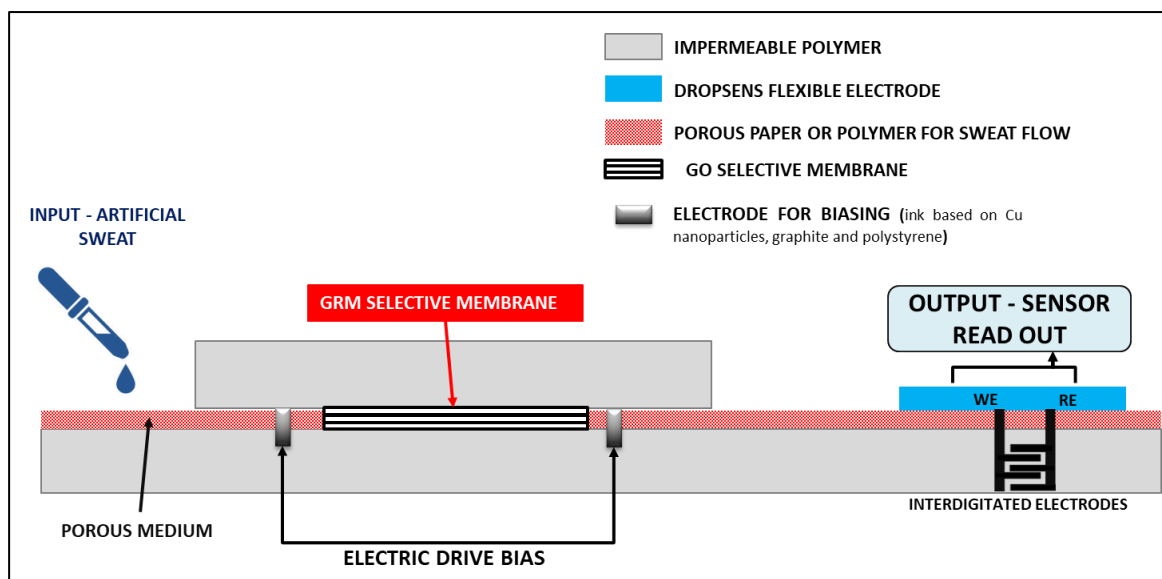


Figure 110. Scheme of the 2 electrodes prototype biosensor.

The interdigitated configuration typically enhances sensitivity and detection limits. They are suitable for decentralized assays, to develop specific biosensors and other electrochemical studies. The dimensions for bands/gaps are 100 μm . Plastic substrate dimensions: L 22.8 mm x W 7 mm x H 0.175mm.

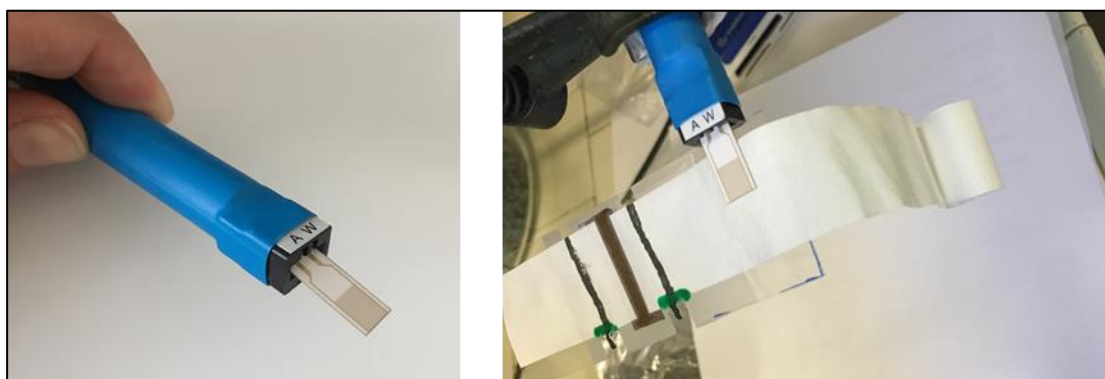


Figure 111. Picture of the 2 electrode (DRP-PW-IDEAU 100) prototype connected to the AUTOLAB.

Fabrication of the final prototype:

Selection of the porous paper: An initial solution of 0.1M KCl is passed through 3 types of membranes, from the left (A) to the right (B) and after 10 minutes the pulsed method is applied to verify the migration of the ions in the membrane. In this way, it is possible to understand how many ions remain stacked during the migration and find the most suitable porous membrane for this application. For

that purpose, three different porous filter papers commonly used in this field are tested: © Nitrocellulose Membranes CN140 Unbacked (blue). Cellulose based membrane (red) and Nitrocellulose BCN140 membrane (orange). After, the pulse method is applied in B, and the current is converted into concentration (C_B).

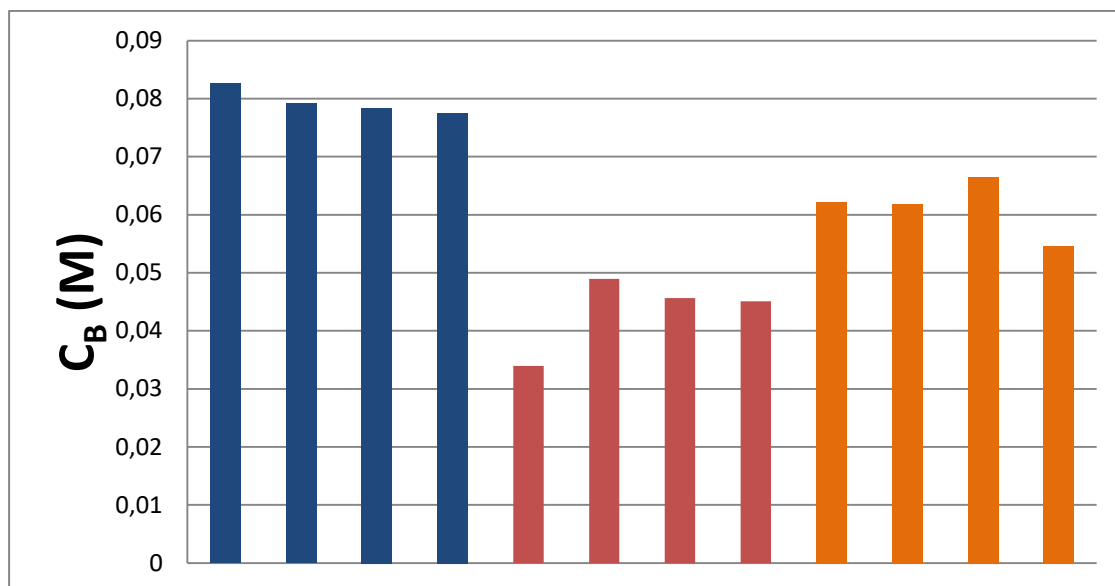


Figure 112 . Comparison of porous filter paper. Materials: © Nitrocellulose Membranes CN140 Unbacked (blue). Cellulose based membrane (red) and Nitrocellulose BCN140 membrane (orange),

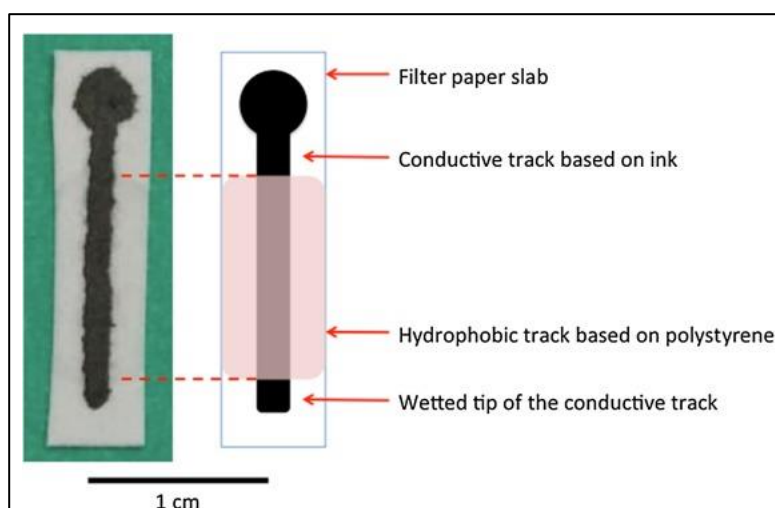
Three different membranes are tested and © Nitrocellulose Membranes CN140 Unbacked (blue bars) shows the best result.

Conductive Ink: Paper-based electrodes have been fabricated by the deposition of an electrically conductive ink based on polystyrene.

The formulation of the ink has been developed aiming at minimising its solubility in water, for best stability of the resulting electrodes. Hence, a polymeric binder such as polystyrene, only soluble in organic solvents, has been chosen. Toluene has been selected as the solvent, since it can easily dissolve polystyrene and possesses high enough vapour pressure to allow fast drying of the deposited ink at room temperature. Inks have been prepared by mixing different amounts of graphite powder in an Eppendorf flask. Then, 0.1 ml toluene

solution containing different amount of polystyrene has been added. Finally, the mixture has been sonicated for 5 min and promptly used. The ink has been deposited onto the substrates by hand, using a pipette tip, avoiding the use of any masks.

The optimized ink formulation has been employed for the fabrication of paper-based working electrodes (Figure 113). Filter papers represent the most spontaneous choice for the substrate of the ink, since additives, which may alter the electrochemical response, are basically absent in this kind of paper. In addition, filter papers are highly reproducible, inexpensive, and commercially available. Different kinds of papers have been tested in order to verify whether the porosity of the paper influences the electrochemical behaviour of the deposited ink: Actually, the immersion of the working electrode leads to the rise of the solution due to capillary forces. Hence, we deposited a hydrophobic track of polystyrene perpendicular to the working electrode, in order to prevent from capillary rise and to allow the solvent only to wet the tip of the electrode. It is worth noticing that the solvent used in this step does not modify the nature of the working electrode, no dissolution of the deposited ink being induced.



Calibration of the electrodes:

2 types of electrodes were calibrated in order to have a current-ion concentration correlation, and to check the sensitivity of the system.

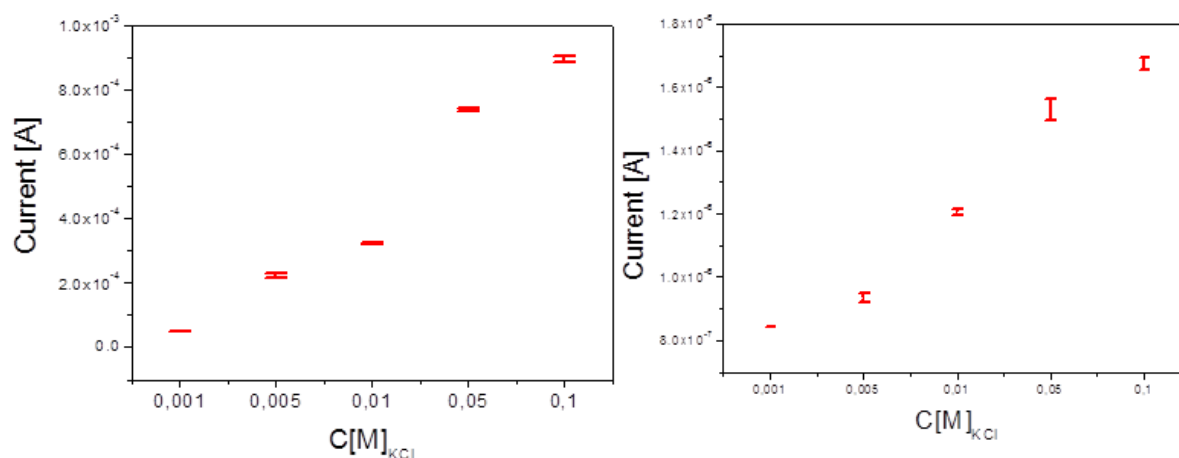
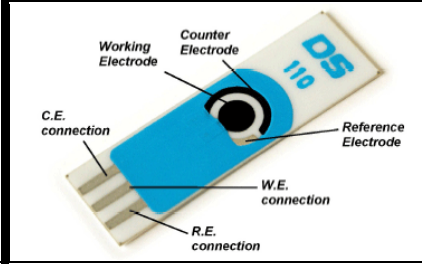



Figure 114. Calibration curve. Left: Electrode DRP- 100. Right: Electrode DRP-PW-IDEAU 100.

Table 10. Calibration of DRP- 100 and DRP-PW-IDEAU 100.

		
C [M]KCl	DRP- 100	DRP-PW-IDEAU 100
	Current(A)	Current (A)
0.1	(8.9±0.1) E-4	(1.67 ±0.02) E-6
0.05	(7.39±0.05) E-4	(1.53±0.03) E-6
0.01	(3.21±0.03) E-4	(1.20±0.01) E-6
0.005	(2.22±0.06) E-4	(9.35±0.1) E-7
0.001	(4.9±0.1) E-5	(8.450±0.003) E-7

Once all the parameters were calibrated, the final prototype was design, consisting in a wearable-flexible bracelet.

Final device (patent submitted):

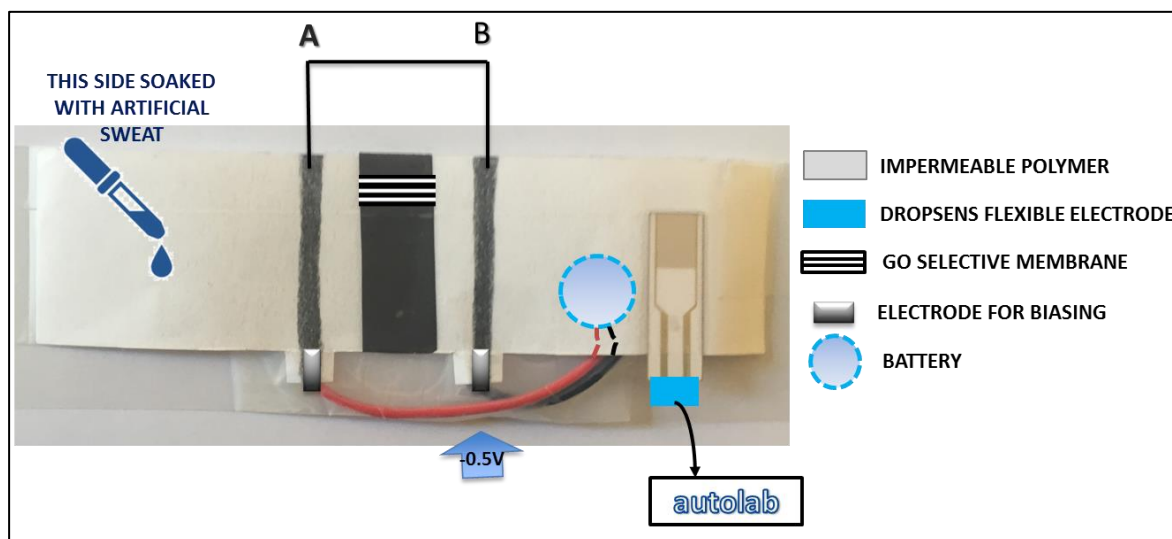


Figure 115. Scheme of the prototype bracelet for biosensing.

The bracelet consists in a porous membrane a selective GOM, 2 electrodes for biasing, a watch battery, and a dropsens flexible gold electrode.

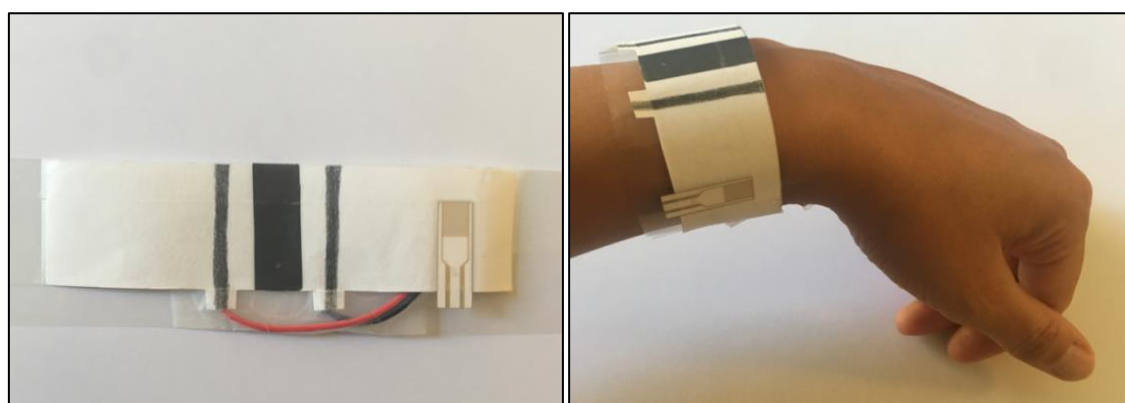


Figure 116. Left and center: photos of the prototype assembled, in this case for use as a bracelet. Final applications will likely be placed instead on the back or upper arm.

Applications:

Wearable sensor technologies are essential to the realization of personalized medicine through continuously monitoring an individual's state of health. Sampling human sweat, which is rich in physiological information, could enable non-invasive monitoring.¹⁴³

Cystic fibrosis:

Cystic fibrosis (CF), the most common genetic disorder in Caucasian populations, is caused by recessive mutations in the gene encoding the cystic fibrosis transmembrane conductance regulator (CFTR), which is a phosphorylation-dependent epithelial Cl⁻ channel. It is located primarily in the apical membrane, where it provides a pathway for Cl⁻ movement across epithelia and regulates the rate of Cl⁻ flow.¹⁴⁴

The normal range of electrolyte values in sweat in adults is up to 70 mmol/l (0.07M Na⁺) and 55 mmol/l (0.055M Cl⁻) respectively in infants 40 mmol/l (0.04M) for Na⁺ and Cl⁻.

A sweat chloride test result of less than or equal to 39 mmol/L in an infant over 6 months old probably means cystic fibrosis is very unlikely. A result between 40 to 59 mmol/L does not give a clear diagnosis. Further testing is needed. If the result is 60 mmol/L or greater, **cystic fibrosis is present.**

To test our method, we dilute the artificial sweat* in different concentrations of Cl⁻.(Artificial sweat ISO-3160-2 Methrom: 20g/L NaCl, 17.5 g/L NH₄Cl, 1.5 g/L lactic acid, 5g/L urea, 2.5 g/L acetic acid)

Table 11. Calculated parameters for Cl⁻ ions.

<i>Known artificial sweat*[Cl⁻]mM</i>	<i>Current(A)</i>			<i>AVERAGE</i>	<i>RESULTS [Cl⁻]mM</i>	
	<i>Sample</i>					
	<i>1</i>	<i>2</i>	<i>3</i>			
50	1.38E-06	1.37E-06	1.40E-06	1.38E-06	48±0.01	Non conclusive
10	1.10E-06	1.10E-06	1.10E-06	1.10E-06	12±0.01	Negative
100	1.79E-06	1.82E-06	1.80E-06	1.80E-06	100±0.01	Positive

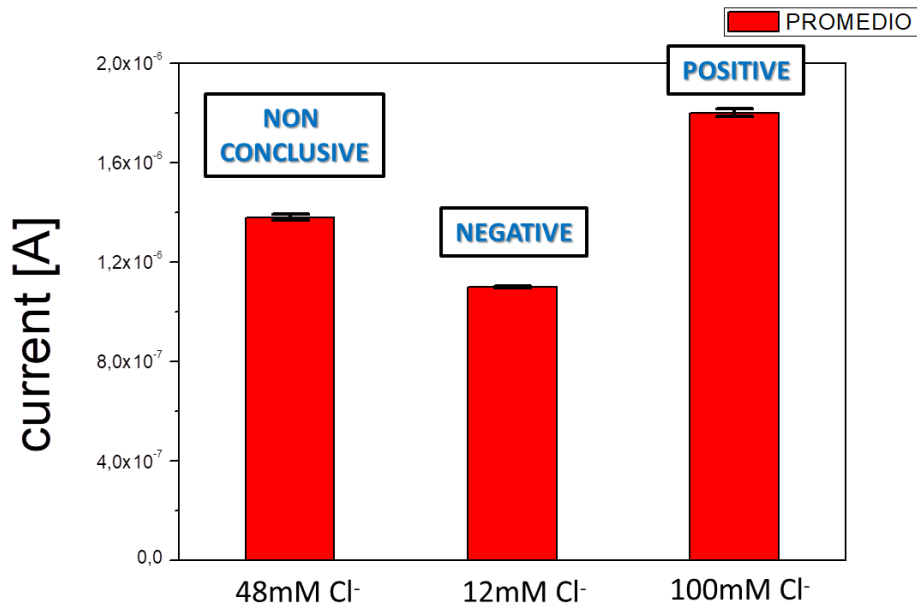


Figure 117. Graph showing 3 test, one negative (12Mm Cl⁻), one non clonclusive (48mM Cl⁻) and one Positive for cystic fibrosis (100mM Cl⁻), using artificial sweat and a known concentration of Cl⁻.

Our method successfully rejects all the components of the artificial sweat but Cl⁻ ions thanks to the selective membrane. It is possible to determine if the sweat samples are positive or negative in cystic fibrosis. The advantage of this method is that the test is not invasive, there is no need for a blood testing, and the measurement is in situ by a conductometric sensor.

Hypokalemia-dehydration

Hypokalemia refers to the condition in which the concentration of potassium in the blood is low. The main causes of hypokalemia are the insufficient consumption of potassium or the loss of potassium in the urine due to certain medications. Mild hypokalemia is often without symptoms, although it may cause elevation of blood pressure, and can provoke the development of an abnormal heart rhythm. Severe hypokalemia, with serum potassium concentrations of 2.5–3 mM, may cause muscle weakness, myalgia, and muscle cramps and constipation.¹³⁵ Doctors consider a person to have severe hypokalemia, a potentially life-threatening condition, when their potassium levels are less than 2.5 mmol/L.¹⁴⁵

Table 12. Calculated parameters for K^+ ions. $<0,0025 [K^+]M$ hypokalemia; $0.0025-0.005 [K^+]M$ normal; $>0.0055 [K^+]M$ hyperkalemia.

<i>Known artificial sweat*[K+]M</i>	<i>Current(A)</i>			<i>AVERAGE</i>	<i>RESULTS [K+]mM</i>	
	<i>Sample</i>					
	<i>1</i>	<i>2</i>	<i>3</i>			
0.0020	9.00E-07	9.13E-07	9.00E-07	9.04E-07	2.3±0.01	Hypokalemia
0.005	9.35E-07	9.36E-07	9.37E-07	9.36E-07	5±0.01	Normal
0.01	1.18E-06	1.17E-06	1.15E-06	1.17E-06	10±0.01	Hyperkalemia

Monitoring hydration status is of the utmost importance to athletes , further test and analysis need to be done in order to evaluate the utility of this device for effective and non-invasive identification of dehydration, for real-time sweat $[Na^+]$ and $[K^+]$ measurements.

Outlook: Further test are being performed by incorporating ionophores as a pre-selective membrane in order to detect $[Na^+]$ and $[K^+]$ at the same time. pH analysis are being made at different pH values in order to verify that the signal is not affected by the change of the pH solution (due to transport of H^+ and OH^- ions). Preliminary results show that the influence of pH is negligible.

8 CONCLUSIONS

Conclusions

This thesis describes the preparation, characterization and possible applications of membranes based on graphene oxide (GO) for selective ion transport.

The key scientific idea is to use the nanometric spaces existing between stacked GO nanosheets as ion sieves for water solutions. The thesis tries to exploit it in different ways, going from chemistry to biomedical, sensing and wearable applications.

Along the chapters; It is described the used experimental techniques, the electrochemical characterization and the description of the fabrication methods, the experimental set-up developed to perform the ion transport measurements focussing on the preliminary tests and the reference measurements, and the azobenzene systems and their use in GO membranes.

After the optimization of the method and the design of a prototype; we develop a wereable, cheap, non ivansive sensor, which is selective for electrolytes in sweat, it does not need an external pump to push the sample, is working just with a common watch battery and it exclude all the complex matrix of the sample. The current prototype (patent submitted) is able to detect potassium, and chloride which are related to some important diseases as hypokalemia or cystic fibrosis in child, within a timescale of a few minutes. Our prototype is sensitive enough for these applications, moreover, allows a non-invasive measurement method which had never been used as a conductometric measurement before, avoiding all the problems of pretreatment of the sample due to the complex matrix of biological systems.

Highlights:

- Low driving voltages ($\pm 0.5V$).
- Capability of delivering small quantities of sample solution (μL -mL) without external instruments (peristaltic pumps, syringes).
- Biofriendly.
- Cheap: paper based membrane, graphene oxide and graphite ink electrodes.
- Wearable-Flexible (polymer based, non toxic).
- No need of pretreatment of biological matrix sample.
- Selective-Sensitive 1.5 ± 0.01 mM [K⁺] or [Cl⁻].
- Non invasive.

ACRONYMS

ΔSP	Surface Potential Maps
AFM	Atomic Force Microscopy
AZO	Azobenzene
CF	Cystic Fibrosis
CNT	Carbon Nanotubes
DC	Direct Current
DI	Deionized
DO3	Disperse Orange 3
EDL	Electrical Double Layer
EDS	Energy-Dispersive X-ray Spectroscopy
GO	Graphene Oxide
GOM	Graphene Oxide Membranes
GRM	Graphene Related Materials
HLPC-MS	Liquid Chromatography–Mass Spectrometry
KPFM	Kelvin Probe Force Microscopy
NMR	Nuclear Magnetic Resonance
PAH	Small Organic Molecules
POC	Point of Care
SAMs	Self-Assembled Monolayers
SEM	Scanning Electron Microscope
SPM	Scanning Probe Microscopy
SWCNTs	Single-Walled Carbon Nanotubes
XPS	X-ray Photoelectron Spectroscopy
XRD	X-Ray Diffraction

REFERENCES

1. Gao, J., Feng, Y., Guo, W. & Jiang, L. Nanofluidics in two-dimensional layered materials: Inspirations from nature. *Chem. Soc. Rev.* **46**, 5400–5424 (2017).
2. Schoch, R. B., Han, J. & Renaud, P. Transport phenomena in nanofluidics. *Rev. Mod. Phys.* (2008). doi:10.1103/RevModPhys.80.839
3. Sparreboom, W., Van Den Berg, A. & Eijkel, J. C. T. Principles and applications of nanofluidic transport. *Nature Nanotechnology* (2009). doi:10.1038/nnano.2009.332
4. Stein, D., Kruithof, M. & Dekker, C. Surface-charge-governed ion transport in nanofluidic channels. *Phys. Rev. Lett.* (2004). doi:10.1103/PhysRevLett.93.035901
5. Blom, M. T., Chmela, E., Oosterbroek, R. E., Tijssen, R. & Van Den Berg, A. On-Chip Hydrodynamic Chromatography Separation and Detection of Nanoparticles and Biomolecules. *Anal. Chem.* (2003). doi:10.1021/ac034663l
6. Guo, W., Tian, Y. & Jiang, L. Asymmetric ion transport through ion-channel-mimetic solid-state nanopores. *Acc. Chem. Res.* **46**, 2834–2846 (2013).
7. Siwy, Z. S. Ion-current rectification in nanopores and nanotubes with broken symmetry. *Adv. Funct. Mater.* (2006). doi:10.1002/adfm.200500471
8. Glaser, D. E. & Viney, C. Biomimetic Materials. in *Biomaterials Science: An Introduction to Materials: Third Edition* (2013). doi:10.1016/B978-0-08-087780-8.00033-4
9. Berndt, A., Lee, S. Y., Ramakrishnan, C. & Deisseroth, K. Structure-guided transformation of channelrhodopsin into a light-activated chloride channel. *Science* . (2014). doi:10.1126/science.1252367
10. Wang, G., Bohaty, A. K., Zharov, I. & White, H. S. Photon gated transport at the glass nanopore electrode. *J. Am. Chem. Soc.* (2006). doi:10.1021/ja064274j
11. Wietek, J. *et al.* Conversion of channelrhodopsin into a light-gated chloride channel. *Science* (2014). doi:10.1126/science.1249375
12. Whang Dong, R. & Apaydin Dogukan, H. Artificial Photosynthesis: Learning from Nature. *ChemPhotoChem* (2018). doi:10.1002/cptc.201700163
13. Sauvage, J.-P. *Molecular Machines and Motors*. Springer **99**, (2010).
14. Bandara, H. M. D. & Burdette, S. C. Photoisomerization in different classes of azobenzene. *Chem. Soc. Rev.* **41**, 1809–25 (2012).
15. Coskun, A., Banaszak, M., Astumian, R. D., Stoddart, J. F. & Grzybowski, B. A. Great expectations: Can artificial molecular machines deliver on their promise? *Chem. Soc. Rev.* **41**, 19–30 (2012).
16. Chen, J. *et al.* Artificial muscle-like function from hierarchical supramolecular assembly of photoresponsive molecular motors. *Nat. Chem.* **10**, 132–138 (2018).

17. Balzani, V., Gomez-lopez, M. & Stoddart, J. F. Molecular machines. *Acc. Chem. Res.* **31**, 405–414 (1997).
18. Wearable Electronic Devices Market—Global Industry Analysis, Size, Share, Trends and Forecast,. 2015-2024 (2017).
19. Guk, K. *et al.* Evolution of wearable devices with real-time disease monitoring for personalized healthcare. *Nanomaterials* **9**, 1–23 (2019).
20. Hwang, I. *et al.* Multifunctional Smart Skin Adhesive Patches for Advanced Health Care. *Adv. Healthc. Mater.* **7**, 1–20 (2018).
21. Gong, S. *et al.* Highly Stretchy Black Gold E-Skin Nanopatches as Highly Sensitive Wearable Biomedical Sensors. *Adv. Electron. Mater.* (2015). doi:10.1002/aelm.201400063
22. Kim, D. H. *et al.* Dissolvable films of silk fibroin for ultrathin conformal bio-integrated electronics. *Nat. Mater.* (2010). doi:10.1038/nmat2745
23. Yao, S., Swetha, P. & Zhu, Y. Nanomaterial-Enabled Wearable Sensors for Healthcare. *Adv. Healthc. Mater.* **7**, 1–27 (2018).
24. Campana, A., Cramer, T., Simon, D. T., Berggren, M. & Biscarini, F. Electrocardiographic Recording with Conformable Organic Electrochemical Transistor Fabricated on Resorbable Bioscaffold. *Adv. Mater.* **26**, 3874–3878 (2014).
25. Heras, A. *et al.* A flexible platform of electrochemically functionalized carbon nanotubes for NADH sensors. *Sensors (Switzerland)* **19**, 1–12 (2019).
26. Novoselov, K. S. *et al.* Electric field in atomically thin carbon films. *Science* . (2004). doi:10.1126/science.1102896
27. Avouris, P. & Dimitrakopoulos, C. Graphene: Synthesis and applications. *Materials Today* (2012). doi:10.1016/S1369-7021(12)70044-5
28. Geim, A. K. & Novoselov, K. S. The rise of graphene. in *Nanoscience and Technology: A Collection of Reviews from Nature Journals* (2009). doi:10.1142/9789814287005_0002
29. Shetti, N. P., Nayak, D. S., Reddy, K. R. & Aminabhvi, T. M. *Graphene–Clay-Based Hybrid Nanostructures for Electrochemical Sensors and Biosensors. Graphene-Based Electrochemical Sensors for Biomolecules* (Elsevier Inc., 2019). doi:10.1016/b978-0-12-815394-9.00010-8
30. Zhu, Y. *et al.* Graphene and graphene oxide: Synthesis, properties, and applications. *Adv. Mater.* (2010). doi:10.1002/adma.201001068
31. Revin, S. B. & John, S. A. Electrochemical sensor for neurotransmitters at physiological pH using a heterocyclic conducting polymer modified electrode. *Analyst* (2012). doi:10.1039/c1an15746a
32. Erickson, K. *et al.* Determination of the local chemical structure of graphene oxide and reduced graphene oxide. *Adv. Mater.* (2010). doi:10.1002/adma.201000732
33. Ghaffar, A., Zhang, L., Zhu, X. & Chen, B. Porous PVdF/GO Nanofibrous Membranes for Selective Separation and Recycling of Charged Organic Dyes from Water. *Environ. Sci.*

- Technol.* (2018). doi:10.1021/acs.est.7b06081
34. Han, J. L. *et al.* Shielding membrane surface carboxyl groups by covalent-binding graphene oxide to improve anti-fouling property and the simultaneous promotion of flux. *Water Res.* (2016). doi:10.1016/j.watres.2016.06.032
 35. Yeh, C.-N., Raidongia, K., Shao, J., Yang, Q.-H. & Huang, J. On the origin of the stability of graphene oxide membranes in water. *Nat. Chem.* **7**, 166–70 (2014).
 36. Rao, C. N. R., Sood, A. K., Voggu, R. & Subrahmanyam, K. S. Some novel attributes of graphene. *J. Phys. Chem. Lett.* (2010). doi:10.1021/jz9004174
 37. Joshi, R. K., Alwarappan, S., Yoshimura, M., Sahajwalla, V. & Nishina, Y. Graphene oxide: The new membrane material. *Appl. Mater. Today* **1**, 1–12 (2015).
 38. Abdul, G., Zhu, X. & Chen, B. Structural characteristics of biochar-graphene nanosheet composites and their adsorption performance for phthalic acid esters. *Chem. Eng. J.* (2017). doi:10.1016/j.cej.2017.02.074
 39. Joshi, R. K. *et al.* Precise and ultrafast molecular sieving through graphene oxide membranes. *Science* **343**, 752–4 (2014).
 40. Yang, Q. *et al.* Ultrathin graphene-based membrane with precise molecular sieving and ultrafast solvent permeation. *Nat. Mater.* (2017). doi:10.1038/nmat5025
 41. Celebi, K. *et al.* Ultimate permeation across atomically thin porous graphene. *Science.* (2014). doi:10.1126/science.1249097
 42. Cohen-Tanugi, D. & Grossman, J. C. Water desalination across nanoporous graphene. *Nano Lett.* (2012). doi:10.1021/nl3012853
 43. Huang, L. *et al.* Reduced Graphene Oxide Membranes for Ultrafast Organic Solvent Nanofiltration. *Adv. Mater.* **28**, 8669–8674 (2016).
 44. Nair, R. R., Wu, H. A., Jayaram, P. N., Grigorieva, I. V. & Geim, A. K. Unimpeded Permeation of Water Through Helium-Leak-Tight Graphene-Based Membranes. *Science* (80-.). **335**, 442–444 (2012).
 45. Huang, L., Zhang, M., Li, C. & Shi, G. Graphene-based membranes for molecular separation. *J. Phys. Chem. Lett.* **6**, 2806–2815 (2015).
 46. Koltonow, B. A. R. & Huang, J. Two-dimensional nanofluidics. *Science.* **351**, 1395–1397 (2016).
 47. Romanelli, G. *et al.* Soft confinement of water in graphene-oxide membranes. *Carbon N. Y.* **108**, 199–203 (2016).
 48. Cheng, L. J. & Guo, L. J. Ionic current rectification, breakdown, and switching in heterogeneous oxide nanofluidic devices. *ACS Nano* (2009). doi:10.1021/nn8007542
 49. Karnik, R., Duan, C., Castelino, K., Daiguji, H. & Majumdar, A. Rectification of ionic current in a nanofluidic diode. *Nano Lett.* (2007). doi:10.1021/nl062806o

50. Yameen, B. *et al.* Single conical nanopores displaying pH-tunable rectifying characteristics. manipulating ionic transport with zwitterionic polymer brushes. *J. Am. Chem. Soc.* (2009). doi:10.1021/ja8086104
51. Zhou, Y. *et al.* High-temperature gating of solid-state nanopores with thermo-responsive macromolecular nanoactuators in ionic liquids. *Adv. Mater.* (2012). doi:10.1002/adma.201104814
52. Raidongia, K. & Huang, J. Nanofluidic Ion Transport through Reconstructed Layered Materials. *J. Am. Chem. Soc.* **134**, 16528–16531 (2012).
53. Abraham, J. *et al.* Tunable sieving of ions using graphene oxide membranes. *Nat. Nanotechnol.* **12**, 546–550 (2017).
54. Kim, S. *et al.* Biomimetic selective ion transport through graphene oxide membranes functionalized with ion recognizing peptides. *Chem. Mater.* **27**, 1255–1261 (2015).
55. Binnig, G., Rohrer, H., Gerber, C. & Weibel, E. Surface studies by scanning tunneling microscopy. *Phys. Rev. Lett.* (1982). doi:10.1103/PhysRevLett.49.57
56. Binnig, G. & Quate, C. F. Atomic Force Microscope. *Phys. Rev. Lett.* **56**, 930–934 (1986).
57. García, R. & Pérez, R. Dynamic atomic force microscopy methods. *Surface Science Reports* (2002). doi:10.1016/s0167-5729(02)00077-8
58. NT-MDT Spectrum Instruments. Available <https://www.ntmdt-si.com/>. (Accessed 5th December 2018)
59. Gwyddion – Free SPM (AFM, SNOM/NSOM, STM, MFM, ...) data analysis software. Available <http://gwyddion.net/>. (Accessed 5th December 2018)
60. Nonnenmacher, M., O'Boyle, M. P. & Wickramasinghe, H. K. Kelvin probe force microscopy. *Appl. Phys. Lett.* **58**, 2921–2923 (1991).
61. Liscio, A., Palermo, V. & Samorì, P. Probing local surface potential of quasi-one-dimensional systems: A KPFM study of P3HT nanofibers. *Adv. Funct. Mater.* (2008). doi:10.1002/adfm.200701142
62. Liscio, A., Palermo, V. & Samorì, P. Nanoscale Quantitative Measurement of the Potential of Charged Nanostructures by Electrostatic and Kelvin Probe Force Microscopy : Unraveling Electronic Processes in Complex. *Acc. Chem. Res.* **43**, 541–550 (2010).
63. Liscio, A. Scanning probe microscopy beyond imaging: A general tool for quantitative analysis. *ChemPhysChem* (2013). doi:10.1002/cphc.201200880
64. Hertz, H. Ueber einen Einfluss des ultravioletten Lichtes auf die elektrische Entladung. *Ann. Phys.* (1887). doi:10.1002/andp.18872670827
65. Sezen, H. & Suzer, S. XPS for chemical- and charge-sensitive analyses. *Thin Solid Films* (2013). doi:10.1016/j.tsf.2013.02.002
66. Desimoni, E. & Brunetti, B. X-ray Photoelectron Spectroscopic characterization of chemically modified electrodes used as chemical sensors and biosensors: A review.

- Chemosensors* (2015). doi:10.3390/chemosensors3020070
67. O’Keeffe, P. *et al.* Graphene-Induced Improvements of Perovskite Solar Cell Stability: Effects on Hot-Carriers. *Nano Lett.* (2019). doi:10.1021/acs.nanolett.8b03685
 68. Toschi, F. *et al.* Enhanced Charge Separation Efficiency in DNA Templated Polymer Solar Cells. *Adv. Funct. Mater.* **28**, 1–8 (2018).
 69. Becke, A. D. A new mixing of Hartree-Fock and local density-functional theories. *J. Chem. Phys.* **98**, 1372–1377 (1993).
 70. Dockic, J. *et al.* Quantum Chemical Investigation of Thermal Cis-to-Trans Isomerization of Azobenzene Derivatives: Substituent Effects, Solvent Effects, and Comparison to Experimental Data. *J. Phys. Chem. A* **113**, 6763–6773 (2009).
 71. Bléger, D. *et al.* Electronic decoupling approach to quantitative photoswitching in linear multiazobenzene architectures. *J. Phys. Chem. B* **115**, 9930–9940 (2011).
 72. Tomasi, J., Mennucci, B. & Cammi, R. Quantum Mechanical Continuum Solvation Models. *Chem. Rev.* **105**, 2999–3094 (2005).
 73. Frisch, M. J. *et al.* Gaussian09. *Gaussian 09* (2009).
 74. O’Donnell, J., Ahmadkhanlou, F., Yoon, H.-S. & Washington, G. All-printed smart structures: a viable option? in *Active and Passive Smart Structures and Integrated Systems 2014* (2014). doi:10.1117/12.2045284
 75. Rengier, F. *et al.* 3D printing based on imaging data: Review of medical applications. *International Journal of Computer Assisted Radiology and Surgery* (2010). doi:10.1007/s11548-010-0476-x
 76. Murphy, S. V. & Atala, A. 3D bioprinting of tissues and organs. *Nature Biotechnology* (2014). doi:10.1038/nbt.2958
 77. Roland ARM-10 Desktop 3D Printer - RobotShop. Available <https://www.robotshop.com/en/roland-arm-10-desktop-3d-printer.html>, (Accessed 9th Novemb. 2018)
 78. Norrman, K., Ghanbari-Siahkali, A. & Larsen, N. B. Studies of spin-coated polymer films. *Annual Reports on the Progress of Chemistry - Section C* (2005). doi:10.1039/b408857n
 79. Lawrence, C. J. The mechanics of spin coating of polymer films. *Phys. Fluids* (1988). doi:10.1063/1.866986
 80. Park, J., Lee, S. & Lee, H. H. High-mobility polymer thin-film transistors fabricated by solvent-assisted drop-casting. *Org. Electron.* (2006). doi:10.1016/j.orgel.2006.03.008
 81. Hummers, W. S. & Offeman, R. E. Preparation of Graphitic Oxide. *J. Am. Chem. Soc.* (1958). doi:10.1021/ja01539a017
 82. Kovtun, A. *et al.* Accurate chemical analysis of oxygenated graphene-based materials using X-ray photoelectron spectroscopy. *Carbon N. Y.* (2019). doi:10.1016/j.carbon.2018.11.012

83. Joshi, R. K. *et al.* Precise and Ultrafast Molecular Sieving Through Graphene Oxide Membranes. *Science* (80-.). **343**, 752–754 (2014).
84. Akbari, A. *et al.* Large-area graphene-based nanofiltration membranes by shear alignment of discotic nematic liquid crystals of graphene oxide. *Nat. Commun.* (2016). doi:10.1038/ncomms10891
85. A. E. Scheidegger. *The Physics of Flow Through Porous Media.* (1974).
86. Dullien, F. A. L. Porous media: fluid transport and pore structure. (1979). doi:10.1016/0300-9467(81)80049-4
87. Andrews, L. C. Special functions of mathematics for engineers. *SPIE Press* (1998).
88. Bird, R., Stewart, W. . & Lightfoot, E. . *Transport Phenomena.* (John Wiley & Sons, 1976).
89. Monroe, C. W. Ionic Mobility and Diffusivity. in *Encyclopedia of Applied Electrochemistry* (eds. Kreysa, G., Ota, K. & Savinell, R. F.) 1125–1130 (Springer New York, 2014). doi:10.1007/978-1-4419-6996-5_325
90. Park, S. *et al.* Graphene Oxide Papers Modified by Divalent Ions—Enhancing Mechanical Properties via Chemical Cross-Linking. *ACS Nano* **2**, 572–8 (2008).
91. Moulder, J., Stickle, W., Sobol, P. & Bomben, K. Handbook of X-ray Photoelectron Spectroscopy Perkin-Elmer Corp., Physical Electronics Division, Eden Prairie, Minnesota, USA, 1979. 190 pp. \$195. *Surf. Interface Anal.* (1981). doi:10.1002/sia.740030412
92. Briggs, D. Wanger, C. D., Riggs, W. M., Davis, L. E., Moulder, J. F., Muilenberg, G. E. Handbook of X-ray Photoelectron Spectroscopy: a reference book of standard data for use in x-ray photoelectron spectroscopy. *Perkin-Elmer Corporation* (1979).
93. García-Amorós, J. & Velasco, D. Recent advances towards azobenzene-based lightdriven real-time information-transmitting materials. *Beilstein J. Org. Chem.* **8**, 1003–1017 (2012).
94. Feringa, B. L. & Browne, W. R. *Molecular Switches, Second Edition. Molecular Switches, Second Edition* (2011). doi:10.1002/9783527634408
95. Orgiu, E. & Samorì, P. Organic electronics marries photochromism: Generation of multifunctional interfaces, materials, and devices. *Adv. Mater.* **26**, 1827–1844 (2014).
96. Shiraishi, Y., Sumiya, S. & Hirai, T. Highly sensitive cyanide anion detection with a coumarin-spiropyran conjugate as a fluorescent receptor. *Chem. Commun.* **47**, 4953–4955 (2011).
97. Champagne, B., Plaquet, A., Pozzo, J. L., Rodriguez, V. & Castet, F. Nonlinear optical molecular switches as selective cation sensors. *J. Am. Chem. Soc.* (2012). doi:10.1021/ja302395f
98. Natali, M. & Giordani, S. Molecular switches as photocontrollable ‘smart’ receptors. *Chemical Society Reviews* (2012). doi:10.1039/c2cs35015g
99. Kottas, G. S., Clarke, L. I., Horinek, D. & Michl, J. Artificial Molecular Rotors. *Chem. Rev.* **105**, 1281–1376 (2005).

100. Kinbara, K. & Aida, T. Toward Intelligent Molecular Machines: Directed Motions of Biological and Artificial Molecules and Assemblies. *Chem. Rev.* **105**, 1377–1400 (2005).
101. Iwamura, H. & Mislow, K. Stereochemical Consequences of Dynamic Gearing. *Acc. Chem. Res.* **21**, 175–182 (1988).
102. Bandara, H. M. D. & Burdette, S. C. Photoisomerization in different classes of azobenzene. *Chem. Soc. Rev.* **41**, 1809–1825 (2012).
103. Balzani, V., Credi, A. & Venturi, M. Light powered molecular machines. *Chem. Soc. Rev.* **38**, 1542–1550 (2009).
104. Yager, K. G. & Barrett, C. J. Novel photo-switching using azobenzene functional materials. *J. Photochem. Photobiol. A Chem.* **182**, 250–261 (2006).
105. Min, M., Seo, S., Lee, S. M. & Lee, H. Voltage-controlled nonvolatile molecular memory of an azobenzene monolayer through solution-processed reduced graphene oxide contacts. *Adv. Mater.* **25**, 7045–7050 (2013).
106. Tan, E. M. M. *et al.* Fast photodynamics of azobenzene probed by scanning excited-state potential energy surfaces using slow spectroscopy. *Nat. Commun.* **6**, 5860 (2015).
107. Tiberio, G., Muccioli, L., Berardi, R. & Zannoni, C. How does the trans-cis photoisomerization of azobenzene take place in organic solvents? *ChemPhysChem* (2010). doi:10.1002/cphc.200900652
108. Dürr, H. & Bouas-Laurent, H. *Photochromism: Molecules and systems. Photochromism: Molecules and Systems* (2003). doi:10.1016/B978-0-444-51322-9.X5000-3
109. Rau, H. & Lüddecke, E. On the Rotation-Inversion Controversy on Photoisomerization of Azobenzenes. Experimental Proof of Inversion. *J. Am. Chem. Soc.* **104**, 1616–1620 (1982).
110. Schultz, T. *et al.* Mechanism and dynamics of azobenzene photoisomerization. *J. Am. Chem. Soc.* (2003). doi:10.1021/ja021363x
111. Quick, M. *et al.* Photoisomerization dynamics and pathways of trans - And cis -azobenzene in solution from broadband femtosecond spectroscopies and calculations. *J. Phys. Chem. B* **118**, 8756–8771 (2014).
112. Moldt, T. *et al.* Differing Isomerization Kinetics of Azobenzene-Functionalized Self-Assembled Monolayers in Ambient Air and in Vacuum. *Langmuir* **32**, 10795–10801 (2016).
113. Rau, H. & Yu-Quan, S. Photoisomerization of sterically hindered azobenzenes. *J. Photochem. Photobiol. A Chem.* **42**, 321–327 (1988).
114. Zhang, H. *et al.* Interface engineering of semiconductor/dielectric heterojunctions toward functional organic thin-film transistors. *Nano Lett.* **11**, 4939–4946 (2011).
115. Ferri, V. *et al.* Light-Powered Electrical Switch Based on Cargo-Lifting Azobenzene. *Angew. Chem., Int. Ed.* **47**, 3407–3409 (2008).
116. Pace, G. *et al.* Cooperative light-induced molecular movements of highly ordered azobenzene self-assembled monolayers. *Proc. Natl. Acad. Sci.* **104**, 9937–9942 (2007).

117. Ishikawa, D., Ito, E., Han, M. & Hara, M. Effect of the steric molecular structure of azobenzene on the formation of self-assembled monolayers with a photoswitchable surface morphology. *Langmuir* **29**, 4622–4631 (2013).
118. Georgakilas, V. *et al.* Functionalization of graphene: Covalent and non-covalent approaches, derivatives and applications. *Chem. Rev.* **112**, 6156–6214 (2012).
119. Gmbh, C. W. V. *et al.* Microporous Metal-Organic Framework Stabilized by Balanced Multiple Host-Cousteranion Hydrogen Bonding Interactions for High-density CO₂ Capture at Ambient Conditions SI. 200–203
120. Dąbrowa, K., Niedbała, P. & Jurczak, J. Anion-tunable control of thermal Z→E isomerisation in basic azobenzene receptors SI. *Chem. Commun.* **50**, 15748–15751 (2014).
121. Niyogi, S. *et al.* Spectroscopy of covalently functionalized graphene. *Nano Lett.* (2010). doi:10.1021/nl1021128
122. Das, S., Kamat, P. V., Padmaja, S., Au, V. & Madison, S. a. Free radical induced oxidation of the azo dye Acid Yellow 9. *J. Chem. Soc. Perkin Trans. 2* **2**, 1219–1223 (1999).
123. Chang, C. W., Lu, Y. C., Wang, T. Te & Diau, E. W. G. Photoisomerization dynamics of azobenzene in solution with S₁ excitation: A femtosecond fluorescence anisotropy study. *J. Am. Chem. Soc.* **126**, 10109–10118 (2004).
124. Joshi, N. K., Fuyuki, M. & Wada, A. Polarity controlled reaction path and kinetics of thermal cis-to-trans isomerization of 4-aminoazobenzene. *J. Phys. Chem. B* **118**, 1891–1899 (2014).
125. Asano, T. & Okada, T. Thermal Z-E isomerization of azobenzenes. The pressure, solvent, and substituent effects. *J. Org. Chem.* **49**, 4387–4391 (1984).
126. Mali, C. S., Chavan, S. D., Kanse, K. S., Kumbharkhane, A. C. & Mehrotra, S. C. Dielectric relaxation of poly ethylene glycol-water mixtures using time domain technique. *Indian J. Pure Appl. Phys.* **45**, 476–481 (2007).
127. Bahrenburg, J., Röttger, K., Siewertsen, R., Renth, F. & Temps, F. Sequential photoisomerisation dynamics of the push–pull azobenzene Disperse Red 1. *Photochem. Photobiol. Sci.* **11**, 1210 (2012).
128. Palermo, V., Palma, M. & Samori, P. Electronic characterization of organic thin films by Kelvin probe force microscopy. *Adv. Mater.* **18**, 145–164 (2006).
129. Stiller, B. *et al.* Self-assembled monolayers of novel azobenzenes for optically induced switching. *Mater. Sci. Eng. C* **8–9**, 385–389 (1999).
130. Marchante, E., Crivillers, N., Buhl, M., Veciana, J. & Mas-Torrent, M. An Electrically Driven and Readable Molecular Monolayer Switch Based on a Solid Electrolyte. *Angew. Chemie Int. Ed.* 368–372 (2015). doi:10.1002/anie.201508449
131. Koshima, H., Ojima, N. & Uchimoto, H. Supporting Information for Mechanical Motion of Azobenzene Crystals upon Photoirradiation. 2–7 (2009).
132. Wang, Y. *et al.* Graphene-directed supramolecular assembly of multifunctional polymer

- hydrogel membranes. *Adv. Funct. Mater.* **25**, 126–133 (2015).
133. Wang, J. Amperometric biosensors for clinical and therapeutic drug monitoring: A review. *J. Pharm. Biomed. Anal.* (1999). doi:10.1016/S0731-7085(98)00056-9
 134. Jaffrezic-renault, N. & V.Dzyadevych, S. Conductometric Microbiosensors for Environmental Monitoring. *sensors* **8**, 2569–2588 (2008).
 135. Braiek, M., Djebbi, M. A., Chateaux, J. F. & Jaffrezic-Renault, N. A conductometric sensor for potassium detection in whole blood. *Sensors Actuators, B Chem.* **235**, 27–32 (2016).
 136. Parrilla, M., Cuartero, M. & Crespo, G. A. Wearable potentiometric ion sensors. *TrAC - Trends in Analytical Chemistry* (2019). doi:10.1016/j.trac.2018.11.024
 137. Huang, H. *et al.* Graphene-based sensors for human health monitoring. *Frontiers in Chemistry* (2019). doi:10.3389/fchem.2019.00399
 138. Pierleoni, D. *et al.* Selective Gas Permeation in Graphene Oxide-Polymer Self-Assembled Multilayers. *ACS Appl. Mater. Interfaces* **10**, 11242–11250 (2018).
 139. Kovtun, A. *et al.* Graphene oxide–polysulfone filters for tap water purification, obtained by fast microwave oven treatment. *Nanoscale* (2019). doi:10.1039/c9nr06897j
 140. Maccaferri, G. *et al.* Highly sensitive amperometric sensor for morphine detection based on electrochemically exfoliated graphene oxide. Application in screening tests of urine samples. *Sensors Actuators, B Chem.* (2019). doi:10.1016/j.snb.2018.10.163
 141. Maccaferri, G. *et al.* Systematic study of the correlation between surface chemistry, conductivity and electrocatalytic properties of graphene oxide nanosheets. *Carbon N. Y.* (2017). doi:10.1016/j.carbon.2017.05.030
 142. Bard, A. & Faulkner, L. *Electrochemical Methods: fundamentals and applications. -2nd ed. Electrochemistry. I. Faulkner, Larry R* (1944). doi:10.1016/B978-0-12-381373-2.00056-9
 143. Gao, W. *et al.* Fully integrated wearable sensor arrays for multiplexed in situ perspiration analysis. *Nature* **529**, 509–514 (2016).
 144. Sheppard, D. N. & Welsh, M. J. Structure and function of the CFTR chloride channel. *Physiological Reviews* (1999). doi:10.1152/physrev.1999.79.1.S23
 145. Kardalas, E. *et al.* Hypokalemia: A clinical update. *Endocrine Connections* (2018). doi:10.1530/EC-18-0109

LIST OF FIGURES

Figure 1. Chloride channels conducting chloride anions across a cell membrane.....	28
Figure 2. Fundamental properties and applications of 2D layered materials. The exfoliation–reconstruction strategy enables highly scalable fabrication and highly efficient chemical modification of the 2D nanofluidic systems with ultra-high ion or water flux and tunable channel size. Meanwhile, wide applications are found in, for example, biomimetic ion transport manipulation, molecular sieving, nanofluidic energy conversion, battery separators, and energy storage. ¹	29
Figure 3. Industrial wearable technologies. (A) Evolution of wearable medical devices (B) Application of wearable devices in the healthcare and biomedical monitoring systems. ¹⁹	32
Figure 4. Conceptual illustration of the medical skin adhesive patch with various fundamental and advanced functions. ²⁰	32
Figure 5. PEDOT:PSS polymer based device showing properties such as flexibility and transparency and used for Electrocardiogram (ECG) recording when attached to human skin. ²⁴	34
Figure 6. Schematic view of the UV/Vis absorption spectroelectrochemical set-up in parallel configuration. ²⁵	34
Figure 7. Unit cell of graphene evidencing the two sub-lattice structures (red and blue). ²⁷	37
Figure 8. Scheme showing that graphene is a 2D building material for carbon materials of all other dimensionalities: it can be wrapped up into 0D fullerenes, rolled into 1D nanotubes or stacked into 3D graphite. ²⁸	38
Figure 9. Graphene (A) is a two-dimensional material for constructing other nanoscale carbons such as (B) 3D graphite, (C) 1D carbon nanotubes, and (D) 0D fullerene C ₆₀ . ²⁹	39
Figure 10. A flow chart on graphene production methods with some exemplificative examples of the procedures mostly used: mechanical exfoliation, epitaxial growth, CVD, thermally reduced graphene.	40
Figure 11. Aberration corrected TEM images of the following materials. Scale bar, denoting 2 nanometers, is valid for all images. (A) Single suspended sheet of graphene. On the right, graphitic area indicated in yellow. (B) Single suspended sheet of GO. On the right, holes are indicated in blue, graphitic areas in yellow, and high contrast, disordered regions, indicating oxygen functionalities, in red. ³²	41
Figure 12. Representative structure of GO.	42
Figure 13. GO membranes obtained from Teflon filters. ³⁵	42
Figure 14. Schematic representing a membrane system. ³⁷	43

Figure 15. Schematic diagram of the two types of graphene-based membranes. (a) Nanoporous graphene membrane consists of a single layer of graphene with nanopores of defined sizes. Selectivity is achieved by size exclusion or electrostatic repulsion between charged species and the pores. (b) GOM composed of stacked GO sheets. In a GOM, the transport passages are the interlayer spaces between the sheets.⁴⁵ 44

Figure 16. Schematic model of the nanocapillaries in GO films. Monolayer water can move through the capillaries when they are wide opened, however with low humidity the capillaries becomes narrower (shown by dashed line) and as a result there is no sufficient space between the capillaries to accommodate the water molecule. Figure reproduced with permission from.⁴⁴ 45

Figure 17. Lamellar film with massive arrays of 2D nanofluidic channels can be made by the exfoliation- reconstruction approach, as illustrated with models of GO sheets terminated with negatively charged carboxyl groups.⁴⁶ 45

Figure 18. (a) AFM image of the as-prepared GOM, Z-range $\frac{1}{4}$ 3 nm; (b) As-prepared GOM before hydration; (c) XRD surveys and (d) TGA analysis of the dry (black) and hydrated (grey) membranes.⁴⁷ 46

Figure 19. (a) Schematic illustration and (b) photograph showing GO paper-based nanofluidics device. (c) Representative I–V curves recorded at different KCl concentrations. (d) Ionic conductivity as a function of salt concentration measured through GO nanochannels. Results of two devices are presented here, showing good consistency. ⁵² 47

Figure 20. Physically confined GO membranes with tunable interlayer spacing. a, Schematic illustrating the direction of ion/water permeation along graphene planes. b, Photograph of a PCGO membrane glued into a rectangular slot within a plastic disk of 5 cm in diameter. Inset: photo of the PCGO stack before it was placed inside the slot. Scale bar, 5 mm. c, Permeation rates through PCGO membranes with different interlayer distances (colour coded). The salts used were KCl, NaCl, LiCl, CaCl₂ and MgCl₂. Dashed lines are guides to the eye indicating a rapid cutoff in salt permeation, which is dependent on the interlayer spacing.⁵³ 48

Figure 21. Left: Schem and picture of the biomimetic functionalized GO membrane. Right: Permeation test of Co²⁺, Ni²⁺, and Cu²⁺ ions through GO- based membranes. 49

Figure 22. Scheme of transport through GO membranes. 50

Figure 23. Working principle of AFM; key components are cantilever with tip, laser source, photodiode and feedback loop. 55

Figure 24. Schematic representation of KPFM..... 57

Figure 25. XPS working principle (adapted from⁶⁵): XPS spectra is obtained by irradiating the sample surface with X-rays, while simultaneously measuring the kinetic energy and number of electrons that escape from the top of the surface by means of the Electron Energy Analyzer. 59

Figure 26. a) Agilent B2912A SMU; b) Agilent N1294A banana-to-triax adapters; c) sample holder and contact probes inside the Faraday cage; d) user interface of the SMU. 63

Figure 27. a) Autolab b) sample holder with an electrode for pulse method.	63
Figure 28. 3D printing process: from 3D CAD design to the printed object.	64
Figure 29. DLP printing technique. ⁷⁷	65
Figure 30. Spin coating technique.	65
Figure 31. Laurell WS 400B-6NPP/LITE spin coater.	66
Figure 32. FEG-SEM images collected by secondary electrons at (a) bare substrate (b) GO. White arrows indicate ripples typical of 2-dimensional nanosheets.	72
Figure 33. XPS spectra of GO. a) Atomic concentration of GO measured by XPS; b) survey spectrum and high-resolution C 1s spectrum of GO.	73
Figure 34. Scheme of membrane fabrication.	74
Figure 35. a) SEM images of obtained GO membranes after coverage with PDMS polymer and zoom b) Photograph showing GO nanofluidic device.	75
Figure 36. Left: SEM image of the cross-section of GOM. a) $c=0.5$ g/L; 1.5 ± 0.1 μm , b) $c=1$ g/L; 2.1 ± 0.1 μm , c) $c=2$ g/L; 5.1 ± 0.3 μm . The error was calculated with 4 membranes for each concentration of GO. Right: Tuning of the thickness, membrane thickness vs GO concentration. Red line is the calibration curve calculated by the fit.	75
Figure 37. XPS spectra: A) Si 2p and b) C 1s of GO on PDMS.	77
Figure 38. Scheme of the set-up for ion transport in plane and out of plane.	78
Figure 39. Set-up scheme: Chanel 2; A-B: biasing; VA-B: Voltage to transport ions.	79
Figure 40. a) Applied pulse in BC. b) transient displacement current (I_{displ}) versus time. C) Zoom.	80
Figure 41. Transient displacement current (I_{displ}) versus time for KCl and CaCl ₂ . Fitted with equation 4.4.b.	81
Figure 42. Transient displacement current (I_{displ}) versus time for 2 different solutions of Na ⁺ (petri dish A, conc = 0.1 M), with same concentration but different days and membranes.	82
Figure 43. Correlation of the transient displacement current (I_{displ}) and the concentration of KCl.	83
Figure 44. (a) Photograph showing GO out of plane device. (b) GO strip membrane covered with cellulose to prevent GO degradation.	84
Figure 45. Picture of the preliminar experimental set-up. Petri A: KCl 0.1M; Petri B: DI water. Volume: 10mL.	85

Figure 46. Design of the device built with B9Creator [®] V1.2HD. *Dimensions divided by 1000.	86
Figure 47. Scheme of the final set-up created by 3D printing.	86
Figure 48. Illustration of the transport mechanisms in the nanochannels in GOMs under the (a) pressure-driven permeation of water, as typically used in ion sieving set-up and (b) Ion flow due to the potential bias applied, as we performed in this thesis.	87
Figure 49. Diffusivity vs hydrated diameter.....	89
Figure 50. Ion concentration vs bias time: a) in plane and b) out of plane (dashed lines show the linear behaviour for eye guide) Red: cellulose; Orange: 200nm GOM; Brown: 1500nm GOM. 0.1m 1M KCl and H ₂ O included as a reference. Error bars denote standard deviation.....	90
Figure 51. Concentration (calculated by Transient displacement current) versus time for K ⁺ , with different concentrations (Thickness) of GO. (c = 0.5 g/L, 1.5±0.1µm) and (c = 0.33g/L, 0.2±0.05µm). Double layer cellulose membrane included as a control. H ₂ O and 100mM KCl signals included as a reference.	91
Figure 52. Concentration (calculated by Transient displacement current) versus time for K ⁺ , with different concentrations (Thickness) of GO a) c=0.5g/L; 1.5±0.1µ, b) c=1g/L; 2.1±0.1µ, c) c=2g/L; 5.1±0.3µ. H ₂ O and 100mM KCl signals included as a reference.	92
Figure 53. Hydrated diameter of the ions under study.....	92
Figure 54. Graph: Concentration versus time for 2 different solutions of Na ⁺ K ⁺ , Na ⁺ , Li ⁺ , Ca ⁺⁺ , Mg ⁺⁺ . (Cell A, conc = 0.1 M), with same concentration but different days and membranes.....	93
Figure 55. Graph: Concentration versus time for 2 different solutions of F ⁻ , Cl ⁻ , Br ⁻ (Cell A, conc = 0.1 M), with same concentration but different days and membranes.....	93
Figure 56. Plateau Concentration vs hydrated diameter.....	94
Figure 57. Models of the M-modified GO papers: (a) schematic model of the reaction between GO paper. ⁹⁰	94
Figure 58. Concentration Plateau (mM) vs recalculated* Effective Density, which is new parameter calculated taking into account the hydrated ion volume.	95
Figure 59. Graph a: I plateau versus hydrated Radio. Graph b: I plateau versus 1/charge density. Graph c: α versus charge density.....	96
Figure 60. Ion concentration vs time of biasing in cell A feed (black), and cell B (red) in: a) Out of plane b) In plane	97
Figure 61. XPS signal of GO membrane after bias (upper black circle) and reference signal from GO membrane on PDMS before bias (lower blue squares) in a) Li ⁺ , b) Na ⁺ , c) Mg ²⁺ , d) K ⁺ and e) Ca ²⁺ solutions.	99

Figure 62. XRD spectra showing the change in the d-spacing of GO membranes in different salt solutions: (A) cation (fixed anion = Cl ⁻), (B) anion (fixed cation = K ⁺).....	100
Figure 63. Environmental SEM image of GOM before and after biasing of K ⁺ . Small crystals oriented along the ion current direction.....	101
Figure 64. Concentration of K ⁺ ions versus time for in plane (red) and out of plane (orange) method .Same thickness of GO, c = 0.5 g/L, 1.5±0.1µm. H ₂ O and 100mM KCl signals included as a reference.....	103
Figure 65. Isomerization of an azobenzene molecule.....	107
Figure 66. Photochromism of azobenzene derivatives and energetic profile for the switching process. ⁹³	107
Figure 67. Rotation and inversion mechanisms proposed for the thermal cis-to-trans isomerisation processes of azobenzenes.	108
Figure 68. Schematic of different approaches to functionalize graphene by using covalent or non-covalent (supramolecular) approaches.	110
Figure 69. Triazole structure.....	111
Figure 70. Scheme of the reduction of DO3.	112
Figure 71. NMR spectra of compound reduced DO3 in DMSO-d ₆ (400MHz). Experimental: ¹ H NMR (400 MHz, DMSO) δ 7.55 (d, J = 8.8 Hz, 4H), 6.65 (d, J = 8.8 Hz, 4H), 5.73 (s, 4H). ...	113
Figure 72. TLC of reduced DO3. R _f ,3 = 0.55, R _f ,2 (Disperse Orange 3) = 0.74 (hexanes - ethyl acetate 1:1 v/v).....	113
Figure 73. Scheme of Synthesis of DMAZ and 4-(4H-1,2,4-Triazol-4-yl)benzoic Acid (Hept). 114	114
Figure 74. NMR spectra of DMAZ in DMSO-d ₆ (400MHz). Experimental: ¹ H NMR (400 MHz, DMSO) δ 3,24 (s, 6H), 8,34 (s,1H).	114
Figure 75. Scheme of the synthesis of the compound VQ10 from DO3 and DMAZ.....	115
Figure 76. TLC of reduced VQ10. R _f , 3 = 0.55, R _f , 2 (Disperse Orange 3) = 0.74 (hexanes - ethyl acetate 1:1 v/v).....	115
Figure 77. HPLS-MS spectra of the compound VQ10.....	116
Figure 78. Scheme of the reduction of VQ10.....	116
Figure 79. Changes in the absorption spectra of the triazole azobenzene in DMF upon irradiation at 365 nm.....	117
Figure 80. Example of covalent functionalization of graphene by azobenzene with molecular hydrogen bonds.	118

Figure 81. Scheme of functionalization of GO sheets with commercial azobenzenes (AZO1)..	118
Figure 82. a) Structure and different conformations AZO1, one of the azobenzene molecules studied in this work. b) Schematic representation of all the different solid and liquid environments where the cis \rightarrow trans switching of the molecule was studied.	119
Figure 83. . a,b,c) Optical absorption spectra of AZO1 in different solvents. d) Calculated spectrum for AZO1 in its trans- (blue) and cis- (green) forms in water before and after UV illumination.	123
Figure 84. a) Changes in the absorption spectra of AZO1 in DMF upon irradiation at 365 nm. The Arrow indicates the changes upon irradiation time). The different spectra have been recorded each 30 seconds. b) Absorbance at 410 nm (black squares) as a function of irradiation time. The red solid line shows a fit of the experimental data acquired during 5 cycles of irradiation under the same conditions.	124
Figure 85. Changes in optical absorption of AZO1 as a function of time a) DMF and b) different mixtures of water and PEG, ranging from pure water till pure PEG.	127
Figure 86. Transient spectrum of AZO1 50 μ M in DMF with a pump pulse at 410 nm (280 μ J/cm ²). The time delay between the pump and the probe is 0.65 ps. The shaded area in the spectrum shows an intense negative feature due to scattered pump radiation around 410 nm..	128
Figure 87. Transient spectrum of AZO1 100 μ M in H ₂ O with a pump pulse at 385 nm (280 μ J/cm ²). The time delay between the pump and the probe is 0.5 ps. The shaded area in the spectrum shows an intense negative feature due to scattered pump radiation around 385 nm..	129
Figure 88. AFM topography and corresponding Surface potential maps (Δ SP) measured on AZO1 and AZO2 islands deposited on ultraflat silicon substrate. Δ SP maps are obtained by comparing the KPFM images acquired after and before irradiation at 365 nm for 60 min: Δ SP = KPFM _{trans} – KPFM _{cis} . Z-ranges. AFM images = 8 nm, Δ SP images = 30 mV.	130
Figure 89. a) phase-AFM topography image of mesoscopic AZO1 crystals self-assembled on silicon. b) Reflectance spectra of mesoscopic AZO1 layer during exposure to UV Black line (initial one). Blue line after 30 min exposure to UV λ =365nm (Pd=3.2 mW/cm ²). Red line after 30 min exposure to Vis λ =440nm (Pd=0.56 mW/cm ²).	133
Figure 90. Schematic representation of the two azobenzene based compounds under study.	134
Figure 91. Calculated UV-VIS spectra of compound AZO1 in trans (black) and cis (red line) isomers in PEG, DMF and H ₂ O solvents (from top to bottom). The vertical lines and numbers depicted in the graph represent the magnitude and wavelength of the main optical transitions respectively.	136
Figure 92. Calculated UV-VIS spectra of compound AZO2 in trans (black) and cis (red line) isomers in DMF solvent. The vertical lines and numbers depicted in the graph represent the magnitude and wavelength of the main optical transitions respectively.	137
Figure 93. Scheme of the covalent functionalization of GO with azobenzene molecules.	138

Figure 94. <i>Picture of residual azobenzene after functionalization.</i>	138
Figure 95. <i>UV-vis absorption spectra of GO (blue), azobenzene (green), GO-AZO covalent (red), GO-AZO physisorbed (black).</i>	139
Figure 96. <i>XPS spectra of GO, azobenzene, and GO after covalent functionalization.</i>	139
Figure 97. <i>Scheme of GO-AZO membrane.</i>	142
Figure 98. <i>Picture of the GO-PAH membrane obtained.</i>	143
Figure 99. <i>Dimensions of the isomerization of AZO1.</i>	143
Figure 100. <i>Spectroscopy characterization of GO, AZO1-GO, and AZO2-GO. UV/vis absorption spectra recorded in water after 30min of irradiation.</i>	144
Figure 101. <i>XRD spectra of GO-AZO1 before and after UV irradiation.</i>	144
Figure 102. <i>The main stages in the sensor operation.</i> ²⁹	149
Figure 103. <i>Ion migration in the solution volume and electrolyte conductivity.</i> ¹³⁴	151
Figure 104. <i>Scheme showing the 2-dimensional sieving effect of the GRM membrane, for detection of specific ions.</i>	154
Figure 105. <i>Examples of the two main applications of wearable sensors: health-care monitoring and sport performance.</i> ¹³⁶	154
Figure 106. <i>Picture of the AUTOLAB set-up.</i>	155
Figure 107. <i>Scheme of an electrode for biosensing.</i>	156
Figure 108. <i>Scheme of the 3 electrodes prototype biosensor.</i>	157
Figure 109. <i>Picture of the 3 electrode prototype connected to the AUTOLAB.</i>	158
Figure 110. <i>Scheme of the 2 electrodes prototype biosensor.</i>	159
Figure 111. <i>Picture of the 2 electrode (DRP-PW-IDEAU 100) prototype connected to the AUTOLAB.</i>	159
Figure 112. <i>Comparison of porous filter paper. Materials: ® Nitrocellulose Membranes CN140 Unbacked (blue). Cellulose based membrane (red) and Nitrocellulose BCN140 membrane (orange),</i>	160
Figure 113. <i>Scheme of the conductive ink.</i>	161
Figure 114. <i>Calibration curve. Left: Electrode DRP- 100. Right: Electrode DRP-PW-IDEAU 100.</i>	162
Figure 115. <i>Scheme of the prototype bracelet for biosensing.</i>	163

Figure 116. *Left and center: photos of the prototype assembled, in this case for use as a bracelet. Final applications will likely be placed instead on the back or upper arm.* 163

Figure 117. *Graph showing 3 test, one negative (12Mm Cl⁻), one non clonclusive (48mM Cl⁻) and one Positive for cystic fibrosis (100mM Cl⁻), using artificial sweat and a known concentration of Cl⁻.* 165

LIST OF TABLES

Table 1. Parameters of the ions under study and the salt used in the experiments. *Calculated Effective Density ($C/\text{\AA}^3$)= number of charge / hydrated volume.....	78
Table 2. Calculated data for K^+ , Na^+ , and Ca^{2+}	95
Table 3. Identification of cations present on GO membrane in PDMS after bias: characteristic transitions observed and reference values. KE=Kinetic Energy, BE=Binding Energy. *Presence of Ca contamination (0.3% at.).....	99
Table 4. Identification of anions present on GO membrane in PDMS after bias: characteristic transitions observed and reference values. KE=Kinetic Energy, BE=Binding Energy. * Presence of K contamination (3.7 % at.).....	100
Table 5. Chemical state of the ions inside the GOM after biasing confirmed by XPS and ESD spectroscopy.....	102
Table 6. Kinetic constants calculated for AZO1 switching in different solvents.	125
Table 7. Ground state properties for the different systems under study: relative energy (ΔE_{rel}) respect the less stable compound (cis- isomers in PEG and DMF for AZO1 and AZO2 respectively), difference in energy ($\Delta E_{cis-trans}$) between isomers, Lowest/Highest Un-/Occupied molecular orbital (LUMO/HOMO) level energies, electronic bandgap and dipole magnitude. .	135
Table 8. Excited state properties in the UV-VIS region for the two azobenzene compounds under study: wavelengths (λ), oscillator strengths (f), major contributions and related percentage (%) of the main optical transitions.....	137
Table 9. Ion mobility in infinitely diluted aqueous solutions at temperature of 25 °C. ¹³⁴	152
Table 10. Calibration of DRP- 100 and DRP-PW-IDEAU 100.....	162
Table 11. Calculated parameters for Cl^- ions.....	164
Table 12. Calculated parameters for K^+ ions. <0,0025 [K^+]M hypokalemia; 0.0025-0.005 [K^+]M normal; >0.0055 [K^+]M hyperkalemia.....	166

LIST OF ACTIVITIES DURING PHD

Publications, conferences, workshop attendance, courses, and seminar presentations:

V.Quintano (**Patent submitted**) Electrochemical sensor with 2-dimensional nanofiltering pores for selective ion detection. November 2019

Z.Xia, V.Quintano, *et al.* A robust, modular approach to produce graphene–MOx multilayer foams as electrodes for Li-ion batteries. *Nanoscale* (2019). doi:10.1039/c8nr09195a

V.Quintano. *et al.* Measurement of cis-trans conformational switching of polar azobenzenes on polar and apolar solvents and self-assembled monolayers (submitted)

J.Sun, V.Quintano, *et al.* Reversible Na⁺ intercalation into asymmetric “Janus” graphene, studied in real time for sodium ion battery applications (submitted)

V.Quintano. *et al.* Ion transport through graphene based materials for biomedical applications (Manuscript in preparation)

Graphene Week 2019 (European comission) 23th-27th September. Oral contribution: “Selective ion transport and crystal growth in 2-dimensions inside graphene oxide membranes” V.Quintano. Helsinki, Finland.

Conference on Chemistry of Two-Dimensional Materials (**Chem2DMat**) 10th-13th sept 2019. Dresden,Germany.

Poster: Photoswitching of commercial azobenzenes in different environments. V. Quintano, F. Liscio, A. Liscio, V. Palermo.

Graphene2019 International Conference "Selective ion transport and crystal growth in 2-dimensions inside graphene oxide membranes" V.Quintano, A.Kovtun, A.Liscio, V.Palermo (Rome-Italy, June 25-28, 2019).

PhD Day in Molecular and Regenerative Medicine, 24 January 2019. Department of Physics, Informatics and Mathematics. UNIMORE, Modena.

Ion transport through graphene oxide membranes for biomedical applications. V. Quintano, A.Kovtun, A. Liscio, Parkula.V, V. Palermo , M. Di Lauro and F. Biscarini.

Summer School Graphene Flagship Conference: 2D materials for environment

and energy applications. 1th -6th July 2018. Hindas, Sweden.

Poster 1: *Molecular Transport and Dynamics in 2-Dimensional Materials*. V. Quintano, M. Christian, A. Liscio, V. Palermo, M. Di Lauro and F. Biscarini.

Poster 2: *Multilayer Sandwich Structures of Fe₂O₃-Graphene Foams and Their Application in Energy Storage*. Z.Xia, V.Quintano, M. Christian, M.Gazzano, A.Kovtun, C.Arbizzani, V.Palermo, and V.Morandi . **(Second prize)**.

Winter School Graphene Flagship Conference: Structural Characterization on graphene-based materials. 5th -10th February 2018. Obergurgl, Austria.

Poster 1: Ion transport through graphene oxide membranes. V. Quintano, F.Liscio, A. Kovtun, V. Palermo, M.Di Lauro and F.Biscarini.

Poster 2: Energy store in 3D graphene composites. M. Christian, Z.Xia, M.Gazzano, V.Quintano, A.Kovtun, C.Arbizzani, V.Palermo, and V.Morandi **(First prize)**.

PhD Day in Molecular and Regenerative Medicine, 18 January 2018. Department of Physics, Informatics and Mathematics. UNIMORE, Modena.

Photoswitching of azobenzenes in constrained environment for biomedical applications. V.Quintano, S.Dell'Elce, F.Liscio, A.Liscio, V.Palermo, M.Di Lauro and F.Biscarini.

iSwitch 3rd Workshop: Business and Management Skills- Organized by CSIC, Barcelona, Spain 15th, 16th March 2018.

1st European Conference on Chemistry of Two-Dimensional Materials (**Chem2DMat**) 22th-26th august 2017. Faculty of Chemistry, Strasbourg, France.

Poster: *Photoswitching of azobenzenes in constrained 2D d environment*. V. Quintano, S. Dell'Elce, F. Liscio, A. Liscio, V. Palermo.

3rd Bologna SPM Workshop. Scanning Probe Microscopy and Spectroscopy for mineral, biological and material science. 14th July 2017. Dept. Biological, Geological and Environmental sciences. University Bologna, Italy.

Formazione generale dei lavoratori ai sensi dell'art. 37 del Dlgs 81/08 così come definito dall'Accordo Stato Regioni del 21/12/11. - Organized CNR, Bologna 2017.

iSwitch 2nd Workshop: Presentation Skills- Organized by ISIS, Strasbourg, France 7th, 8th November 2017

Workshop: International Workshop on Light Activated Nanostructures- Organized by CNR, Bologna, Italy 16th May 2017

iSwitch 1st Workshop: Entrepreneurship and Career Planning- Organized by CNR, Bologna, Italy 24th, 25th January 2017

iSwitch 2nd School: **Molecular Design and Synthesis. Honored Invited Professor Jean-Pierre Sauvage:** From transition metal-based interlocking rings to molecular switches and machines.– Organized by University of Basel, Freiburg (Germany) / 13th–15th September 2016.

iSwitch 1st School: Advanced Optical Materials and Devices - University College of London (UK) /1st -3rd of March 2016

Secondments:

23st August to 2nd September: XRD measurements within the Flagship project - **Chalmers University** (Goteborg, Sweden)

1st May to 14th August 2018: Design and experiment of microfluidic devices fabricated with 3D printing - **SCRIBA Nanotecnologie** S.R.L (Bologna, Italy)

29th January to 15th February 2017/ 16th September to 1st October 2016: Synthesis and functionalization of graphene based materials - Institut de Science et d'Ingénierie Supramoléculaires (ISIS). **Université de Strasbourg** (Strasbourg, France)

15th-31th January 2018: Resolving photoisomerization dynamics via ultrafast UV-visible transient absorption spectroscopy-EuroFEL Support Laboratory, a fast-spectroscopy facility. **ISM-CNR**. (Rome, Italy)

ACKNOWLEDGEMENTS

I would like to thank to my PhD advisors, Professors Vincenzo Palermo and Fabio Biscarini, for supporting me during these past four years. Vincenzo is one of the smartest people I know. I hope that I could be as lively, enthusiastic, and energetic as him and to someday be able to command an audience as well as he does. They have been supportive and have given me the freedom to pursue various projects without objection. They have also provided insightful discussions about the research. I am also very grateful to Dr. Andrea Liscio for his scientific advice and knowledge and many insightful discussions and suggestions. He is my primary resource for getting my science questions answered and was instrumental in helping me crank out this thesis, all in few month. All my gratitude to all professors involved in my MarieCurie project, especially to Professor Paolo Samorí.

I also thank UNIMORE Labs, in particular all the people from LEO and ELSENSE Labs, with special mention to Professor Chiara Zanardi. I am also pleased to say thank you all Nanochemistry Lab (ISOF-CNR). I would always remember my fellow labmates too for the fun-time we spent together .It wouldn't have been possible to conduct this research without their precious support. They all really mean a lot to me. A special wink to my iSwitch and Graphene Flagship colleagues, with whom I toured Europe learning how to give talks; Thanks to Marie Sklodowska-Curie project "ISwitch" (G.A. 642196) and GrapheneCore2 (G.A. 785219) – Graphene Flagship.

I would also like to thank my friends from Bologna, and my housemates. Love you so much girls. Thank you for making me feel at home being so far from my country.

I especially thank my parents, they gave me enough moral support, encouragement and motivation to accomplish my personal goals. I thank my whole family and lifelong friends, this dissertation would not have been possible without their warm love, continued patience, and endless support.

I owe thanks to a very special person, my husband, for his continued and unfailing love, support and understanding during my pursuit of my PhD. You were always around at times I thought that it is impossible to continue, you helped me to keep things in perspective. I greatly value his contribution and deeply appreciate his belief in me. An above all, for what is yet to come.